

# **Dissertation**

submitted to the  
Combined Faculties of the Natural Sciences and Mathematics  
of the Ruperto-Carola-University of Heidelberg, Germany,  
for the degree of  
Doctor of Natural Sciences

Put forward by

**Georg Eckhard Winner**  
born in: Berlin, Germany

Oral examination: October 19, 2020



# **On the Evolution and Observational Signatures of Cosmic Ray Electrons in Magnetohydrodynamical Simulations**

Georg Eckhard Winner

Referees: Prof. Dr. Christoph Pfrommer  
Prof. Dr. Ralf Klessen



## **On the Evolution and Observational Signatures of Cosmic Ray Electrons in Magnetohydrodynamical Simulations**

Cosmic ray (CR) electrons are ubiquitous in the universe and reveal key insights into the non-thermal physics. Their synchrotron radiation, bremsstrahlung, and inverse Compton emission shed light on the interstellar medium, on galaxies and galactic outflows, on galaxy clusters, and on active galactic nuclei. Models of these emission processes can be tested against observations with magnetohydrodynamical (MHD) simulations. While dynamically important CR protons are often included in MHD simulations, CR electrons are rarely treated because their treatment requires a detailed numerical modeling of their spectra due to complex hysteresis effects. Within the scope of this work, I have developed the efficient post-processing code `CREST` that evolves spatially and temporally resolved CR electron spectra. This code allows a comparison of CR electron emission signatures to observations by means of multi-frequency spectra and morphology. Further, `CREST` enables to validate models of CR electron acceleration and to explore whether observations can be explained by leptonic or hadronic interactions. Hence, this work opens up a new capability for MHD simulations of dynamical systems that can be compared to radio, X-ray, and  $\gamma$ -ray observations. I apply `CREST` to three-dimensional MHD simulations of the supernova remnant of SN 1006. These show that a mixed leptonic-hadronic model explains best the observed  $\gamma$ -ray emission and that CR electrons, similar to CR protons, are preferentially accelerated in environments where the shock direction is quasi-parallel to the upstream magnetic field. In addition, the simulations show that a magnetic field amplification by a volume-filling turbulent dynamo is required and that the Bell amplification needs to be spatially confined to the shock. Both findings are necessary in order to match simultaneously radio, X-ray, and  $\gamma$ -ray observations.



## **Über die Entwicklung und die beobachtbaren Charakteristiken von Elektronen der kosmischen Strahlung in magnetohydrodynamischen Simulationen**

Elektronen der kosmischen Strahlung (CR Elektronen) sind allgegenwärtig im Universum und liefern Schlüsselerkenntnisse über die nicht-thermische Physik. Ihre Synchrotron-, Brems- und inverse Compton-Strahlung geben Aufschluss über das interstellare Medium, über Galaxien und galaktische Ausflüsse, über Galaxienhaufen und über aktive galaktische Kerne. Modelle dieser Emissionsprozesse können mithilfe von magnetohydrodynamischen (MHD) Simulationen gegen Beobachtungen geprüft werden. Während die dynamisch wichtigen CR Protonen häufig einbezogen werden, werden CR Elektronen selten betrachtet, da deren Behandlung eine detaillierte spektrale Modellierung aufgrund komplexer Hystereseeffekten benötigt. Im Rahmen dieser Arbeit habe ich den effizienten Nachbearbeitungscode `CREST` entwickelt, der Elektronenspektren zeitlich und räumlich aufgelöst entwickelt. Dies erlaubt einen Vergleich der Emissionscharakteristiken von CR Elektronen mit Beobachtungen anhand von Multi-Frequenzspektren und der Morphologie. Ferner ermöglicht `CREST`, Beschleunigungsmodelle der CR Elektronen zu überprüfen, und zu untersuchen, ob Beobachtungen mit leptonischen oder hadronischen Wechselwirkungen erklärt werden können. Diese Arbeit eröffnet somit eine neue Möglichkeit für MHD Simulationen von dynamischen Systemen, die gleichzeitig mit Radio-, Röntgen- und  $\gamma$ -Strahlungsbeobachtungen verglichen werden können. Ich wende `CREST` auf dreidimensionale MHD Simulationen des Supernovaüberrests von SN 1006 an. Diese Simulationen zeigen, dass ein gemischtes leptonisch-hadronisches Modell die beobachtete  $\gamma$ -Strahlung am besten erklärt und dass CR Elektronen, ähnlich wie CR Protonen, bevorzugt in Umgebungen beschleunigt werden, in denen die Stoßrichtung quasi-parallel zum Magnetfeld stromaufwärts ist. Die Simulationen zeigen zudem, dass eine Magnetfeldverstärkung durch einen volumenfüllenden, turbulenten Dynamo benötigt wird und dass die sogenannte Bellsche Verstärkung räumlich eng an die Stoßfront gebunden sein muss. Beides ist notwendig, um einen gleichzeitigen Angleich an Radio-, Röntgenstrahlungs- und  $\gamma$ -Strahlungsbeobachtungen zu erzielen.



# Contents

<b>List of Figures</b>	<b>XIII</b>
<b>List of Tables</b>	<b>XV</b>
<b>1 Introduction</b>	<b>1</b>
<b>2 Theoretical Background</b>	<b>3</b>
2.1 Cosmic Rays . . . . .	3
2.1.1 Transport . . . . .	3
2.1.2 Fermi-I Acceleration . . . . .	5
2.1.3 Leptonic Losses . . . . .	9
2.1.4 Hadronic Losses . . . . .	11
2.2 Magnetohydrodynamical Simulations . . . . .	12
2.2.1 Ideal MHD . . . . .	13
2.2.2 MHD with Cosmic Rays . . . . .	15
2.2.3 Shocks . . . . .	17
2.3 Supernova Remnants . . . . .	19
2.3.1 Classification . . . . .	19
2.3.2 Evolution of Supernova Remnants . . . . .	20
<b>3 The CREST Code</b>	<b>23</b>
3.1 Implementation Strategy . . . . .	23
3.2 MHD Simulations with CR Electrons . . . . .	25
3.3 CREST - Cosmic Ray Electron Spectra Evolution in Time . . . . .	28
3.3.1 Structure of the Code . . . . .	28
3.3.2 Numerical Solution to the Fokker–Planck Equation . . . . .	30
<b>4 Evolution of Cosmic Ray Electron Spectra in Magnetohydrodynamical Simulations</b>	<b>39</b>
4.1 Introduction . . . . .	39
4.2 Methodology . . . . .	42
4.2.1 Theoretical Background . . . . .	42
4.2.2 Numerical Discretisation . . . . .	46
4.2.3 Analytical Solutions . . . . .	50

4.3	Idealised One-Zone Tests . . . . .	56
4.3.1	Adiabatic Changes . . . . .	56
4.3.2	Freely Cooling Spectrum . . . . .	57
4.3.3	Steady-State Spectrum . . . . .	59
4.3.4	Fermi-II Reacceleration . . . . .	60
4.4	Hydrodynamical Simulations . . . . .	61
4.4.1	Shock Tubes . . . . .	62
4.4.2	Sedov–Taylor Blast Wave . . . . .	66
4.5	Conclusions . . . . .	69
<b>5</b>	<b>Evolution and Observational Signatures of the Cosmic Ray Electron Spectrum in SN 1006</b>	<b>71</b>
5.1	Introduction . . . . .	71
5.2	Simulation Setup . . . . .	73
5.2.1	Simulation Codes . . . . .	73
5.2.2	Magnetic Obliquity-Dependent Acceleration . . . . .	75
5.2.3	Initial Conditions . . . . .	76
5.2.4	Magnetic Modelling . . . . .	77
5.2.5	Non-Thermal Radiative Transfer . . . . .	79
5.3	Leptonic versus Hadronic Model . . . . .	80
5.3.1	Multi-Frequency Spectrum . . . . .	80
5.3.2	Non-Thermal Emission Morphologies . . . . .	83
5.4	Obliquity-Dependent Acceleration . . . . .	86
5.4.1	Quasi-Parallel Acceleration Efficiency . . . . .	86
5.4.2	Constant Acceleration Efficiency . . . . .	86
5.4.3	Quasi-Perpendicular Acceleration Efficiency . . . . .	89
5.5	Amplification and Damping of Magnetic Fields . . . . .	89
5.5.1	Turbulent Magnetic Amplification . . . . .	89
5.5.2	Magnetic Amplification via the Bell Instability . . . . .	92
5.6	Parameter Dependencies . . . . .	93
5.6.1	Spectral Index of CRs . . . . .	93
5.6.2	Magnetic Amplification and Maximum Momentum . . . . .	96
5.6.3	Ambient Photon Field and Density . . . . .	98
5.7	Discussion and Conclusion . . . . .	101
<b>6</b>	<b>Conclusions and Outlook</b>	<b>103</b>
6.1	Conclusions . . . . .	103
6.2	Outlook . . . . .	104

**First Author Publications of G. Winner** **i**

**Bibliography** **iii**

<b>A Appendix</b>	<b>xxv</b>
<b>Danksagung</b>	<b>xxvii</b>



# List of Figures

2.1	Shock Tube Test for a Strong Shock with $\mathcal{M} = 10$ . . . . .	18
3.1	CREST Flowchart . . . . .	28
3.2	Advection Test for Adiabatic Expansion . . . . .	31
4.1	Characteristic Time-Scales for Electron Cooling . . . . .	51
4.2	Comparison between Exact and Approximate Formulae for Coulomb Losses . . . . .	52
4.3	Adiabatic Expansion of an Initial Power-Law Spectrum . . . . .	57
4.4	Freely Cooling Power-Law Spectrum . . . . .	58
4.5	Energy-Weighted Relative L1 Errors for Cooling, Steady-State and Fermi-II Reacceleration Tests . . . . .	58
4.6	Build up of a Steady-State Spectrum . . . . .	59
4.7	Fermi-II Reacceleration with and without Cooling . . . . .	60
4.8	1D Shock-Tube Test of a Strong Shock . . . . .	61
4.9	Histograms of the Compression Ratio and Spectral Index . . . . .	62
4.10	Tracer Particle Resolution Study for 1D Shock Tubes . . . . .	63
4.11	CR Electron Spectra for 1D and 3D Shock-Tube Simulations . . . . .	64
4.12	Comparison of Direct Acceleration and Reacceleration . . . . .	65
4.13	3D Sedov–Taylor Blast-Wave Simulation . . . . .	67
4.14	Tracer Particle Density and Spectra for 3D Sedov–Taylor Blast-Wave Simulation . . . . .	67
5.1	Obliquity-Dependent Electron Acceleration Efficiency . . . . .	74
5.2	Magnetic Field Morphology in a Slice through the Centre of our Simulated Remnant . . . . .	77
5.3	Best-Fit Multi-Frequency Spectrum of SN 1006 . . . . .	80
5.4	Morphological Comparison of our Best-Fit Simulation with Preferred Quasi-Parallel Acceleration . . . . .	81
5.5	Angular Dependency of Synchrotron Emission and Adiabatically Compressed Magnetic Field . . . . .	82
5.6	$\gamma$ -Ray Maps of our Best-Fit Quasi-Parallel Acceleration Model . . . . .	82
5.7	Morphological Comparison of our Simulation with Constant Acceleration . . . . .	87
5.8	Morphology of the Simulations with Preferred Quasi-Perpendicular Acceleration Efficiency . . . . .	88
5.9	Multi-Frequency Spectra of Models with Short-Range and Long-Range Bell-Amplified Magnetic Fields . . . . .	90

## List of Figures

---

5.10	Morphology of Simulations with a Long-Range Bell-Amplified Magnetic Field . . . . .	91
5.11	Multi-Frequency Spectra and Radial Profiles for Different Decay Models of the Bell-Amplified Magnetic Field . . . . .	92
5.12	Total $\gamma$ -ray Spectra and Hadronic $\gamma$ -ray Spectra for Different CR Proton Spectral Indices . . . . .	94
5.13	Multi-frequency Spectra and CR electron spectra for Different CR Electron Spectral Indices . . . . .	94
5.14	Multi-Frequency Spectra for Different Magnetic Fields, Bell Amplification Factors, and Maximal Acceleration Momenta . . . . .	96
5.15	Best-Fit Multi-Frequency Spectra and Parameter Space Study . . . . .	97
5.16	High Energy $\gamma$ -ray Spectrum and Interstellar Radiation Fields . . . . .	99
5.17	High Energy $\gamma$ -ray Spectrum for Varying Ambient Gas Densities . . . . .	99
A.1	Multi-Frequency spectra and Relative Error . . . . .	xxvi

# List of Tables

3.1	Example of the Header File of a Tracer Particle Output . . . . .	25
3.2	Example of a Data Block in a Tracer Particle Data File . . . . .	26
3.3	An Example of the CREST Spectrum Output . . . . .	29
4.1	Initial Values of Shock-Tube Setups . . . . .	62
5.1	Resolution per Box Length in Shells from the Centre . . . . .	77



# 1 Introduction

The research on cosmic rays (CRs), which started with Victor Hess' balloon flights in 1912, has developed into an important branch of astrophysics because it provides insights into the non-thermal physics of many environments such as the interstellar medium (ISM), galaxies, galaxy clusters, and active galactic nuclei (AGN). CRs are charged particles that emerge from the thermal pool and move with relativistic velocities around magnetic fields. CRs are composed of about 90 per cent protons, 9 per cent alpha particles, 1 per cent electrons, and the rest are heavier nuclei and antiparticles. Their kinetic energies span several orders of magnitude from below their rest mass up to almost  $10^{20}$  eV for heavy nuclei.

CRs can be observed at earth with a plethora of experiments, that are earth-bound (air shower arrays, imaging atmospheric Cherenkov telescopes, neutrino detectors), space-based particle spectrometers, or balloon-borne detectors. Information about CRs in remote environments can be obtained through their non-thermal emission which are synchrotron radiation, inverse Compton emission and bremsstrahlung of CR electrons and  $\gamma$ -rays from hadronic interactions of CR protons. The resulting radiation can be observed with radio telescopes and interferometer arrays, X-ray satellites, and  $\gamma$ -ray telescopes and satellites.

Despite the enormous amount of collected data, the origin of CRs remains unclear. The ultra high energetic range of CRs must be of extragalactic origin and CRs with up to  $10^{15}$  eV are believed to originate from supernova remnants (SNRs) in our Galaxy. In this thesis, I will focus on the latter and the leptonic CR component.

The hadronic component of CRs to which we refer as CR protons plays an important dynamical role. CR protons are in energy equipartition with turbulent and magnetic energy in the midplane of the Galaxy (Boulares and Cox, 1990) and are therefore important for the dynamics of the ISM. Although CRs can interact in principle with the thermal gas via particle collisions in principle, CRs with a few GeV which carry the bulk of the total CR energy are collisionlessly coupled to the gas via efficient scattering off MHD waves. An important mechanism is the scattering off self-excited Alfvén waves by streaming of CRs down their own pressure gradient. The energy of CRs can be transferred to thermal energy via the damping of these resonantly excited Alfvén waves. This CR heating source could be a key to solve the "cooling flow problem" in galaxy clusters (McNamara and Nulsen, 2007; Guo and Oh, 2008; Pfrommer, 2013; Jacob and Pfrommer, 2017a,b). As CRs stream and diffuse along open field lines into the Galactic halo, a CR pressure gradient is build up which can become dominant over gravitational attraction thereby accelerating the gas and driving a strong Galactic outflow (Zweibel, 2017; Naab and Ostriker, 2017). CR protons become visible through  $\gamma$ -ray emission due to hadronic interaction with the gas.

The leptonic component of CRs to which we refer as CR electrons are not dynamically important as their energy content is smaller in comparison to CR protons by a factor of around 50 to 100 at the solar radius in the Milky Way (Zweibel, 2013). CR electrons cool quickly via Coulomb interaction and bremsstrahlung as they move through the ambient gas, synchrotron radiation as they spiral around magnetic fields, and via inverse-Compton interactions with ambient photon fields. These radiation mechanisms link CR physics with observations and give us insights into remote astrophysical systems, e.g. SNRs in our Galaxy, radio relics and mini halos in galaxy clusters, and the Fermi bubbles as a likely prominent example of a galactic outflow. SNRs are of central importance as their shock fronts accelerate CR protons and electrons.

In the last two decades, magnetohydrodynamical (MHD) simulations have become an important tool to study the dynamical influence of CRs because they allow to self-consistently model the interplay between gas, magnetic fields, and CRs. CR protons are included as a relativistic fluid whose energy evolves on a separate equation and can exchange energy with the thermal gas. This treatment is sufficient to study the dynamical impact of CRs. However, it is inevitable to track the evolution of the CR electron spectrum as it determines the synchrotron, bremsstrahlung, and inverse Compton spectra. In addition, the CR electron spectrum is shaped by acceleration, cooling, and reacceleration such that the exact history of these events is important.

This thesis covers the evolution of the CR electron spectrum alongside MHD simulations. I have developed an efficient numerical code called `CREST` which stands for Cosmic Ray Electron Spectra evolved in Time. First, I introduce the theoretical background of CR physics and MHD simulations together with a discussion about SNRs. Then in Chapter 3, I present the scope of this code by discussing possible implementation strategies and how it is coupled to the moving-mesh MHD code `AREPO`. In addition, I layout the general structure of the code and how numerical solutions to the Fokker-Planck equation, i.e. the governing transport equation of CR electrons, are obtained. In Chapter 4, I proceed with an in-depth presentation of `CREST` and show a variety of tests ranging from idealized one zone models to hydrodynamical simulations. These validate that this work together with the documentation of `CREST` enables future studies on CR electrons in the ISM, galaxies, galaxy clusters and AGNs. Finally in Chapter 5, I apply `CREST` to MHD simulations of the supernova remnant SN 1006 which links microscopic plasma insights obtained from kinetic particle-in-cell (PIC) simulations to global MHD scales. The analysis enables to test our understanding of plasma physics in a novel way by detailed comparison to non-thermal observations from radio to X-rays to  $\gamma$ -rays. I conclude this thesis in Chapter 6 by summarizing my results and presenting future applications of this work.

## 2 Theoretical Background

This chapter presents the essential theoretical background of CR physics and transport. We first introduce the physics of CRs in section 2.1. Secondly, we describe MHD simulations, the `AREPO` code, and the CR code module in section 2.2. Thirdly, we review the evolution of SNR that are an important source of CR acceleration in our Galaxy in section 2.3.

### 2.1 Cosmic Rays

The existence of cosmic rays has been well established for more than 100 years. In the year 1912, balloon experiments by Victor Hess showed that ionizing radiation increases with altitude suggesting a cosmic origin (Hess, 1912). Ground-based experiments (e.g. KASCADE, Auger, Telescope Array), balloon-borne experiments (e.g. ATIC, CREAM, BESS), and space-based experiments (PAMELA, AMS-02) have shown that the total energy per nucleon of CRs spans approximately 11 orders of magnitude from  $10^9$  eV to  $10^{20}$  eV (e.g. Gaisser et al., 2016). The spectrum is described by piecewise power laws  $N(E) \propto E^{-\alpha}$  from  $10^{10}$  eV to  $10^{15}$  eV with the spectral index  $\alpha \approx 2.7$ , from  $10^{16}$  eV to  $10^{18}$  eV with the softer index  $\alpha \approx 3.1$ , and above  $1 \times 10^{19}$  with a harder index  $\alpha \approx 2.6$ . It is modified below  $10^{10}$  eV by solar modulation. The spectrum shows two distinct features that are the so-called knee at  $\sim 3 \times 10^{15}$  eV and ankle at  $\sim 3 \times 10^{15}$  eV where the spectral index of the spectrum changes.

This work focuses on the spectrum up energies of a few tens of TeV which contains the bulk of the total CR energy and which are responsible for emission from radio, X-rays to  $\gamma$ -rays. This section presents an overview of the fundamental physics of CRs and contains adapted text from section 2.1 of our publication in Winner et al. (2019).

#### 2.1.1 Transport

The distribution of CRs consist of protons and electrons can be characterized by their phase space coordinates, position  $\mathbf{x}$  and momentum  $\mathbf{p}$ . We use the dimensionless momentum  $\mathbf{p}_p = \mathbf{P}_p/(m_p c)$  for CR protons and  $\mathbf{p}_e = \mathbf{P}_e/(m_e c)$  for CR electrons, where  $m_p$  and  $m_e$  are the proton and electron rest mass, respectively, and  $c$  is the speed of light. The distribution function  $f_i(\mathbf{x}, \mathbf{p}, t)$  for each specie is described by the relativistic Vlasov equation

$$\frac{\partial f_i}{\partial t} + \dot{\mathbf{x}}_i \cdot \nabla f_i + \dot{\mathbf{p}}_i \cdot \nabla_{\mathbf{p}_i} f_i = \left. \frac{\partial f_i}{\partial p_i} \right|_c \quad i \in \{p, e\} \quad (2.1)$$

where the collisional term  $\partial f / \partial p|_c$  represents sources and sinks of particles and  $\dot{\mathbf{p}}_i$  is the Lorentz force

$$\dot{\mathbf{p}}_i = \frac{Ze}{m_i c} \left[ \mathbf{E}(\mathbf{x}, t) + \frac{\mathbf{v} \times \mathbf{B}(\mathbf{x}, t)}{c} \right] \quad (2.2)$$

with electric field  $\mathbf{E}$ , magnetic field  $\mathbf{B}$ , and charge  $Ze$ . The large scale electric field can be neglected due to high electrical conductivity of astrophysical plasmas. In a uniform magnetic field, the particles gyrate around the field lines with a gyrofrequency of

$$\Omega_i = \frac{e|\mathbf{B}|}{\gamma_i m_i c} \quad (2.3)$$

where  $\gamma_i = \sqrt{1 + p_i^2}$  is the Lorentz factor. In the following, we drop the index  $i$  for protons and electrons and only mention it if we refer to a specific species.

However, the distribution function as well as the particle motions are influenced by randomly fluctuating magnetic fields. By frequent scattering off the ubiquitous MHD waves, the pitch angle, i.e. the angle between the momentum and magnetic field, is isotropized. The Fokker–Planck equation can be derived by a perturbation method with a quasi-linear approximation (Skilling, 1975; Schlickeiser, 1989a; Zank, 2014). The distribution function  $f$  is generally influenced by the Lorentz force of fluctuating MHD fields. As individual fluctuations are of minor importance, the distribution function is ensemble averaged over these fluctuations. It is further assumed that the MHD fluctuations are small in amplitude such that particles move approximately on their undisturbed gyro orbits on a particle correlation time and such that the distribution function is gyrotropic (isotropic in gyrophase). In addition, the timescale of MHD fluctuations which lead to pitch-angle scattering has to be much larger than the correlation time and much shorter than the time on which the ensemble average can react. The distribution function is then split into an unperturbed and a perturbed component on which the influence of MHD fluctuations are worked out. We include continuous losses plus a source term (Kirk et al., 1988; Schlickeiser, 1989b) such that the transport equation for the 3D CR distribution takes the form

$$\frac{\partial f}{\partial t} + (\mathbf{v} + \mathbf{v}_{\text{st}}) \cdot \nabla f = \nabla \cdot [\mathbf{K} \cdot \nabla f] + \frac{p}{3} \frac{\partial f}{\partial p} \nabla \cdot (\mathbf{v} + \mathbf{v}_{\text{st}}) + \frac{1}{p^2} \frac{\partial}{\partial p} \left[ p^2 D_{pp} \frac{\partial f}{\partial p} \right] + S(p) \quad (2.4)$$

where  $p = |\mathbf{p}|$  is the absolute value of the normalized momentum. In addition,  $\mathbf{v}$  is the velocity of the background plasma and  $\mathbf{v}_{\text{st}} = -v_A \text{sgn}(\mathbf{B} \cdot \nabla f)$  is the streaming velocity of CRs with the Alfvén velocity  $v_A = \mathbf{B} / \sqrt{4\pi\rho}$  in the plasma with mass density  $\rho$ . Furthermore,  $\mathbf{K}$  and  $D_{pp}$  are the spatial and momentum diffusion, respectively. The source and sink term  $S$  is given by

$$S(p) = Q(p) - \frac{1}{p^2} \frac{\partial}{\partial p} \left( p^2 \dot{p} f \right) - \frac{f}{\tau_c} \quad (2.5)$$

where  $Q(p)$  is an injection source,  $\dot{p}$  is a cooling term, and  $\tau_c$  is the timescale of catastrophic losses, e.g. spallation reactions of CR protons. In the case of CR electrons,  $Q(p)$  describes injection of secondary electrons that result from hadronic interactions of CR protons. We note that Equation (2.4) gives the evolution of the distribution function  $f^{3D}$  in 3D momentum space with number and kinetic energy density

$$n = \int f^{3D}(p) 4\pi p^2 dp, \quad (2.6)$$

$$\varepsilon = \int E_{\text{kin}}(p) f^{3D}(p) 4\pi p^2 dp, \quad (2.7)$$

respectively, where  $E_{\text{kin}}(p) = (\sqrt{1 + p^2} - 1)mc^2$  is the kinetic energy. It is convenient to transform the transport equation into 1D momentum space via the relation  $f^{1D} = 4\pi p^2 f^{3D}$  which is often used in the literature and will be used in following chapters.

### 2.1.2 Fermi-I Acceleration

CRs are accelerated from particles of the thermal pool at astrophysical shocks, e.g. at the expanding shock front of SNRs, at the shocks of AGNs, at cluster and merger shocks. These shocks can additionally reaccelerate a previously existing CR population. In the original idea proposed by Fermi (1949), particles frequently scatter off moving magnetized clouds in the ISM with velocity  $v$ . The particles are reflected due to magnetic mirroring at magnetic irregularities in these clouds which are produced by turbulent motions from winds, shocks, and energetic particles traveling through the clouds. As head-on collisions are more probable than tail-on collisions, frequent scattering results in mean energy increase of the order  $\beta^2 = (v/c)^2$  per scattering event. It is a slow acceleration process due to the second order in  $\beta$  with  $\beta \ll 1$ . Therefore, particles need sufficient energy to gain more energy than they lose through ionization and Coulomb losses at the same time which makes this acceleration inefficient for heavy ions of the CRs.

Diffusive shock acceleration (DSA) is a more efficient first-order acceleration process modifying Fermi's original idea which takes place in converging flows of astrophysical shocks (Krymskii, 1977; Axford et al., 1977; Bell, 1978b; Blandford and Ostriker, 1978). Particles gain energy by crossing multiple times back and forth the shock front while being scattered at magnetic irregularities due to wave-particle interaction. The dissipated thermal energy is partially (up to 10 to 15 per cent) converted into the acceleration of CRs. These accelerated particles can themselves drive MHD waves off which they scatter. The maximum attainable energy depends on the size and the magnetic field strength of the acceleration site as the magnetic field-dependent Larmor radius of the accelerated particle  $r_g = pc/(qB)$  has to be smaller than the confinement radius (Hillas, 1984). The maximum energy of electrons is limited by simultaneous cooling losses (Zirakashvili and Aharonian, 2007).

We first discuss a macroscopic picture of Fermi-I acceleration and secondly, present result from kinetic simulations of CR proton and electron acceleration.

### Macroscopic Picture of Fermi-I Acceleration

We follow the approach by Drury (1983) and consider a plane-parallel shock moving (non-relativistically) along the  $x$ -direction with a sharp shock transition layer which is much smaller than the CR diffusion length  $D/v$ . In the shock rest frame, the shock is located at  $x = 0$  and lies in the  $y$ - $z$  plane. The fluid flows along the positive  $x$ -direction and the velocity is

$$v(x) = \begin{cases} v_1 & \text{for } x < 0, \\ v_2 & \text{for } x > 0, \end{cases} \quad (2.8)$$

where the indices 1 and 2 denote upstream and downstream quantities, respectively. The shock compression ratio, i.e. the ratio of downstream to upstream density, is  $r = \rho_2/\rho_1$ . Using the Rankine–Hugoniot (see Section 2.2.3), it can be expressed as

$$r = \frac{\rho_2}{\rho_1} = \frac{v_1}{v_2} = \frac{\gamma + 1}{\gamma - 1 + 2/\mathcal{M}^2} \quad (2.9)$$

with adiabatic index  $\gamma$  (assuming  $\gamma = \gamma_1 = \gamma_2$ ) and (upstream) Mach number  $\mathcal{M} = v_1/c_{s,1}$  which is the ratio of velocity to sound speed in the upstream. For an ideal mono-atomic gas where no internal degrees of freedom are excited by the shock and for a strong shock with  $\mathcal{M} \gg 1$ , the compression ratio approaches the value  $r = 4$ .

We assume the system to be stationary and further neglect streaming, Fermi-II acceleration, and cooling such that the transport equation (2.4) reduces to a diffusion-advection equation

$$v \frac{\partial f}{\partial x} = \frac{\partial}{\partial x} \left[ K \frac{\partial f}{\partial x} \right] + \frac{p}{3} \frac{\partial f}{\partial p} \frac{\partial v}{\partial x} + v_1 q(p) \delta(x) \quad (2.10)$$

where we included a source term located at the shock front  $x = 0$  (Pfrommer, 2005). We take the general solution of the form

$$f(x, p) = g_1(p) + g_2(p) \exp \left( \int_0^x \frac{v(x')}{K} dx' \right) \quad (2.11)$$

and impose that the far upstream spectrum has a distribution function  $\lim_{x \rightarrow -\infty} f(x, p) = f_1(p)$  and that the downstream spectrum  $f_2$  is finite. The second term in Equation (2.11) is the diffusion term which balances the incoming flux in the upstream region ( $x < 0$ ) and yields a steady state spectrum. As it yields a growing infinite solution in the downstream region ( $x > 0$ ), the diffusion term has to be zero and the spectrum is spatially constant. We further impose that the solution has to be continuous at the shock transition layer such that the solution is given by

$$f(x, p) = \begin{cases} f_1(p) + [f_2(p) - f_1(p)] \exp \left( - \int_x^0 \frac{v_1}{K} dx' \right) & \text{for } x < 0, \\ f_2(p) & \text{for } x \geq 0. \end{cases} \quad (2.12)$$

In order to obtain the solution for the downstream spectrum, Equation (2.10) has to be integrated across the shock from  $-\epsilon$  and  $\epsilon$  and evaluated in the limit  $\epsilon \rightarrow 0$ . We obtain the following differential equation

$$p \frac{\partial f}{\partial p} = \frac{3r}{r-1} [f_1(p) + q(p) - f_2(p)] \quad (2.13)$$

where we have taken the shock compression ratio of Equation (2.9). The solution for  $f_2(p)$  is given by

$$f_2(p) = \alpha p^{-\alpha} \int_0^p dp' [f_1(p') + q(p')] p'^{\alpha-1} \quad (2.14)$$

with the spectral index  $\alpha = 3r/(r-1)$ . This can be interpreted as reacceleration of the previously existing upstream spectrum and new acceleration of particles from the thermal pool. It is independent of the spatial diffusion coefficient and depends only on the shock compression ratio. If we consider the source function to have the form  $q(p) = q_0 \delta(p - p_{\text{inj}})$  with an injection momentum  $p_{\text{inj}}$  and neglect a far upstream spectrum  $f_1$ , the downstream spectrum due to particles accelerated at the shock becomes

$$f_2(p) = \frac{q_0 \alpha}{p_{\text{inj}}} \left( \frac{p}{p_{\text{inj}}} \right)^{-\alpha}. \quad (2.15)$$

In a strong shock in a fluid with  $\gamma_{\text{th}} = 5/3$ , the shock compression ratio is  $r = 4$  and the spectral index is  $\alpha_{3D} = 4$  for a 3D momentum space distribution function. For a 1D momentum space distribution function with  $f^{1D} = 4\pi p^2 f^{3D}$ , the spectral index is  $\alpha_{1D} = 2$ .

### Kinetic Simulations of Fermi-I Acceleration

As mentioned before, the acceleration of particles from the thermal pool to typical CR energies is achieved by frequent scattering of particles at magnetic irregularities at shocks. Their dynamics can be studied in kinetic particle-in-cells (PIC) simulations which cover all relevant microphysical processes necessary for CRs. These type of simulations evolve the equations of motions for individual macroparticles of electrons and protons in electric and magnetic fields (Charles K. Birdsall, 1985). These fields are evaluated according to Maxwells equations on a grid and are generated by the charge distributions and their currents themselves. As the evolution of all these processes is computationally expensive, current PIC simulations cover physical time-scales on the order of seconds to a few minutes for number densities of the order of  $n \approx 1 \text{ cm}^{-3}$ .

In contrast to full PIC simulations, hybrid simulations treat electrons as a massless neutralizing fluid (Lipatov, 2002) while self-consistently capturing shock evolution and plasma instabilities in MHD approximation, i.e. neglecting displacement currents. Hybrid simulations are successful at modeling ion acceleration at non-relativistic shocks (Caprioli

and Spitkovsky, 2014a,b,c, for a review see Caprioli, 2015). They find that more than 10 per cent of the shock ram kinetic energy can be converted into the acceleration of CRs with a power-law tail for quasi-parallel shocks. Quasi-parallel shocks are characterized by  $\theta \lesssim 45^\circ$  where  $\theta$  is the obliquity angle between the shock normal and the far upstream magnetic field. For quasi-perpendicular shocks with  $\theta \gtrsim 45^\circ$ , the acceleration efficiency of ions is strongly reduced. The acceleration of ions from the thermal pool involves three stages (Caprioli et al., 2015). First, the ions incoming from upstream get reflected by the shock electrostatic potential barrier and gyrate back into the upstream medium leading to the formation of a new barrier. Secondly, the ions experience shock drift acceleration (SDA) in convective electric fields and the probability of an ion to participate in  $N$  cycles of SDA is  $\sim 0.25^N$ . A fraction of ions which is about one per cent at quasi-parallel shocks reaches the injection energy of  $E_{\text{inj}} \sim mv_{\text{sh}}^2$  for diffusive shock acceleration where  $v_{\text{sh}}$  is the shock speed. Thirdly, ions experience DSA while crossing the shock multiple times and being scattered on self-generated magnetic fluctuations. These fluctuations originate from the non-resonant hybrid instability (Bell, 2004), also known as the Bell instability.

So far, there is no comprehensive theory of electron injection into DSA (Caprioli, 2015; Xu et al., 2019). There are two problems with the injection of electrons. First, they have significantly smaller Larmor radii than the shock transition width such that they cannot cross the shock in order to participate in DSA. Secondly, the electrostatic shock potential barrier with an upstream-directed electric field hinders electron reflection. The preacceleration and injection of electrons into DSA is studied with full PIC simulations where the electrons are not treated as a fluid. Full PIC simulations are computationally more expensive than hybrid simulations due to the large proton to electron mass ratio of  $m_p/m_e \approx 1836$ . They must resolve timescales from the inverse of the electron plasma-frequency  $\omega_{\text{pl,e}}^{-1} = (4\pi e^2 n_e/m_e)^{-1/2}$  to the inverse of the proton cyclotron frequency  $\omega_{\text{c,p}}^{-1} = (eB/[m_p c])^{-1}$  which leads to the relation (Riquelme and Spitkovsky, 2011)

$$\frac{\omega_{\text{pl,e}}}{\omega_{\text{c,p}}} = \frac{v_A}{c} \sqrt{\frac{m_p}{m_e}}. \quad (2.16)$$

Simulations can be made feasible if a reduced mass ratio of  $m_p/m_e = 100 - 400$  is assumed. Often the dimensionality is reduced to 1D or 2D and the magnetic field has an out-of-plane configuration. Acceleration at high Mach number quasi-parallel shock has been found in 1D, full PIC simulations (Kato, 2015; Park et al., 2015). In the simulations of Park et al. (2015), the electrons are preheated via SDA, gain further energy via SDA and Fermi-like acceleration, and finally get injected into DSA. Electrons as well as protons scatter off waves that are excited via the non-resonant hybrid instability.

PIC simulations of quasi-perpendicular shocks with low Mach numbers find electron acceleration that is driven by the oblique firehose instability. (Guo et al., 2014a,b). Non-relativistic quasi-perpendicular shocks are able to preaccelerate electrons (Riquelme and Spitkovsky, 2011; Bohdan et al., 2017) and inject electrons into DSA with a power-law spectrum in the downstream (Xu et al., 2019). In the latter, it is found that electrons

drive non-resonant waves in the upstream after reflection at the shock front. Thereby, they enable trapping of electrons between the shock and self-excited waves such that they undergo multiple cycles of SDA before injection into DSA.

### 2.1.3 Leptonic Losses

CR electrons lose their energy via multiple processes, i.e. Coulomb, bremsstrahlung, synchrotron and inverse Compton losses. These processes act on much smaller timescales than that of CR protons. They lead to observable radiation which is important to study CR physics in remote astrophysical environments. Formulae are adopted from Blumenthal and Gould (1970), Rybicki and Lightman (1986), and Longair (2012) if not stated otherwise.

#### Coulomb Losses

CR electrons that move through an ionized plasma lose energy by scattering off electrons of the plasma. Thereby, CR electrons transfer kinetic energy to the plasma and act as a heating source of the plasma. The Coulomb loss rate of CR electrons (Gould, 1975) is given by

$$\dot{p}_c(p) = -\frac{3\sigma_T n_e c}{2\beta^2} \left[ \ln\left(\frac{m_e c^2 \beta \sqrt{\gamma-1}}{\hbar \omega_{pl}}\right) + \ln(2) \left(\frac{\beta^2}{2} + \frac{1}{\gamma}\right) + \frac{1}{2} + \left(\frac{\gamma-1}{4\gamma}\right)^2 \right], \quad (2.17)$$

where  $\sigma_T = 8\pi e^4 (m_e c^2)^{-2}/3$  is the Thomson cross-section,  $\hbar$  is the reduced Planck constant,  $m_e$  the electron mass,  $\beta = p(1+p^2)^{-1/2}$  is the dimensionless CR electron velocity, and  $\gamma = (1+p^2)^{1/2}$  is the Lorentz factor of CR electrons. The electron density is  $n_e = n_{\text{gas}} X_H x_e$  where  $X_H$  is the hydrogen mass fraction and  $x_e = n_e/n_H$  is the ionization fraction, the ratio of electron density-to-hydrogen density, which is denoted by  $n_H$ . The plasma frequency is  $\omega_{pl} = \sqrt{4\pi e^2 n_e/m_e}$  and  $e$  denotes the elementary charge. The Coulomb loss rate has only a weak dependency on the electron momentum for  $p > 1$  due to the slowly varying logarithm in the loss rate.

#### Relativistic Bremsstrahlung

Another loss process is bremsstrahlung of CR electrons moving through the electrostatic potential of a nucleus and thereby emitting radiation. This process is also known as free-free emission which corresponds to the transition between two unbound states of an atom. In the rest frame of the electron, an electromagnetic pulse is emitted by the approaching nucleus and the virtual photons scatter off the electron. The momentum loss rate of CR electrons due to bremsstrahlung is given by

$$\dot{p}_b(p) = -\frac{16}{3} \alpha \left(\frac{e^2}{m_e^2 c^3}\right)^2 \gamma \chi [E(p)], \quad (2.18)$$

where  $\alpha \approx 1/137$  is the fine-structure constant. The loss rate also depends on the total cross section  $\chi[E(p)]$  which is given in Koch and Motz (1959). Relativistic bremsstrahlung becomes important for high density environments and is negligible below  $n \lesssim 1 \text{ cm}^{-3}$ .

### Synchrotron Radiation

Electrons move in magnetic fields on circular orbits around the magnetic field lines due their Lorentz force (see Equation (2.2)). This permanent acceleration leads to synchrotron radiation that is responsible for radio emission, e.g. in our Galaxy or at SNRs (Rybicki and Lightman, 1986; Longair, 2012). It is also responsible for non-thermal X-ray emission. The loss term due to synchrotron radiation is given by

$$\dot{p}_s = -\frac{4\sigma_T p^2 B^2}{3m_e c \beta 8\pi} \quad (2.19)$$

where we have assumed an isotropic distribution of pitch angles  $\theta$ . The Thompson cross-section is given by  $\sigma_T = 8\pi r_e^2/3$  with the classical electron radius  $r_e = e^2/(m_e c^2)$ . While non-relativistic charged particles emit radiation at the non-relativistic gyrofrequency  $\nu_g = eB/(2\pi m_e)$ , relativistic particles emit synchrotron radiation that can be decomposed into harmonics of the relativistic gyrofrequency  $\nu_r = \nu_g/\gamma$ . The total emitted synchrotron power per unit volume and unit frequency at an angular frequency  $\omega$  is

$$P_s(\omega) = \frac{d^3 E}{dV d\omega dt} = \frac{\sqrt{3} e^3 B}{2\pi m_e c^2} \sin \theta \int_0^\infty dp \frac{p}{\sqrt{1+p^2}} f(p) F\left(\frac{\omega}{\omega_c}\right) \quad (2.20)$$

with a 1D electron spectrum  $f(p)$ , the critical frequency  $\omega_c = 3(1+p^2)eB \sin \theta/(3m_e c)$ , and the synchrotron Kernel  $F(x) = x \int_x^\infty K_{5/3}(y) dy$  where  $K_{5/3}$  is the modified Bessel function of second kind of order  $5/3$ . For a power law electron spectrum of the form  $f(p) \propto p^{-\alpha_e}$  with spectral index  $\alpha_e$ , the emitted synchrotron power obeys the proportionality  $P_{\text{tot}}(\omega) \propto \omega^{-\alpha_s}$  with the synchrotron spectral index of  $\alpha_s = (\alpha_e - 1)/2$ . Hence, the synchrotron spectrum gives insights into the shape of the electron spectrum and the magnetic field distributions.

### Inverse Compton

In contrast to Compton scattering, low energetic photons gain energy by scattering off CR electrons during the inverse Compton scattering process (Rybicki and Lightman, 1986; Longair, 2012). Together with hadronic  $\gamma$ -ray emission and non-thermal bremsstrahlung, inverse Compton emission is the source of high energy  $\gamma$  radiation. The loss term of a CR electron with Lorentz factor  $\gamma$  can be worked out in the rest frame of the electron. As long as the photon energy with frequency  $\omega$  in the electron rest frame is much smaller than the electron rest energy  $\gamma \hbar \omega \ll m_e c^2$ , inverse Compton scattering is simply Thompson scattering in this frame of reference. Working out the incident energy density of the

photon field in the electron rest frame and transforming back to the laboratory frame, the momentum loss rate of inverse Compton scattering is found to be

$$\dot{p}_{\text{ic}} = -\frac{4\sigma_{\text{T}}p^2}{3m_e c\beta} \varepsilon_{\text{ph}} \quad (2.21)$$

where  $\varepsilon_{\text{ph}}$  is the energy density of the photon field. The loss term is similar to that of synchrotron emission in Equation (2.20) which can be interpreted as electrons scattering of virtual photons from the magnetic field for synchrotron emission. Alternatively, the photon field of IC emission can be expressed by an equivalent magnetic field, which is  $B_{\text{CMB}} = \sqrt{8\pi\varepsilon_{\text{CMB}}(1+z)^2} \approx 3.24\mu\text{G}(1+z)^2$  for the CMB photon field with  $\varepsilon_{\text{CMB}} \approx 4.17 \times 10^{-13} \text{ eVcm}^{-3}$  at redshift  $z = 0$ .

We note that the loss rate contains the Thompson cross section  $\sigma_{\text{T}}$  which is only valid for  $\gamma\hbar\omega \ll m_e c^2$ , which corresponds to  $\gamma \ll 5 \times 10^8$  for CMB photons with  $\hbar\omega \approx 10^{-3} \text{ eV}$ . For larger electron or photon energies the Klein–Nishina cross-section

$$\sigma_{\text{KN}} = \pi r_e^2 \frac{1}{x} \left\{ \left[ 1 - \frac{2(x+1)}{x^2} \right] \ln(2x+1) + \frac{1}{2} + \frac{4}{x} - \frac{1}{2(2x+1)^2} \right\} \quad (2.22)$$

with  $x = \hbar\omega/(m_e c^2)$  has to be applied which approaches the Thompson cross-section for  $x \ll 1$ . It is interesting to note that the average energy of scattered photons for an isotropic distribution of CR electrons

$$\hbar\bar{\omega} = \frac{4}{3}\gamma^2\beta^2\hbar\omega_0 \approx \frac{4}{3}p^2\hbar\omega_0 \quad (2.23)$$

can be derived via dividing Equation (2.21) by the incident photon flux  $\sigma_{\text{T}}c\varepsilon_{\text{ph}}/(\hbar\omega_0)$ . It shows that CMB photons with  $E \approx 1 \times 10^{-3} \text{ eV}$  can be scattered to GeV energies by CR electrons with  $p \approx 10^6$ . The total emitted inverse Compton power per unit volume and frequency  $\nu$  is

$$P_{\text{ic}} = \frac{d^3E_{\text{ic}}}{dt dV d\nu} = 2\pi h E_{\text{ic}} r_e c^2 \int dp f(p) \frac{p}{(1+p^2)^{3/2}} \int \frac{dE}{E} n(E) F(q(E, E_{\text{ic}}, p)) \quad (2.24)$$

where  $f(p)$  is the electron spectrum and  $n(E)$  is the number density of the incident photon field. The auxiliary functions  $F(x)$  and  $q(E, E_{\text{ic}}, p)$  are

$$F(x) = 2x \ln x + x + 1 - 2x^2, \quad (2.25)$$

$$q(E, E_{\text{ic}}, p) = E_{\text{ic}} \left( 4E (1+p^2) \left[ 1 - \frac{E_{\text{ic}}}{\sqrt{1+p^2} m_e c^2} \right] \right)^{-1}. \quad (2.26)$$

### 2.1.4 Hadronic Losses

CR protons lose their energy due to Coulomb losses via scattering with plasma particles and hadronic interactions. Bremsstrahlung and synchrotron radiation are negligible for CR protons with energies  $E_p \lesssim 10^{18} \text{ eV}$  due the large proton to electron mass ratio which leads to large cooling time scales.

### Coulomb Losses

Similar to CR electrons, CR protons lose energy by traversing a plasma and scattering off electrons. The CR proton momentum loss term (Gould, 1972b) is given by

$$\dot{p}_c = \frac{4\pi e^4}{m_e m_p \beta^2 c^3} \left[ \ln \left( \frac{2m_e \beta p}{\hbar \omega_{pl}} \right) - \frac{\beta^2}{2} \right]. \quad (2.27)$$

The time-scales  $\tau = p/\dot{p}_c$  become small and important for small proton momenta  $p < 1$ . At larger momenta hadronic interactions become important.

### Hadronic Interactions

Hadronic interactions are an important momentum loss term of CR protons and lead to observational signature via  $\gamma$ -rays, production of secondary electrons and neutrinos (Longair, 2012; Gaisser et al., 2016). CR protons scatter inelastically on protons and nuclei of a plasma thereby producing neutral or charged pions if their momentum is larger than the pion production threshold of  $p_{\text{thr}} \approx 0.83$ . Due to baryon number conservation two protons or one proton and a neutron are remaining where the neutron decays quickly with a mean lifetime of  $\tau_n \approx 882$  s. The produced pions decay again via

$$\pi^0 \rightarrow 2\gamma \quad (2.28)$$

$$\pi^\pm \rightarrow \mu^\pm + \nu_\mu / \bar{\nu}_\mu \rightarrow e^\pm + \nu_e / \bar{\nu}_e + \nu_\mu + \bar{\nu}_\mu. \quad (2.29)$$

The two photons from neutral pion decay are the origin of high-energy  $\gamma$ -rays from astrophysical objects, e.g. AGN jets and SNRs, and are responsible for Galactic  $\gamma$ -ray emission. Electrons and positrons from charged pion decay are often referred to as secondary electrons which are subject to the same emission processes as primary electrons. Independent of the branching ratios of the decay channels, the total loss rate of CR protons due to hadronic interactions (Mannheim and Schlickeiser, 1994) is

$$\dot{p} = n_p \sigma_{pp}^\pi K_p \frac{\gamma - 1}{\beta} \theta(p - p_{\text{thr}}) \quad (2.30)$$

where  $n_N$  is the target nucleon density,  $\sigma_{pp}^\pi$  is the total pion production cross section (Dermer, 1986), and  $K_p = 0.65$  is the inelasticity (Mannheim and Schlickeiser, 1994).

## 2.2 Magnetohydrodynamical Simulations

Magnetohydrodynamical (MHD) simulations are an essential tool for understanding the physical processes of astrophysical systems. Classically, the plasma is treated as a fluid of an ideal gas. The fluid approximation requires frequent scattering of the particles in the fluid and that the mean free path between collisions  $\lambda_{\text{mfp}} = (\sigma n)^{-1}$ , with collision cross

section  $\sigma$  and number density  $n$ , is much smaller than the macroscopic system length scale. To order of magnitude, the cross section of charged particles is  $\sigma \sim (kT)^2/e^2$  (Shu, 1992) which yields  $\lambda_{\text{mfp}} \approx 10^{-5} \text{ pc } (T/10^4 \text{ K})^2 (n/1 \text{ cm}^{-3})^{-1}$ . The ideal gas assumption is valid due to low number densities and high temperatures in many astrophysical environments, except for the interior of stars or gaseous planets. CRs can be incorporated into MHD simulations treating them as an additional, relativistic fluid if they are efficiently coupled to the plasma via frequent wave-particle scatterings on spatial scales much smaller than the macroscopic system length.

### 2.2.1 Ideal MHD

We present the standard derivations for the equations of ideal MHD (e.g. Shu, 1992; Pringle et al., 2007; Regev et al., 2016). The underlying assumptions are that the plasma is perfectly conducting and behaves like a perfect fluid with the equation of state

$$P_{\text{th}} = (\gamma_{\text{th}} - 1) \varepsilon_{\text{th}} \quad (2.31)$$

that relates thermal pressure  $P_{\text{th}}$  to the thermal energy density  $\varepsilon_{\text{th}}$  via the adiabatic index  $\gamma_{\text{th}} = 5/3$  of ideal gas. The equations derived below rely on the conservation of mass, momentum, and energy.

We consider an arbitrary volume  $V$  in which the gas has a mass density  $\rho$ . The total mass inside the volume is given by the volume integral and it can only change by inflowing or outflowing material through the surface  $\partial V$  of the volume in absence of any sources or sinks

$$\frac{\partial}{\partial t} \int_V \rho \, dV = - \int_{\partial V} \rho \mathbf{v} \cdot d\mathbf{A} \quad (2.32)$$

where  $\mathbf{v}$  is the velocity of the flowing material. The minus sign on the right-hand side is due to the outwards pointing normal vector  $\mathbf{S}$  of a surface element of the volume. We apply Gauss's theorem  $\int_{\partial V} \mathbf{a} \cdot d\mathbf{A} = \int_V \nabla \cdot \mathbf{a} \, dV$  and consider that Equation (2.32) holds for any volume  $V$  such that we obtain the continuity equation

$$\frac{\partial \rho}{\partial t} + \nabla \cdot (\rho \mathbf{v}) = 0. \quad (2.33)$$

The momentum equation is obtained with the same approach. We start with the total momentum  $\int_V \rho \mathbf{v} \, dV$  inside a volume  $V$  that can change via momentum flux through the surface

$$\frac{\partial}{\partial t} \int_V \rho \mathbf{v} \, dV = - \int_{\partial V} \rho \mathbf{v} \mathbf{v}^T \cdot d\mathbf{A}. \quad (2.34)$$

if there are no external forces acting on the fluid (e.g. gravity) and if there is no viscosity. Applying Gauss's theorem we obtain the equation

$$\frac{\partial}{\partial t} (\rho \mathbf{v}) + \nabla \cdot (\rho \mathbf{v} \mathbf{v}^T) = 0 \quad (2.35)$$

which is Newton's second law in absence of exterior forces for a fluid element. We add the gradient force  $\mathbf{F}_P = -\nabla P_{\text{th}}$  with thermal pressure  $P_{\text{th}}$  and the Lorentz force  $\mathbf{F}_L = (\mathbf{j} \times \mathbf{B})/c$  with current density  $\mathbf{j}$  and magnetic field  $\mathbf{B}$  to the right-hand side of the equation above. We neglect the electric field  $\mathbf{E}$  which is zero under the assumption of ideal MHD, i.e. infinite conductivity. The Lorentz force can be rewritten with Ampère's law such that

$$\mathbf{F}_L = (\mathbf{B} \cdot \nabla) \mathbf{B} - \frac{1}{2} \nabla B^2 \quad (2.36)$$

where the first and second term on the right-hand side are the magnetic tension and pressure, respectively. We finally obtain the momentum equation

$$\frac{\partial}{\partial t} (\rho \mathbf{v}) + \nabla \cdot [\rho \mathbf{v} \mathbf{v}^T + P \mathbf{1} - \mathbf{B}(\mathbf{v} \cdot \mathbf{B})] = 0 \quad (2.37)$$

where  $P = P_{\text{th}} + B^2/2$  is the total pressure and  $\mathbf{1}$  is a rank two unit tensor. It is useful to define the plasma beta parameter  $\beta_{\text{pl}} = P_{\text{th}}/P_B$  that is the ratio of plasma thermal pressure to magnetic pressure.

The evolution of the energy density equation can be obtained similarly to the continuity and momentum equation. We first look at the evolution of thermal and kinetic energy density and include the magnetic energy later on. The volume  $V$  contains thermal energy density  $\varepsilon_{\text{th}}$  and kinetic energy density  $\rho v^2/2$  which can change through inflow/outflow of energy and by pressure  $P_{\text{th}}$  acting on the system according to first law of thermodynamics at constant entropy

$$\frac{\partial}{\partial t} \int_V \left( \varepsilon_{\text{th}} + \frac{1}{2} \rho v^2 \right) dV = - \int_{\partial V} \left( \varepsilon_{\text{th}} + \frac{1}{2} \rho v^2 + P_{\text{th}} \right) \mathbf{v} \cdot d\mathbf{A}. \quad (2.38)$$

We note that viscosity, thermal conduction, and non-adiabatic energy gains and losses are neglected. As before, the equation above is converted via Gauss's theorem to

$$\frac{\partial}{\partial t} \left( \varepsilon_{\text{th}} + \frac{1}{2} \rho v^2 \right) + \nabla \cdot \left[ \left( \varepsilon_{\text{th}} + \frac{1}{2} \rho v^2 + P_{\text{th}} \right) \mathbf{v} \right] = 0. \quad (2.39)$$

We add the equation for the evolution of magnetic energy density

$$\frac{\partial}{\partial t} \left( \frac{1}{2} B^2 \right) + \nabla \cdot [\mathbf{B}^2 \mathbf{v} - \mathbf{B}(\mathbf{v} \cdot \mathbf{B})] = 0. \quad (2.40)$$

which is obtained by combining Faraday's law

$$\nabla \times \mathbf{E} + \frac{1}{c} \frac{\partial \mathbf{B}}{\partial t} = 0 \quad (2.41)$$

and ideal Ohm's law

$$\mathbf{E} + \frac{1}{c} (\mathbf{v} \times \mathbf{B}) = 0. \quad (2.42)$$

The energy conservation equation is then given by

$$\frac{\partial \varepsilon}{\partial t} + \nabla \cdot [(\varepsilon + P)\mathbf{v} - \mathbf{B}(\mathbf{v} \cdot \mathbf{B})] = 0. \quad (2.43)$$

where  $\varepsilon = \varepsilon_{\text{th}} + \rho v^2/2 + \mathbf{B}^2$  is the total energy density and  $P = P_{\text{th}} + \mathbf{B}^2/2$  is the total pressure. The equation for the evolution of the magnetic field can be obtained from Faraday's and ideal Ohm's law and is called induction equation

$$\frac{\partial \mathbf{B}}{\partial t} = \nabla \cdot (\mathbf{B}\mathbf{v}^T - \mathbf{v}\mathbf{B}^T). \quad (2.44)$$

Finally, the equations (2.33), (2.36), (2.43), and (2.44) can be combined to the elegant form as hyperbolic conservation law

$$\frac{\partial \mathbf{U}}{\partial t} + \nabla \cdot \mathbf{F}(\mathbf{U}) = \mathbf{S} \quad (2.45)$$

where  $\mathbf{U}$ ,  $\mathbf{F}(\mathbf{U})$ , and  $\mathbf{S}$  denote the state vector of conserved quantities, the flux vector, and the source vector, respectively. In ideal MHD, these vectors are given by

$$\mathbf{U} = \begin{pmatrix} \rho \\ \rho\mathbf{v} \\ \varepsilon \\ \mathbf{B} \end{pmatrix}, \quad \mathbf{F}(\mathbf{U}) = \begin{pmatrix} \rho\mathbf{v} \\ \rho\mathbf{v}\mathbf{v}^T + P\mathbf{1} - \mathbf{B}\mathbf{B}^T \\ (\varepsilon + P)\mathbf{v} - \mathbf{B}(\mathbf{v} \cdot \mathbf{B}) \\ \mathbf{B}\mathbf{v}^T - \mathbf{v}\mathbf{B}^T \end{pmatrix}, \quad \mathbf{S} = \begin{pmatrix} 0 \\ 0 \\ 0 \\ 0 \end{pmatrix}. \quad (2.46)$$

In addition, the source vector  $\mathbf{S}$  that accounts for additional heating and cooling terms for the energy equation can be added to the right-hand side of Equation (2.45). If the magnetic field is zero and viscosity with the viscous stress tensor  $\mathbf{\Pi}$  is included into the momentum and energy equations, the Navier-Stokes equations are obtained.

### 2.2.2 MHD with Cosmic Rays

In contrast to PIC simulations, MHD simulations treat CRs as a relativistic gas with adiabatic index  $\gamma_{\text{cr}} = 4/3$  that interacts with the thermal gas via momentum and energy exchange. This treatment assumes that CRs are spatially confined to the magnetic field which is flux frozen into the plasma due to its high electrical conductivity. It is valid as long as the gyro radius is smaller than the coherence scale of the magnetic field which is a few parsecs in the ISM up to few kiloparsecs in the Milky Way (Beck and Wielebinski, 2013). The bulk of CR energy is carried by CR protons with energies of around the proton rest mass (Enßlin et al., 2007) which corresponds to gyroradii

$$r_g = \frac{E_p}{eB} \approx 10^{-6} \text{ pc} \left( \frac{E_p}{1 \text{ GeV}} \right) \left( \frac{B}{1 \mu\text{G}} \right)^{-1} \quad (2.47)$$

where  $E_p$  is the kinetic energy of an individual proton. Hence, it is a valid assumption to treat CR as relativistic gas within MHD simulations which only breaks down for ultra high energetic CRs. The equations of ideal MHD (2.45) and (2.46) are extended by a CR energy component and a source vector that accounts for energy exchange between thermal and CR fluid via CR pressure (for a treatment without CR streaming see, e.g. Hanasz and Lesch, 2003). In addition, loss (cooling) terms  $\Lambda$  and gain (heating) terms  $\Gamma$  are included for both fluids. The CR energy component is obtained by integrating the transport equation (2.4) according to the kinetic energy moment integral in Equation (2.7). The conservation law of ideal MHD including CRs is given by

$$\frac{\partial \mathbf{U}}{\partial t} + \nabla \cdot \mathbf{F}(\mathbf{U}) = \mathbf{S}. \quad (2.48)$$

The state vector  $\mathbf{U}$ , flux vector  $\mathbf{F}(\mathbf{U})$ , and source vector  $\mathbf{S}$  are given by (Pfrommer et al., 2017a)

$$\mathbf{U} = \begin{pmatrix} \rho \\ \rho \mathbf{v} \\ \varepsilon \\ \varepsilon_{\text{cr}} \\ \mathbf{B} \end{pmatrix}, \quad \mathbf{F}(\mathbf{U}) = \begin{pmatrix} \rho \mathbf{v} \\ \rho \mathbf{v} \mathbf{v}^T + P \mathbf{1} - \mathbf{B} \mathbf{B}^T \\ (\varepsilon + P) \mathbf{v} - \mathbf{B} (\mathbf{v} \cdot \mathbf{B}) \\ \varepsilon_{\text{cr}} \mathbf{v} + (\varepsilon_{\text{cr}} + P_{\text{cr}}) \mathbf{v}_{\text{st}} - \kappa_{\varepsilon} \mathbf{b} (\mathbf{b} \cdot \nabla \varepsilon_{\text{cr}}) \\ \mathbf{B} \mathbf{v}^T - \mathbf{v} \mathbf{B}^T \end{pmatrix},$$

$$\mathbf{S} = \begin{pmatrix} 0 \\ 0 \\ P_{\text{cr}} \nabla \cdot \mathbf{v} - \mathbf{v}_{\text{st}} \cdot \nabla P_{\text{cr}} + \Lambda_{\text{th}} + \Gamma_{\text{th}} \\ -P_{\text{cr}} \nabla \cdot \mathbf{v} + \mathbf{v}_{\text{st}} \cdot \nabla P_{\text{cr}} + \Lambda_{\text{cr}} + \Gamma_{\text{cr}} \\ 0 \end{pmatrix} \quad (2.49)$$

where  $\varepsilon_{\text{cr}}$ ,  $P_{\text{cr}}$ ,  $\mathbf{v}_{\text{st}}$ , and  $\kappa_{\varepsilon}$  are energy density, pressure, streaming velocity, and kinetic energy weighted spatial diffusion coefficient of the CRs, respectively, and  $\mathbf{b} = \mathbf{B}/|\mathbf{B}|$  is the magnetic field unit vector. The total pressure is given by

$$P = P_{\text{th}} + P_{\text{cr}} + \frac{\mathbf{B}^2}{2} \quad (2.50)$$

where  $P_{\text{cr}}$  is the CR pressure. The total energy density excluding CRs is

$$\varepsilon = \varepsilon_{\text{th}} + \frac{\rho \mathbf{v}^2}{2} + \frac{\mathbf{B}^2}{2} \quad (2.51)$$

with the thermal energy density  $\varepsilon_{\text{th}}$ . The system of equations in (2.49) is closed by relating energy density and pressure

$$P_{\text{th}} = (\gamma_{\text{th}} - 1) \varepsilon_{\text{th}}, \quad (2.52)$$

$$P_{\text{cr}} = (\gamma_{\text{cr}} - 1) \varepsilon_{\text{cr}} \quad (2.53)$$

with adiabatic index  $\gamma_{\text{th}} = 5/3$  and  $\gamma_{\text{cr}} = 4/3$  for thermal gas and relativistic cosmic rays, respectively. The streaming velocity of CRs given by

$$\mathbf{v}_{\text{cr}} = -v_{\text{A}} \text{sgn}(\mathbf{B} \cdot \nabla P_{\text{cr}}) \quad (2.54)$$

which implies that CRs stream along the magnetic fields in direction of their negative pressure gradient. Although individual CR particles travel with approximately the speed of light, the bulk motion is limited to the Alfvén velocity due to the CR streaming instability (Kulsrud and Pearce, 1969; Wiener et al., 2013). The streaming of CRs excites Alfvén waves in the magnetic field, that scatter and nearly isotropize the CR distribution in the wave frame. This limits the bulk streaming motion to approximately the Alfvén velocity.

In summary, MHD simulations capture all important transport processes of CRs that are advection with the gas, streaming along magnetic field lines down the CR pressure gradient, spatial diffusion, and cooling. It is important to note that the equations above neglect the momentum spectrum of CRs and use a one-moment formulation of CR transport, i.e. only the CR energy density is evolved. A treatment of spectrally resolved CR hydrodynamics is presented in Girichidis et al. (2020) which enables to correctly connect to CR proton observables that are chemical changes by interaction of low-energy CRs,  $\gamma$ -ray emission and production of secondary electrons by hadronic interactions of high-energy CRs. In order to account for self-regulated CR transport with streaming and diffusion, the formalism needs to be extended to a two-moment formulation of CRs, i.e. the evolution of CR energy density and momentum density, including the energy density of Alfvén waves (Thomas and Pfrommer, 2019). In order to understand the details of microscopic particle acceleration at the shock front, higher-order moments of the transport equation need to be taken into account (e.g. Reville and Bell, 2013).

### 2.2.3 Shocks

Shocks appear in many astrophysical environments and are an important source of CR acceleration. A shock happens if a gas reaches velocities that are larger than the sound speed  $c_s$  of the medium or than the fast magnetosonic waves in high  $\beta_{\text{pl}}$  environments and is characterized by a discontinuous change of fluid properties and an increase of entropy. For simplicity, we ignore magnetic fields and cosmic rays in this discussion and refer for detailed treatment of shocks involving CRs to Pfrommer et al. (2017a). It is useful to discuss the shock properties in the shock rest frame. We denote upstream and downstream quantities with indices 1 and 2, respectively. The conservation laws for mass, momentum, and energy lead to the Rankine-Hugoniot jump conditions

$$\rho_1 v_1 = \rho_2 v_2, \quad (2.55)$$

$$P_1 + \rho_1 v_1^2 = P_2 + \rho_2 v_2^2, \quad (2.56)$$

$$\frac{\varepsilon_1 + P_1}{\rho_1} + \frac{v_1^2}{2} = \frac{\varepsilon_2 + P_2}{\rho_2} + \frac{v_2^2}{2}. \quad (2.57)$$

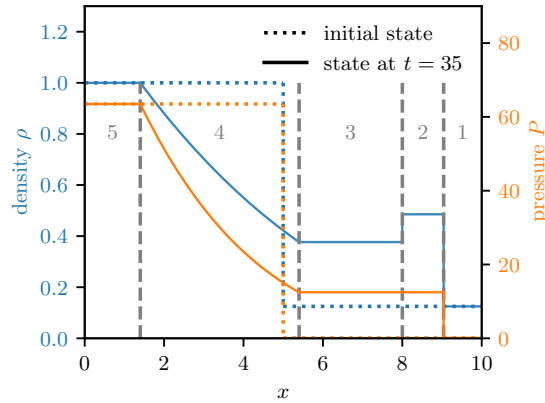


Figure 2.1: Shock tube test for a strong shock with  $\mathcal{M} = 10$ . Initial states of density (orange) and pressure (blue) are shown by the dotted lines and states at time  $t = 35$  by solid lines. Dashed lines separate undisturbed left state (5), rarefaction wave (4), decompressed left fluid (3), shock-compressed right fluid (2), and undisturbed right state (1).

It is important to note that Equation (2.55) allows for two solutions  $v_1 = v_2 = 0$  and  $v_1, v_2 \neq 0$ . The former is called a tangential discontinuity where no mass is flowing through the interface and the latter is a shock. For a polytropic gas, the jump conditions can be expressed by the shock upstream Mach number

$$\mathcal{M} = v_1/c_s = \sqrt{\frac{mv_1^2}{\gamma kT_1}} \quad (2.58)$$

that is the ratio of the shock speed to the upstream sound speed. Hence, the jump conditions can be expressed as functions of the Mach number

$$\frac{\rho_2}{\rho_1} = \frac{v_1}{v_2} = \frac{\gamma + 1}{\gamma - 1 + 2/\mathcal{M}^2}, \quad (2.59)$$

$$\frac{P_2}{P_1} = \frac{2\gamma\mathcal{M}^2 - (\gamma - 1)}{\gamma + 1}, \quad (2.60)$$

$$\frac{T_2}{T_1} = \frac{[(\gamma - 1)\mathcal{M}^2] [2\gamma\mathcal{M}^2 - (\gamma - 1)]}{(\gamma + 1)^2 \mathcal{M}^2}, \quad (2.61)$$

where the latter is a combination of the former two relations. These relations show the discontinuous change of density, pressure, and temperature across the shock. The shock dissipates kinetic energy into heat thereby increasing the specific entropy of the gas by

$$\Delta s = c_V \left[ \ln \left( \frac{P_2}{\rho_2} \right) - \ln \left( \frac{P_1}{\rho_1} \right) \right]. \quad (2.62)$$

Figure 2.1 shows an example of a shock tube test problem for a strong shock with  $\mathcal{M} = 10$ . The dotted lines represent the initial densities  $\rho_5 = 1$  and  $\rho_1 = 0.125$  and initial pressures  $P_5 = 63.5$  and  $P_1 = 0.1$ . The velocities are initially zero. Due to the high pressure on the left-hand side a shock wave propagates into the medium on the right-hand side. The medium has five characteristic regions that are the undisturbed left state (5), the rarefaction wave (4), the expanded left fluid (3), the shock-compressed right fluid / shock piston (2), and the undisturbed right state (1). The shock front is between regions (1) and (2) and is characterized by density and pressure jumps according to Equations (2.59) and (2.60). Regions (2) and (3) are separated by a contact discontinuity which has a jump in density but not in pressure. In a medium additionally containing a relativistic CR fluid, the same description holds for the total pressure. However, thermal and CR pressure behave differently due to different adiabatic indices and additional CR pressure due to CR injection at the shock has to be taken into account (Pfrommer et al., 2017a).

## 2.3 Supernova Remnants

The stellar evolution of white dwarfs which are pushed above the Chandrasekhar mass limit and of massive stars with  $M_* \gtrsim 8M_\odot$  is terminated by a supernova (SN) which is a luminous and powerful explosion (e.g. Alsabti and Murdin, 2017). The name supernova refers to very luminous new star that is only temporally visible. Approximately  $10^{51}$  erg is converted into kinetic energy by release of gravitational binding energy. The explosion drives an expanding shock wave into the ambient medium, thereby heating the gas and accelerating CRs. The expanding shell of the SN is visible via thermal X-rays and non-thermal radio, X-ray, and  $\gamma$ -ray emission. The remnants can be visible from hundreds to a few thousand years. SNe are able to produce isotopes with atomic number  $Z > 28$  by rapid neutron capture during the r-process and can be also detected via neutrino emission (e.g. Hirata et al., 1987).

### 2.3.1 Classification

The classification of SNe is based on spectroscopic properties rather than the physical mechanism leading to the explosion. If a SN shows no hydrogen lines it is referred to as type I and if hydrogen lines are visible then it is of type II.

Type Ia SNe are driven by thermonuclear explosion and show silicon absorption lines but no hydrogen lines. There are two mechanisms that lead to a type Ia SN. In the single degenerate scenario (Nomoto, 1982), a white dwarf accretes mass from a companion star via stellar wind or through Roche-lobe overflow through the inner Lagrangian point of the binary system. The explosion is triggered when the carbon-oxygen white dwarf reaches the Chandrasekhar mass of  $M_{\text{ch}} = 1.4M_\odot$ . However, this model requires a fine-tuned mass flow such that accretion is possible in a stable configuration (Maguire, 2017). In the double degenerate scenario (Iben and Tutukov, 1984), the binary system is composed

of two white dwarfs which merge and explode. The fraction of single versus double degenerate scenarios is a matter of active debate. The current paradigm suggests that double degenerate scenarios are more likely (see Pakmor et al., 2010, for an example of violent mergers).

Type Ib/c and II SNe mark the end of massive stars which undergo a core collapse when the gravity of outer layers exceed the thermal pressure in the nuclear-burning core. The explosion is preceded by stellar winds and significant mass ejection into the surrounding medium.

### 2.3.2 Evolution of Supernova Remnants

The expansion of the supernova remnant (SNR) into the surrounding circum stellar medium (CSM) or ISM has three characteristic stages (e.g. Gaisser et al., 2016; Alsabti and Murdin, 2017; Reynolds, 2017). The explosion energy and the density profiles of the CSM and of the ejected mass determine the duration of these evolutionary stages.

#### Free Expansion Phase

The majority of the explosion energy is converted into the kinetic energy  $E_{\text{ej}}$  of the ejected material which expands into the surrounding medium. The expansion is dominated by the ejecta with mass  $M_{\text{ej}}$  which expands with typical velocities of

$$v_s = \sqrt{\frac{2E_{\text{ej}}}{M_{\text{ej}}}} \approx 10^4 \text{ km s}^{-1} \left( \frac{E_{\text{ej}}}{10^{51} \text{ erg}} \right)^{1/2} \left( \frac{M_{\text{ej}}}{M_{\odot}} \right)^{-1/2} \quad (2.63)$$

that are much larger than the typical speed of sound in the ISM. Hence, the ejecta drive a shock wave with constant velocity as long as the swept up mass is much smaller than the ejected mass. The radius of the shell increases linearly in time. However, the star which ends as a SN can drive stellar winds that change the density profile of the CSM to  $\rho_{\text{CSM}} \propto r^{-s}$  and the ejected mass can have a density profile of  $\rho_{\text{ej}} \propto r^{-n}$  with  $r$  being the radius from the star. The shocked ejecta and the shocked swept up medium are separated by a contact discontinuity which can be described by a self-similar solution (Chevalier, 1982). The radial evolution in time  $t$  of the contact discontinuity is given by

$$r_{\text{cd}} \propto t^{(n-3)/(n-s)}. \quad (2.64)$$

For type Ia SNe, the white dwarf barely changes the surrounding medium. Valid assumptions for the density profiles are  $s = 0$  and  $n = 7$ , such that  $r_{\text{cd}} \propto t^{4/7}$ . In the case of core collapse SNe, the density profiles typically have the parameters  $s = 2$  due to stellar winds which represents the steady state of a wind moving with constant velocity into a sphere and  $n = 9-12$  which gives  $r_{\text{cd}} \propto t^{6/7 \dots 9/10}$  (Reynolds, 2008).

As soon as the swept up mass becomes comparable to the ejected mass the expanding shell is slowed down and moves to the Sedov–Taylor phase. In the model of a homogeneous

surrounding medium and linearly growing radius, the characteristic transition time from free expansion to the Sedov–Taylor phase is

$$t_{\text{st}} = \left( \frac{3M_{\text{ej}}^{5/2}}{4\pi\mu m_{\text{p}}n(2E)^{3/2}} \right)^{1/3} \approx 210 \text{ yr} \left( \frac{M_{\text{ej}}}{M_{\odot}} \right)^{5/6} \left( \frac{E_{\text{ej}}}{10^{51} \text{ erg}} \right)^{-1/2} \left( \frac{\mu n}{1 \text{ cm}^{-3}} \right)^{-1}. \quad (2.65)$$

### Sedov–Taylor Phase

The Sedov–Taylor phase (Sedov, 1959; Taylor, 1950) is characterized by an energy-driven shock wave with

$$r_{\text{st}}(t) = \alpha \left( \frac{Et^2}{\rho} \right)^{1/5}, \quad (2.66)$$

$$v_{\text{st}}(t) = \frac{2\alpha}{5} \left( \frac{E}{\rho t^3} \right)^{1/5}, \quad (2.67)$$

where  $E$  is the total energy of the explosion and  $\alpha$  is dimensionless factor of order unity. The scaling relation in Equation (2.66) can be easily obtained by dimensional analysis and the factor  $\alpha$  can be derived from the Euler equations while exploiting the self-similarity of the solution. The blast wave is slowed down due to the pressure of the ambient medium which leads to a reverse shock. While the forward shock continues expanding with  $r_{\text{st}}(t) \propto t^{2/5}$ , the reverse shock will eventually slow down and move backwards towards the center.

### Radiative Phase

When the temperature of the shocked gas cools down due to the adiabatic expansion in the Sedov–Taylor phase, cooling of the gas via radiation becomes important after approximately  $3 \times 10^4$  yr (Blondin et al., 1998; Reynolds, 2008). The ionized gas starts to recombine and the energy is radiated away via line emission. The remnant consists now of a hot, low density interior surrounded by a thin dense shell. The shell which contains most of the mass moves pressure-driven like a snowplow into the ambient medium with  $r_{\text{pd}} \propto t^{2/7}$ . As soon as the pressure becomes negligible for the dynamics, the shell moves as a momentum-conserving snowplow with  $r_{\text{mc}} \propto t^{1/4}$ . The velocity of the shell decreases further until it becomes slower than the sound speed of the ambient medium and the shock transforms to a normal wave. This marks the end of the remnant.



## 3 The CREST Code

Many MHD codes which include CR protons and ions, e.g. RAMSES (Booth et al., 2013), PIERNIK (Hanasz et al., 2010, 2013) AREPO (Pakmor et al., 2016a; Pfrommer et al., 2017a), FLASH (Girichidis et al., 2016, 2018), treat CR protons as relativistic fluid and thereby evolve only their energy density. A notable exception is the spectrally resolved cosmic ray hydrodynamics in Girichidis et al. (2020). In order to calculate hadronic  $\gamma$ -ray emission, the CR proton spectrum can be calculated with a steady state assumption. The CR proton spectral index depends only on the acceleration as hadronic losses leave it unchanged.

In contrast to CR protons, CR electrons suffer fast cooling losses which change the slope of their spectrum at small and large momenta (e.g. Sarazin, 1999; Winner et al., 2019) and limit the maximum acceleration momentum for shock acceleration (Zirakashvili and Aharonian, 2007). Adiabatic changes further influence the spectrum by shifting the spectrum in momentum space and thereby moving characteristic spectral features of non-adiabatic cooling to different momenta, which limits the applicability of a steady state assumption. As the spectral shape of CR electrons is imprinted into the synchrotron and inverse-Compton spectrum, the evolution of the CR electron spectrum rather than only their energy density has to be followed. Hence, a different simulation approach is required for CR electrons which is obtained with the CREST code. This chapter presents CREST which is a code for Cosmic Ray Electron Spectra evolved in Time.

### 3.1 Implementation Strategy

There are several possibilities to calculate the evolution of the CR electron spectrum along MHD simulations. We discuss these possibilities and present the strategy that is followed by CREST.

First, the spectrum can be calculated on the fly within the MHD simulation or in post-processing due to the fact that the back reaction of CR electrons on the gas is negligible due to their low energy content in comparison to CR protons (e.g. Zweibel, 2013). While the on-the-fly calculation is more efficient in terms of disk usage, post-processing is more flexible and computation-time efficient for model and parameter testing at the cost of disk usage because all necessary information to calculate the spectral evolution has to be stored on disk. The post-processing approach allows to extensively test models of CR electrons without running the same MHD simulation multiple times. We highlight that this is only possible for CR electrons because they do not influence the dynamics of the MHD system. We exploit this possibility in order to test different models of CR electron shock

acceleration, magnetic field amplification, radiation fields, and turbulent reacceleration.

Secondly, the spectrum can be spatially sampled on cells of the MHD simulation or on Lagrangian tracer particles. The first approach avoids spatial coarse graining and guarantees that the spatial sampling of CR electrons matches that of the gas. However, CRs are advected with the gas which flows across the cells such that the spectral information has to be communicated from cells to their neighbours in every MHD time step. Because the spectrum is sampled with many bins, the cell-based spatial sampling requires a high load of additional communication between the cells and eventually across computing threads. The cell-based sampling is not flexible to allow for coarser sampling of CR electrons in less important regions of a simulation, e.g. high density regions with very short electron cooling time scales such that GeV  $\gamma$ -ray emission is mostly due to hadronic interactions of CR protons. An example would be a galaxy simulation with outflows similar to Fermi bubbles in the Milky Way. The GeV  $\gamma$ -ray emission from the disc of the Milky Way can be accounted for hadronic  $\gamma$ -rays and the low density outflow regions are important for leptonic  $\gamma$ -ray emission (Selig et al., 2015). These problems can be overcome with tracer particles that passively follow the gas flow. If the spectrum is evolved on tracer particles, the Fokker–Planck equation can be solved in a Lagrangian frame where no information has to be exchanged among tracer particles if spatial diffusion and streaming can be neglected. They also allow for coarser/finer sampling in certain areas of interest. One disadvantage of tracer particles is that they tend to concentrate more closely than the gas in converging flows as there are no repulsive forces between them (Genel et al., 2013). This issue could be solved by resampling the tracer particles on larger time intervals.

Thirdly, a discretization of the spectrum in momentum has to be chosen. The spectrum can be sampled on piecewise constant bins or with higher order functions such as piecewise power laws (Jun and Jones, 1999; Miniati, 2001; Girichidis et al., 2020). A sampling with piecewise power laws is useful as the CR spectrum has a (piecewise) power-law shape (see Equation 2.15) and allows to calculate the spectral evolution with fewer bins than a sampling with piecewise constant bins would require. However, the reduced number of bins comes at cost of storing two variables per bin which are amplitude and spectral slope. Further, the piecewise power-law approach requires to calculate moments of number and energy density (see Equations 2.6 and 2.7) in every time step in order to calculate shifts across bin boundaries due to cooling and adiabatic changes (see derivations in Miniati, 2001; Girichidis et al., 2020). A sampling of the spectrum with piecewise constant bins allows a straightforward implementation using standard numerical recipes of hydrodynamics such as slope limiters. It is useful to solve the Fokker–Planck equation in 1D momentum space with  $f^{1D} = 4\pi p^2 f^{3D}$  in order to reduce the ratio of the spectrum in each bin, e.g. the accelerated spectrum at strong shocks with a compression ratio of  $r = 4$  follows  $f^{1D} \propto p^{-2}$  in 1D momentum space contrary to  $f^{3D} \propto p^{-4}$  in 3D momentum space. In principle, any scaling  $p^\beta f(p)$  can be chosen but the complexity of the transport equation is retained. The piecewise constant approach requires a larger number of bins which is on the one hand more computationally expensive but on the other hand more robust to numerical instabilities and enables to track small scale spectral features accurately.

Table 3.1: Example of the header file of a tracer particle output.  $N_{\text{tp}}$  is the number of tracer particles. Data is stored in code units.

data type	amount	comment
int32	1	the size of the header block in bytes (without leading/trailing integer)
int32	1	version number of output format
float64	1	the code unit length in cm
float64	1	the code unit mass in g
float64	1	the code unit velocity in cm/s
int32	1	number of tracer particles $N_{\text{tp}}$
int32	1	flag for cosmic ray shock acceleration and 3D magnetic field
int32	1	flag for magnetic obliquity
int32	1	flag for cosmic ray injection
uint32	$N_{\text{tp}}$	IDs of the tracer particle
float32	$N_{\text{tp}}$	associated masses of the tracer particles
int32	1	size in bytes of one output time step for tracer particles
int32	1	the size of the header block in bytes (without leading/trailing integer)

CREST is designed to work as a post-processing code on Lagrangian tracer particle data from the MHD code AREPO. Another advantage of this implementation is that it can work with any MHD code that provides Lagrangian tracer particles. The calculation of the spectrum is done in 1D momentum space and with piecewise constant bins.

## 3.2 MHD Simulations with CR Electrons

We use the massively parallel code AREPO (Springel, 2010) which evolves the equations of ideal MHD (Pakmor and Springel, 2013) on a moving Voronoi mesh with a second-order accurate hydrodynamic scheme (Pakmor et al., 2016c). Shocks are localized on cell-based criteria (Schaal and Springel, 2015) and CR protons are included as an additional relativistic fluid (Pfrommer et al., 2017a). We use the velocity tracer particles which are massless particles and move passively with the gas without affecting its dynamics (Genel et al., 2013). Tracer particles have their own coordinates and velocities which enable them to move independently of the cells.

Although the tracer particles are massless, they represent a finite volume  $V_{\text{tp}}$  of the gas with mass density  $\rho_{\text{gas}}$ . Hence a mass  $m_{\text{tp}}$  can be assigned to the tracer particles such that they represent a volume

$$V_{\text{tp}} = \frac{m_{\text{tp}}}{\rho_{\text{gas}}}. \quad (3.1)$$

Table 3.2: Example of a data block in a tracer particle data file. This block is written to a data file for every tracer particle (output) time step.  $N_{\text{tp}}$  is the number of tracer particles and data is stored in code units.

data type	amount	comment
int32	1	size of the data block in bytes (without leading/trailing integer)
float64	1	current time of the output time step
float32	$N_{\text{tp}}$	$x$ positions
float32	$N_{\text{tp}}$	$y$ positions
float32	$N_{\text{tp}}$	$z$ positions
float32	$N_{\text{tp}}$	mass densities of parent cells $\rho$
float32	$N_{\text{tp}}$	internal energies of parent cells $u_{\text{th}}$
float32	$N_{\text{tp}}$	energy densities of photon fields $\varepsilon_{\text{ph}}$
float32	$N_{\text{tp}}$	$ B $ or $B_x$ with or without CR shock acceleration, respectively
<i>subblock for CR shock acceleration</i>		
float32	$N_{\text{tp}}$	$B_y$
float32	$N_{\text{tp}}$	$B_z$
int32	$N_{\text{tp}}$	shock flags (0 no shock, 1 shock-zone, 2 shock-surface, 3 post-shock)
float32	$N_{\text{tp}}$	shock dissipated thermal energy densities $\varepsilon_{\text{diss}}$
float32	$N_{\text{tp}}$	pre-shock gas densities $\rho_{\text{pre}}$
float32	$N_{\text{tp}}$	post-shock gas densities $\rho_{\text{post}}$
float32	$N_{\text{tp}}$	shock velocities $v_{\text{shock}}$
float32	$N_{\text{tp}}$	shock surface cell crossing times $t_{\text{sc}}$
float32	$N_{\text{tp}}$	$x$ -components of shock normal $n_s$
float32	$N_{\text{tp}}$	$y$ -components of shock normal $n_s$
float32	$N_{\text{tp}}$	$z$ -components of shock normal $n_s$
<i>subblock for magnetic obliquity at CR shock acceleration</i>		
float32	$N_{\text{tp}}$	magnetic obliquity angles $\theta$
<i>subblock for injection at SNR (subresolution treatment)</i>		
float32	$N_{\text{tp}}$	energy densities of injected CR protons at SNRs
int32	1	size of the data block in bytes (without leading/trailing integer)

The velocity of a tracer particle is obtained from the velocity of its parent cell and the linearly interpolated velocity field gradient at its position. Tracer particles are drifted with their velocities on their individual time steps when they are marked as active, i.e. if their parent cells are tagged as active (see Section 7.2 in Springel, 2010).

In order to calculate the evolution of the CR electron spectrum, additional information is required, e.g. the gas density and magnetic field. These quantities are inherited from the parent cells of the tracer particles. The parent cell is obtained by exploiting the convexity of Voronoi cells. It is the cell whose mesh-generating point is closest to the position of the tracer particle. The data of all tracer particles are stored to disk on desired output intervals which are the tracer particle (output) time steps. We note that the most accurate treatment is storing information in each MHD time step as electrons cool quickly and the temporal history of CR electron acceleration and injection is important. However, tracer particle data output is possible on larger time intervals with smaller disk usage at the cost of coarse graining in time. The acceleration of CR electrons at shocks or the injection at SNRs in a subresolution treatment depends on the modeling of CR proton physics in the MHD simulation. This information is either inherited directly from the parent cells or accumulated and stored in separate variables if the tracer particle output takes place on larger time intervals than the MHD time step. The MHD simulation tracks and accumulates the total energy  $E_{\text{CR,tp}}$  which is deposited into the associated volume  $V_{\text{tp}}$  of the tracer particle

$$E_{\text{CR,tp}} = E_{\text{CR,cell}} \frac{V_{\text{tp}}}{V_{\text{cell}}} \quad (3.2)$$

where  $E_{\text{CR,cell}}$  is the energy of accelerated CR protons or injected CR energy at SNRs in a cell and  $V_{\text{cell}}$  is the cell volume at the current MHD time step. For each tracer particle output, we chose to write the density of deposited CR energy  $\varepsilon_{\text{CR,tp}} = E_{\text{CR,tp}}/V_{\text{tp}}$  with the current associated tracer particle volume  $V_{\text{tp}}$  to disk instead of the conserved quantity  $E_{\text{CR,tp}}$  because  $\varepsilon_{\text{CR,tp}}$  is independent of spatial sampling of the tracer particles. Furthermore, we model the injection and acceleration of CR electrons via the source function  $Q(p)$  in Equation (2.5) which is given in units of inverse volume. After writing tracer particle data to disk, the accumulated energy  $E_{\text{CR,tp}}$  is internally reset. We note that if CR energy deposition happens only in a few spatially confined cells, it is necessary to have a sufficient number of tracer particles in those regions, i.e. at least one tracer particle per cell, in order to account for correct energy deposition into CR electrons. In principle, this spatial sampling problem due to low number of tracer particles could be overcome by finding a cloud of neighbouring tracer particles for every cell where CR energy deposition takes place. However, the large shock fronts in our simulations allow for sufficient sampling with our parent-cell approach.

The tracer particle output is stored to disk in a header file with basic information about the simulation and in data files containing a number of tracer particle time steps. An example of the layout of the header file is given in Table 3.1 and an example of the data block for one output step of tracer particle data is given in Table 3.2.

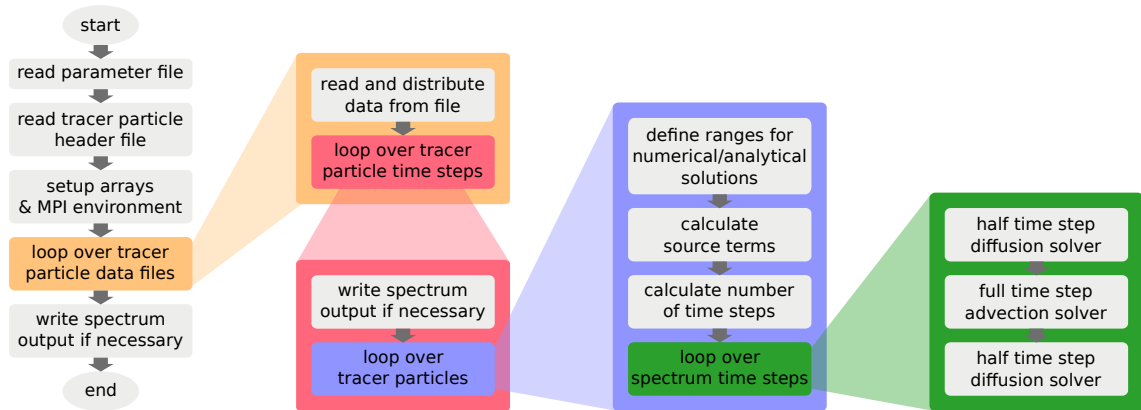


Figure 3.1: CREST flowchart. Coloured boxes represent loops. Tracer particle time steps are defined by the output from the MHD simulation and spectrum time steps are calculated for the numerical solvers. The loop over tracer particles (blue box) is parallelized with MPI.

### 3.3 CREST - Cosmic Ray Electron Spectra Evolution in Time

The CREST code evolves the CR electron spectrum in post-processing based on stored tracer particle data from the MHD simulation. We first present the general structure of the code and continue with the presentation of the numerical implementation of the solvers which are the core of the code.

#### 3.3.1 Structure of the Code

The CREST code can be executed after the MHD simulation has finished and produced tracer particle header and data files. It can be run in parallel with the message passing interface (MPI). Alternatively, a parallelization with the OpenMP (Open Multi-Processing) standard can be used<sup>1</sup>.

The tracer particle files contain all relevant information at time steps that correspond to the MHD time steps or to steps of the desired output time intervals. We refer to these time steps as tracer particle time steps. The data in the tracer particle files is stored in code units of the MHD simulation and is converted to Gaussian-cgs units in the CREST code.

During code execution, outputs of the CR electron spectrum together with additional quantities are written to the disk on intervals which are defined in the parameter file. An example of the structure of these files is given in Table 3.3.

The flowchart of CREST is present in Figure 3.1. At the beginning, the code reads basic information from parameter file and tracer header file and sets up internal data arrays and

<sup>1</sup>The OpenMP parallelization is useful for debugging purposes with one or a few tracer particles.

### 3.3. CREST - COSMIC RAY ELECTRON SPECTRA EVOLUTION IN TIME

Table 3.3: An example of the CREST spectrum output. Data is stored in Gaussian-cgs units.

data type	amount	value & comment
uint32	1	the size of the header block in bytes (without leading/trailing integer)
int32	1	version number of output format
float64	1	time of the current snapshot
int32	1	number of tracer particles $N_{\text{tp}}$
int32	1	number of momentum bins $N_{\text{bin}}$
int32	1	flag for CR shock acceleration ( and 3D $B$ -field)
uint32	1	the size of the header block (without leading/trailing integer)
int32	1	the size of momentum block in bytes (without leading/trailing integer)
float32	$N_{\text{bin}}$	momentum bin centre (normalized momentum)
int32	1	the size of momentum block in bytes (without leading/trailing integer)
uint32	1	the size of data block in bytes (without leading/trailing integer)
uint32	$N_{\text{tp}}$	IDs of tracer particles in CREST
float32	$N_{\text{tp}}$	associated masses of tracer particles
float64	$N_{\text{tp}}$	mass density of parent cell
float64	$N_{\text{tp}}$	internal energy of parent cell
float64	$N_{\text{tp}}$	energy density of photon field
float64	$N_{\text{tp}}$	absolute magnetic field $ B $ or $B_x$
-----		
<i>subblock for 3D magnetic fields (only if CR shock acceleration is active)</i>		
float32	$N_{\text{tp}}$	$B_y$
float32	$N_{\text{tp}}$	$B_z$
-----		
float64	$N_{\text{tp}}$	$x$ position of tracer particle
float64	$N_{\text{tp}}$	$y$ position of tracer particle
float64	$N_{\text{tp}}$	$z$ position of tracer particle
float64	$N_{\text{tp}} \times N_{\text{bin}}$	Spectra for $N_{\text{tp}}$ particles with $N_{\text{bin}}$ bins each
uint32	1	the size of the data block in bytes (without leading/trailing integer)

the environment of the message passing interface (MPI). The first loop over the tracer particle data files (orange box) is executed which contains reading of the data<sup>2</sup>, data distribution routines and another loop. The second loop iterates over the tracer particle time steps of the tracer particle files (red box). It calls the routines to write the electron spectra to files and starts a loop over the tracer particles.

The third loop over tracer particles (blue box) is parallelized with MPI, i.e. each computing thread only calculates the spectra of the tracer particles which it got assigned to at code startup. Within the tracer particle loop, all necessary information to calculate the spectrum is preprocessed. The first routine calculates the ranges where numerical and analytical solutions of the spectrum can be applied based on the current cooling time scales (see Section 4.2.3 for details). After the source terms have been calculated, the number of spectrum time steps are calculated to evolve the spectrum by one tracer particle time step, i.e. within one step in the second loop (red box). The spectrum time steps depend on the time scales of cooling and Fermi-II reacceleration, the speed of adiabatic changes, and the discretization of the momentum space. Finally, a loop over the time steps is executed. The fourth loop (green box) contains the call of the numerical solvers for the diffusion and advection which are parallelized with OpenMP.

### 3.3.2 Numerical Solution to the Fokker–Planck Equation

Here, we present details of our numerical discretisation and how numerical solutions to the Fokker–Planck equation for the evolution of the CR electron spectrum are obtained. The Fokker–Planck equation (2.4) is converted to 1D momentum space via the relation  $f^{1D} = 4\pi p^2 f^{3D}$  such that spectrum evolves without streaming according to

$$\begin{aligned} \frac{df(p,t)}{dt} = & \frac{\partial}{\partial p} \left[ f(p,t) \frac{p}{3} (\nabla \cdot \mathbf{v}) \right] - (\nabla \cdot \mathbf{v}) f(p,t) \\ & - \frac{\partial}{\partial p} [f(p,t) \dot{p}(p,t)] + Q(p,t) \\ & - \frac{\partial}{\partial p} \left[ \frac{f(p,t)}{p^2} \frac{\partial}{\partial p} (p^2 D_{pp}) \right] + \frac{\partial^2}{\partial p^2} [D_{pp} f(p,t)] \\ & + \nabla \cdot [\mathbf{K} \cdot \nabla f(p,t)], \end{aligned} \quad (3.3)$$

where  $df/dt = \partial f/\partial t + \mathbf{v} \cdot \nabla f$  is the Lagrangian time derivative. The last term on the right-hand side represents spatial diffusion which is responsible for Fermi-I acceleration on microscopic scales (see Section 2.1.2) and the Galactic transport of CR electrons. It appears indirectly in our treatment of Fermi-I acceleration via the 1D source term<sup>3</sup>  $Q$  as we focus on macroscopic scales and neglect spatial diffusion.

---

<sup>2</sup>File reading can be splitted into multiple reading routines in order to limit the number of tracer time steps that are stored at once in memory.

<sup>3</sup>The 1D source term is related to the 3D source term in Equation (2.5) via  $Q^{1D} = 4\pi p^2 Q^{3D}$ .

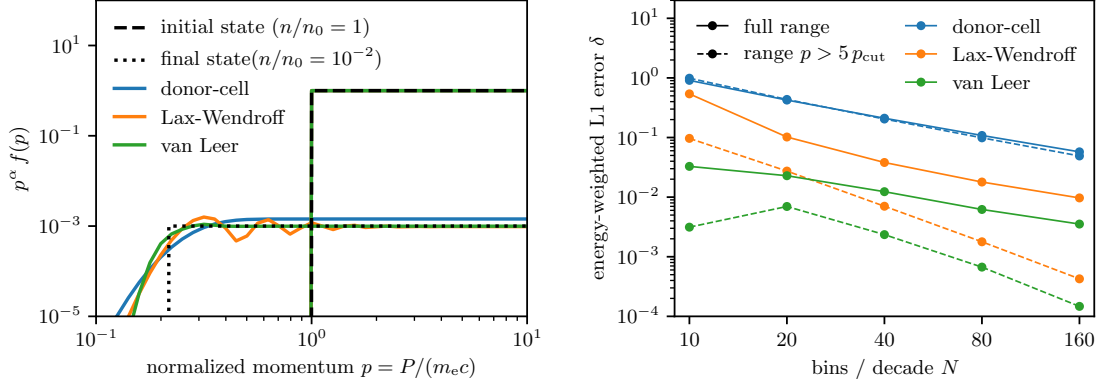


Figure 3.2: Advection test for adiabatic expansion of the density. The left-hand panel shows an initial power-law spectrum (black dashed) with spectral index  $\alpha = 2.5$  that cools due to adiabatic expansion (black dotted). Coloured lines show the solution that is obtained with different numerical advection methods for 20 bins per momentum decade. The right-hand panel shows the energy-weighted L1 error in different momentum ranges for the same methods as shown in the left-hand panel.

We use an operator split approach in order to evolve the CR electron spectrum numerically because the Fokker–Planck Equation (3.3) can be written as an advection-diffusion equation in momentum space. The diffusive (parabolic) part of the transport equation is solved with a finite-difference Crank–Nicolson method (Crank and Nicolson, 1947). The advective (hyperbolic) part of the transport equation is solved with a MUSCL scheme (Monotonic Upstream-centered Scheme for Conservation Laws by van Leer, 1979) together with a van Leer flux limiter (van Leer, 1977) in order prevent oscillations at cutoffs or induced by fast cooling. It is a second-order, finite-volume scheme that uses a piecewise linear reconstruction of the spectrum in each bin. The spectrum is evolved in time from  $t$  to  $t + \Delta t$  according to

$$f(p, t + \Delta t) = \mathcal{A}_{\text{diff}} \left( \frac{\Delta t}{2} \right) \mathcal{A}_{\text{adv}} (\Delta t) \mathcal{A}_{\text{diff}} \left( \frac{\Delta t}{2} \right) f(p, t). \quad (3.4)$$

The numerical implementation of the advection operator  $\mathcal{A}_{\text{adv}}$  and diffusion operator  $\mathcal{A}_{\text{diff}}$  is discussed below. We note that the we closely follow our presentation of those operators in Winner et al. (2019), see also Chapter .

### Comparison of Advective Methods

Figure 3.2 shows results and errors for an advection test for three different numerical advection methods that are the first-order finite-volume donor-cell method, the finite-difference Lax-Wendroff method (Lax and Wendroff, 1960), and a second-order finite-volume method

with the van Leer slope limiter. The left-hand panel shows the theoretical and numerical solutions obtained with the three methods. Initially, the CR electron spectrum in 1D momentum space has the form  $f(p) = Cp^{-\alpha}\Theta(p - p_{\text{cut}})$  with normalization  $C = 1$ , spectral index  $\alpha = 2.5$ , and low momentum cutoff  $p_{\text{cut}} = 1$ . Due to adiabatic expansion of the gas density from an initial density  $n_0$  to a final density of  $n = 10^{-2}n_0$ , the spectrum cools adiabatically. The final spectrum has the form  $f(p) = Cx^{(\alpha+2)/3}p^{-\alpha}\Theta(p - x^{1/3}q)$  with the density ratio  $x = n/n_0$  which can be interpreted as a shift in momentum space and rescaling of the spectrum. The donor-cell method (blue line) is a flux-conserving scheme that is stable but fails to reproduce the analytical solution accurately due to piecewise constant reconstruction of the spectrum within each bin. The Lax-Wendroff method (orange line) is a second-order finite difference method that follows the evolution of the spectrum accurately in absence of sharp features such as cutoffs. However, it produces spurious oscillations at the low momentum cutoff that propagate into the remaining spectrum. Similar problems arise when this method is applied to calculation of the non-thermal cooling of the CR electron spectrum. The piecewise-linear scheme with a non-linear van Leer slope limiter (green line) combines advantages of the two other methods. It uses a piecewise linear reconstruction of the spectrum within each bin and is second-order accurate. In regions close to the cutoff, it falls back to the first-order donor-cell method thereby preventing spurious oscillations. The right-hand panel shows the scaling of the kinetic energy weighted L1 error for all three methods

$$\delta_{\text{L1}} = \frac{\int |f_{\text{sim}} - f_{\text{ana}}| T(p) dp}{\int |f_{\text{ana}}| T(p) dp} \quad (3.5)$$

where  $f_{\text{sim}}$  is the simulated spectrum,  $f_{\text{ana}}$  is the analytical solution, and  $T(p)$  is the kinetic particle energy with  $T(p) = (\sqrt{1 + p^2} - 1)m_e c^2$ . It shows that the van Leer method produces the smallest errors in this test.

Tests on a freely cooling spectrum or combination of non-thermal cooling and continuous injection lead to similar results. The Lax-Wendroff method introduces very strong oscillations due to fast cooling rates at low and high electron momenta, such that it becomes inappropriate to track the evolution of the CR electron spectrum.

### Advection Operator

Our advection operator accounts for cooling (i.e. Coulomb, bremsstrahlung, inverse Compton, and synchrotron cooling), adiabatic changes, and particle acceleration. In our code, we treat Fermi-I acceleration and reacceleration as continuous injection via the term  $Q(p, t)$  in the Fokker-Planck equation as long as the tracer particle resides in shock surface and post-shock cells, i.e. we treat CR electron acceleration identically to the model for CR proton acceleration described by Pfrommer et al. (2017a). The generalized advection

problem obeys the reduced equation

$$\left. \frac{df(p, t)}{dt} \right|_{\text{adv}} - \frac{\partial}{\partial p} \left\{ f(p, t) \left[ \frac{p}{3} (\nabla \cdot \mathbf{v}) - \dot{p}(p, t) \right] \right\} = -(\nabla \cdot \mathbf{v}) f(p, t) + Q(p, t). \quad (3.6)$$

We discretise this equation with a flux-conserving finite volume scheme using a second-order piecewise linear reconstruction of the spectrum (LeVeque et al., 1998). In addition, we use the non-linear van Leer flux limiter (van Leer, 1977) and treat the terms on the right-hand side as an inhomogeneity.

All following equations have in principle to be carried out for all  $N$  momentum bins, i.e.  $i \in [0, N-1]$ . However, the spectrum significantly decreases due to rapid cooling at low and high momenta. We thus cut the spectrum at  $f_{\text{cut}}$  below which we treat numerical values of the spectrum as zero. Hence, the spectrum has to be evolved only on bins between the associated indices  $i_{\text{cut}}$  and  $i_{\text{hcut}}$  indicating the lower and higher cut, respectively. The number of bins on which the spectrum has to be evaluated numerically can be further reduced by using analytic solutions in the low and high momentum regime. The corresponding indices are  $i_{\text{low}}$  and  $i_{\text{high}}$  for the numerical/analytical transition at low and high momentum momenta, respectively. Details are presented below in chapter 4. We define two limiting indices of the advection operator

$$i_{\text{adv}} = \max(i_{\text{cut}}, i_{\text{low}}) \quad \text{and} \quad (3.7)$$

$$i_{\text{hadv}} = \min(i_{\text{hcut}}, i_{\text{high}}) \quad (3.8)$$

for which  $0 \leq i_{\text{adv}}$  and  $i_{\text{hadv}} \leq N$  hold. In the case of a fully numerical simulation, the limiting indices of the advection operator are  $i_{\text{adv}} = i_{\text{cut}}$  and  $i_{\text{hadv}} = i_{\text{hcut}}$ .

Because the total cooling time-scale  $[\dot{p}(p)/p]^{-1}$  is a convex function of momentum, the shortest cooling time-scale is determined by the smallest or largest momentum of the momentum range which is treated by the advection operator. The advection operator works on a time step

$$\Delta t_{\text{adv}} = C_{\text{CFL}} \left[ \max \left( \frac{|\dot{p}(p)|}{\Delta p} \right) + \frac{|\Delta n / \Delta t|}{n} \right]^{-1} \quad (3.9)$$

where  $C_{\text{CFL}}$  is the Courant–Friedrichs–Lewy number and the maximum function over the cooling rates is evaluated on the outermost bin edges

$$\max \left( \frac{|\dot{p}(p)|}{\Delta p} \right) = \max \left( \frac{\dot{p}(p_{i_{\text{adv}}+3/2})}{p_{i_{\text{adv}}+2} - p_{i_{\text{adv}}+1}}, \frac{\dot{p}(p_{i_{\text{hadv}}-5/2})}{p_{i_{\text{hadv}}-1} - p_{i_{\text{hadv}}-2}} \right) \quad (3.10)$$

as the numerical scheme calculates fluxes between bins on bin edges.

The advection operator has a symmetric stencil of five bins which needs in total four ghost bins, with indices  $i_{\text{adv}}$ ,  $i_{\text{adv}}+1$ ,  $i_{\text{hadv}}-2$ , and  $i_{\text{hadv}}-1$ , necessary. The function values in these bins are determined by power-law extrapolation.

The advection operator works as follows. First, we explicitly evolve the spectrum under the influence of (re)acceleration and injection by a half time step

$$f_i^{n+1/2} = f_i^n + \frac{\Delta t}{2} Q_i^n \quad (3.11)$$

where  $Q_i^n = Q(p_i, t_n)$  denotes the discretised (re)acceleration and injection rate at momentum  $p_i$  and time  $t_n$ . We define the advection velocity in momentum space of momentum bin  $p_i$  at time  $t_n$  due to adiabatic and cooling processes by

$$u_i^n = \frac{p_i}{3} (\nabla \cdot \mathbf{v}) - \dot{p}(p_i) \text{ at time } t_n. \quad (3.12)$$

The advection velocity of the bin edges  $u_{i-1/2}$  is similarly defined. We use the advection velocities and the partly evolved function values  $f_i^{n+1/2}$  from equation (3.11) to calculate fluxes  $F$  through the bin edges at intermediate time  $t_{n+1/2}$ . Depending on the sign of the advection velocity  $u_{i-1/2}$  at the bin edge, the flux is given by

$$F_{i-1/2}^{n+1/2} = u_{i-1} f_{i-1}^{n+1/2} + \phi(r_{i-1}) \sigma_{i-1/2} \left( p_{i-1/2} - p_{i-1} + u_{i-1/2} \frac{\Delta t}{2} \right) \quad (3.13)$$

for negative advection velocities  $u_{i-1/2} < 0$  and by

$$F_{i-1/2}^{n+1/2} = u_i f_i^{n+1/2} - \phi(r_i) \sigma_{i-1/2} \left( p_i - p_{i-1/2} - u_{i-1/2} \frac{\Delta t}{2} \right) \quad (3.14)$$

for positive advection velocities  $u_{i-1/2} \geq 0$ . The variable  $\sigma_i$  is the slope of the function values between two bins weighted with their advection velocities

$$\sigma_{i-1/2} = \frac{u_i f_i^{n+1/2} - u_{i-1} f_{i-1}^{n+1/2}}{p_i - p_{i-1}}. \quad (3.15)$$

The function  $\phi(r)$  is the slope limiter function, for which we use the van-Leer slope limiter

$$\phi(r) = \frac{r + |r|}{1 + |r|}. \quad (3.16)$$

The variable  $r$  is ratio of slope at the left bin edge to the slope at the right bin edge, whose definition depends on the sign of the advection velocity. For negative advection velocities  $u_{i-1/2} < 0$ , we use

$$r_{i-1} = \frac{u_{i-1} f_{i-1}^{n+1/2} - u_{i-2} f_{i-2}^{n+1/2}}{p_{i-1} - p_{i-2}} \frac{p_i - p_{i-1}}{u_i f_i^{n+1/2} - u_{i-1} f_{i-1}^{n+1/2}} \quad (3.17)$$

and for positive advection velocities  $u_{i-1/2} \geq 0$ , we adopt

$$r_i = \frac{u_{i+1}f_{i+1}^{n+1/2} - u_i f_i^{n+1/2}}{p_{i-1} - p_{i-2}} \frac{p_i - p_{i-1}}{u_i f_i^{n+1/2} - u_{i-1} f_{i-1}^{n+1/2}}. \quad (3.18)$$

We use the fluxes  $F^{n+1/2}$  at intermediate time step  $t_{n+1/2}$  with the half time step estimate of the spectrum  $f^{n+1/2}$  to calculate the spectrum at time  $t_{n+1}$

$$f_i^{n+1} = f_i^{n+1/2} (1 - \Delta t (\nabla \cdot \mathbf{v})) + \frac{\Delta t}{2} Q_i + \Delta t \frac{F_{i+1/2} - F_{i-1/2}}{p_{i+1/2} - p_{i-1/2}} \left( 1 - \frac{\Delta t}{2} (\nabla \cdot \mathbf{v}) \right), \quad (3.19)$$

where we included an additional factor  $(1 - \Delta t/2 (\nabla \cdot \mathbf{v}))$  that results from the influence of adiabatic changes on the fluxes with a second-order prediction step.

### Diffusion Operator

The diffusion solver is based on the Crank–Nicolson method (Crank and Nicolson, 1947) and solves the diffusive part of the CR electron Fokker–Planck equation,

$$\left. \frac{df(p, t)}{dt} \right|_{\text{diff}} + \frac{\partial}{\partial p} \left[ \frac{f(p, t)}{p^2} \frac{\partial}{\partial p} (p^2 D_{pp}) \right] - \frac{\partial^2}{\partial p^2} [D_{pp} f(p, t)] = 0. \quad (3.20)$$

The combination of an explicit solution

$$f_i^{n+1} = \alpha_i f_{i-1}^n + (1 - \beta_i) f_i^n + \gamma_i f_{i+1}^n \quad (3.21)$$

and an implicit solution

$$f_i^n = -\alpha_i f_{i-1}^{n+1} + (1 + \beta_i) f_i^{n+1} - \gamma_i f_{i+1}^{n+1} \quad (3.22)$$

yields the semi-implicit Crank–Nicolson scheme by addition of both equations

$$-\frac{\alpha_i}{2} f_{i-1}^{n+1} + \left( 1 + \frac{\beta_i}{2} \right) f_i^{n+1} - \frac{\gamma_i}{2} f_{i+1}^{n+1} = \frac{\alpha_i}{2} f_{i-1}^n + \left( 1 - \frac{\beta_i}{2} \right) f_i^n + \frac{\gamma_i}{2} f_{i+1}^n. \quad (3.23)$$

The coefficients  $\alpha_i$ ,  $\beta_i$ , and  $\gamma_i$  are derived by discretising the momentum diffusion term,

$$\begin{aligned} \alpha_i &= \left[ \frac{D_i}{p_{i+1/2} - p_{i-1/2}} + \frac{2D_{i-1}}{p_{i-1}} \right] \frac{\Delta t}{p_i - p_{i-1}}, \\ \beta_i &= \left[ \frac{D_i}{p_i(p_i - p_{i-1})} + \frac{D_{i+1} - D_i}{(p_{i+1} - p_i)^2} + \frac{D_i}{p_{i+1/2} - p_{i-1/2}} \left( \frac{1}{p_{i+1} - p_i} + \frac{1}{p_i - p_{i-1}} \right) \right] \Delta t, \\ \gamma_i &= \left[ \frac{D_i}{(p_{i+1} - p_i)(p_{i+1/2} - p_{i-1/2})} + \frac{D_{i+1} - D_i}{(p_{i+1} - p_i)^2} \right] \Delta t, \end{aligned} \quad (3.24)$$



and its solution is numerically obtained by the application of the forward calculations

$$c'_i = \begin{cases} \frac{c_i}{b_i} & \text{for } i = 0, \\ \frac{c_i}{b_i - a_i c'_{i-1}} & \text{for } i = 1, \dots, N-1, \end{cases} \quad (3.30)$$

$$d'_i = \begin{cases} \frac{d_i}{b_i} & \text{for } i = 0, \\ \frac{d_i - a_i d'_{i-1}}{b_i - a_i c'_{i-1}} & \text{for } i = 1, \dots, N-1, \end{cases} \quad (3.31)$$

and of the backward calculation

$$f_i^{n+1} = \begin{cases} d'_i & \text{for } i = N-1, \\ d'_i - c'_i f_{i+1}^{n+1} & \text{for } i = N-2, \dots, 0. \end{cases} \quad (3.32)$$

We note that the amount of calculations can be reduced if we take only bins into account where the spectrum is larger than a given low cut  $f_{\text{cut}}$ . In this case, equation (3.26) reduces to an  $M$ -dimensional matrix equation with  $M = i_{\text{hcut}} - i_{\text{lcut}}$  and the matrix inversion has to be applied for a submatrix, which is characterised by the indices  $i_{\text{lcut}}, i_{\text{lcut}}+1, i_{\text{lcut}}+2, \dots, i_{\text{hcut}}-2, i_{\text{hcut}}-1$ .



# 4 Evolution of Cosmic Ray Electron Spectra in Magnetohydrodynamical Simulations

This chapter presents our work published in Winner et al. (2019).

Cosmic ray (CR) electrons reveal key insights into the non-thermal physics of the interstellar medium (ISM), galaxies, galaxy clusters, and active galactic nuclei by means of their inverse Compton  $\gamma$ -ray emission and synchrotron emission in magnetic fields. While magnetohydrodynamical (MHD) simulations with CR protons capture their dynamical impact on these systems, only few computational studies include CR electron physics because of the short cooling time-scales and complex hysteresis effects, which require a numerically expensive, high-resolution spectral treatment. Since CR electrons produce important non-thermal observational signatures, such a spectral CR electron treatment is important to link MHD simulations to observations. We present an efficient post-processing code for Cosmic Ray Electron Spectra that are evolved in Time (`CREST`) on Lagrangian tracer particles. The CR electron spectra are very accurately evolved on comparably large MHD time steps owing to an innovative hybrid numerical-analytical scheme. `CREST` is coupled to the cosmological MHD code `AREPO` and treats all important aspects of spectral CR electron evolution such as adiabatic expansion and compression, Coulomb losses, radiative losses in form of inverse Compton, bremsstrahlung and synchrotron processes, diffusive shock acceleration and reacceleration, Fermi-II reacceleration, and secondary electron injection. After showing various code validations of idealized one-zone simulations, we study the coupling of `CREST` to MHD simulations. We demonstrate that the CR electron spectra are efficiently and accurately evolved in shock-tube and Sedov–Taylor blast wave simulations. This opens up the possibility to produce self-consistent synthetic observables of non-thermal emission processes in various astrophysical environments.

## 4.1 Introduction

CRs are ubiquitous in many astrophysical environments, such as the ISM, galaxies, galaxy clusters and active galactic nuclei (AGN). CRs are non-thermal, charged particles consisting of a hadronic component (mainly protons and alpha particles) as well as leptons (mainly electrons and positrons). The leptonic component (henceforth referred to as CR electrons) suffers fast radiative losses via synchrotron interactions with magnetic fields

and inverse Compton (IC) interactions with ambient photon fields. Hence they are directly linked to observations of the non-thermal emission from radio to gamma-ray wavelengths. Hadronic CRs (henceforth referred to as CR protons) are interesting since they play an important dynamical role in the ISM due to their energy equipartition with turbulent and magnetic energy in the midplane of the Milky Way (Boulares and Cox, 1990). As CR protons stream and diffuse vertically from their sources in the galactic midplane, their emerging CR proton pressure gradient can dominate the force balance and accelerate the gas, thus driving a galactic outflow as shown in one-dimensional (1D) magnetic flux-tube models (Breitschwerdt et al., 1991; Zirakashvili et al., 1996; Ptuskin et al., 1997; Everett et al., 2008; Samui et al., 2018) and three-dimensional (3D) simulations (Uhlig et al., 2012; Booth et al., 2013; Salem and Bryan, 2014; Pakmor et al., 2016b; Simpson et al., 2016; Girichidis et al., 2016; Pfrommer et al., 2017b; Ruszkowski et al., 2017b; Jacob et al., 2018).

Fast-streaming CR protons resonantly excite Alfvén waves through the “streaming instability” (Kulsrud and Pearce, 1969). Damping of these waves effectively transfers CR to thermal energy. This process is thought to provide the physical heating mechanism underlying the “cooling flow problem” in galaxy clusters where the cooling gas and nuclear activity appear to be tightly coupled to a self-regulated feedback loop (McNamara and Nulsen, 2007). As CR protons stream out of AGN lobes they can stably heat the surrounding cooling intracluster medium (Loewenstein et al., 1991; Guo and Oh, 2008; Enßlin et al., 2011; Fujita and Ohira, 2012; Pfrommer, 2013; Jacob and Pfrommer, 2017a,b; Ruszkowski et al., 2017a; Ehlert et al., 2018).

Early studies of CR protons in computational cosmology were performed by the Eulerian mesh `COSMOCR` code (Miniati, 2001) and at cosmological shocks by N-body/hydrodynamical simulations (Ryu et al., 2003). The first MHD simulations with active CR proton transport were performed with the `ZEUS-3D` code (Hanasz and Lesch, 2003). Modeling CR proton physics in the smoothed particle hydrodynamics code `GADGET-2` enabled adaptive spatial resolution in high-density environments and to explore the impact of CR protons on the formation of galaxies and galaxy clusters (Pfrommer et al., 2006; Enßlin et al., 2007; Jubelgas et al., 2008). Further numerical CR proton studies were performed with the Eulerian mesh code `PIERNIK` (Hanasz et al., 2010), the adaptive mesh refinement codes `RAMSES` (Booth et al., 2013; Dubois and Commerçon, 2016), `ENZO` (Salem and Bryan, 2014), `FLASH` (Girichidis et al., 2016, 2018), and `PLUTO` (Mignone et al., 2018), the moving-mesh code `AREPO` (Pakmor et al., 2016a; Pfrommer et al., 2017a).

In comparison to CR protons, the energy of CR electrons falls short by a factor of about 100 at the solar radius in the Milky Way (Zweibel, 2013); hence CR electrons are not dynamically important. The cooling time-scale of relativistic CR electrons with Lorentz factors  $\gamma \gtrsim 10^3$  is much shorter than that of relativistic CR protons at the same energy per particle. While CR protons can only effectively cool via rare hadronic interactions (thereby lowering the resulting luminosity), CR electrons cool efficiently via synchrotron and IC interactions. This means that much of the non-thermal physics is only observationally accessible through the leptonic emission channel. Thus, it is very important to model the

momentum spectrum of CR electrons alongside (magneto)hydrodynamical simulations in order to produce realistic synthetic non-thermal observables. Comparing those to observational data enables scrutinising our simulated physics and our understanding of galaxy formation, evolution of galaxy clusters or AGN jet physics.

Supernova remnants (SNRs) provide us with important insights into the physics of particle acceleration and have been observed from radio to  $\gamma$ -ray energies (Helder et al., 2012; Blasi, 2013; Bykov et al., 2018). This radiation is produced by hadronic and leptonic processes, and the ambient density and the magnetic field strength of the SNR determine which of these processes dominates. In low-density environments of SNR, such as RX J1713.7-3946, IC emission by CR electrons likely dominates the  $\gamma$ -ray emission (Ellison et al. 2012, but see Celli et al. 2019, for an interpretation in terms of hadronic emission). Stellar bow shocks of massive runaway stars are also a site of particle acceleration, e.g. the radio emission observed in the bow shock of the runaway star BD +43°3654 might be produced by synchrotron radiation of CR electrons (Benaglia et al., 2010).

Many galaxies exhibit galactic outflows that shine in radio, X-rays, and  $\gamma$ -rays. Understanding the physics of galactic outflows is the holy grail of galaxy formation. The most prominent example of these outflows are the Fermi bubbles, which extend to about 8 kpc north and south from the central region of our Milky Way. They are observed as hard-spectrum gamma-ray structures (Su et al., 2010; Dobler et al., 2010) which coincide with radio lobes (Carretti et al., 2013). The origin of the Fermi bubbles remains elusive and it is not clear whether hadronic CR proton interactions or leptonic IC emission scenarios are dominant for the observed  $\gamma$ -ray emission. Models generally rely on AGN or starburst events. There are several attempts to simulate the evolution of the Fermi bubbles (Yang and Ruszkowski, 2017; Mertsch and Petrosian, 2019) or more generally, to understand radio signatures of outflows in external galaxies (Heesen et al., 2016). However, self-consistent (magneto)hydrodynamical simulations of the Milky Way with CR proton and electron physics are still missing.

Galaxy clusters shine in radio due to synchrotron emission of CR electrons in turbulent cluster magnetic fields. There are three important classes of radio sources in galaxy clusters: radio relics, giant haloes and radio mini haloes (Bykov et al., 2019). Giant radio haloes are characterised by spatially extended regions of diffuse, unpolarised radio emission with an irregular morphology that is centred on the cluster. In contrast, radio relics are often located at the periphery of clusters and show a high degree of polarization with an irregular, elongated morphology. There are several simulation studies of CR electron acceleration and diffuse radio synchrotron emission in the context of galaxy clusters (e.g. Miniati et al., 2001; Miniati, 2003; Pfrommer et al., 2008; Battaglia et al., 2009; Pinzke et al., 2013, 2017; Vazza et al., 2012; Donnert et al., 2013; Donnert and Brunetti, 2014; Guo et al., 2014a,b; Kang et al., 2019).

The plethora of astrophysical systems that shine through leptonic non-thermal radiation makes it inevitable to evolve the CR proton and electron physics on top of MHD simulations in order to distinguish hadronic and leptonic scenarios. Despite the importance of CR electrons, there are only few numerical codes that can evolve the spectra of CR electrons

in MHD simulations, e.g. the `PLUTO` code with CR electrons on Lagrangian particles (Vaidya et al., 2018). We aim at further closing this gap by presenting a numerical post-processing code for Cosmic Ray Electron Spectra that are evolved in Time (`CREST`)<sup>1</sup>, which works together with (magneto)hydrodynamical codes that have Lagrangian tracer particles. In this work, we present the algorithm and test its implementation in one-zone problems. To evolve the CR electron spectrum spatially and temporally resolved alongside MHD simulations, we couple `CREST` to the massively-parallel hydrodynamical code `AREPO` (Springel, 2010), that can also follow CR proton physics (Pfrommer et al., 2017a). In evolving the CR electron spectrum, `CREST` includes adiabatic effects, all important energy loss processes of CR electron as well as energy gain processes such as diffusive shock acceleration (via the Fermi-I process) and reacceleration, Fermi-II reacceleration via particle interactions with compressible turbulence, and secondary electron injection.

We present the physical and numerical foundations of our algorithm in section 4.2. We proceed with numerical tests of our code, including idealized one-zone tests in section 4.3 and simulations with `AREPO` in section 4.4. We conclude in section 4.5 and provide an outlook of future astrophysical applications of our work. We use the cgs system of units throughout this work.

## 4.2 Methodology

Here, we introduce the theoretical background before we explain our discretisation scheme and numerical algorithms to describe our subgrid scale model for Fermi-I acceleration. We then present analytical solutions of limiting cases and our hybrid algorithm that combines analytical and numerical solutions to the transport equation of CR electrons.

### 4.2.1 Theoretical Background

#### Transport Equation

The CR electron distribution is completely described by the phase space density  $f(\mathbf{x}, \mathbf{p}, t)$  whose evolution is given by the relativistic Vlasov equation. Throughout this paper, we use the dimensionless electron momentum,  $\mathbf{p} = \mathbf{P}/(m_e c)$ . CR electrons gyrate around magnetic field lines which are subject to random fluctuations. The application of quasi-linear theory by ensemble averaging over fluctuations, and the use of the diffusion approximation, i.e. the assumption of near-isotropic equilibrium as a consequence of frequent pitch-angle scattering on MHD turbulence leads to the Fokker–Planck equation (Schlickeiser, 1989a; Zank, 2014).

We follow the transport of CR electrons on Lagrangian tracer particles and include continuous losses plus a source term (Schlickeiser, 1989b). Here, we assume that CR

---

<sup>1</sup>The name `CREST` also refers to the physical phenomenon of CR electrons being accelerated and swept up by a shock wave while shining on its crest via synchrotron and IC radiation.

electrons are transported with the gas as they are confined to their gyration orbits around turbulent magnetic fields, which are frozen into the moving plasma. The Fokker–Planck equation for the 1D distribution in momentum space is related to the 3D distribution via  $f(p) = 4\pi p^2 f^{3D}(p)$  and obeys the Fokker–Planck equation without CR streaming (e.g. Pinzke et al., 2017)

$$\begin{aligned} \frac{df(p,t)}{dt} = & \frac{\partial}{\partial p} \left[ f(p,t) \frac{p}{3} (\nabla \cdot \mathbf{v}) \right] - (\nabla \cdot \mathbf{v}) f(p,t) \\ & - \frac{\partial}{\partial p} [f(p,t) \dot{p}(p,t)] + Q(p,t) \\ & - \frac{\partial}{\partial p} \left[ \frac{f(p,t)}{p^2} \frac{\partial}{\partial p} (p^2 D_{pp}) \right] + \frac{\partial^2}{\partial p^2} [D_{pp} f(p,t)] \\ & + \nabla \cdot [\mathbf{K} \cdot \nabla f(p,t)], \end{aligned} \quad (4.1)$$

where  $d/dt = \partial/\partial t + \mathbf{v} \cdot \nabla$  is the Lagrangian time derivative and  $p = |\mathbf{p}|$  is the absolute value of the momentum. The first line on the right-hand side describes adiabatic changes resulting from changes in the gas velocity  $\mathbf{v}$  and Fermi-I acceleration and reacceleration (in combination with spatial diffusion, see Blandford and Eichler, 1987).

The second line describes energy losses (i.e. Coulomb and radiative losses)  $\dot{p}(p,t)$  and injection with source function  $Q(p,t)$  for unresolved subgrid acceleration processes and secondary electron injection that are produced in hadronic interactions of CR protons with the ambient gas. The latter process is described by  $Q_{\text{inj}} = \dot{C}_{\text{inj}} p^{-\alpha_{\text{inj}}}$  with injection slope  $\alpha_{\text{inj}}$  that is identical to that of the CR proton distribution, an injection rate  $\dot{C}_{\text{inj}} = C_{\text{inj}}/\tau_{\text{pp}}$ , where  $C_{\text{inj}} \propto n_{\text{crp}}$  and  $\tau_{\text{pp}} = 1/(c\sigma_{\text{pp}}n_{\text{tar}})$  (Mannheim and Schlickeiser, 1994). Here,  $c$  is the speed of light,  $\sigma_{\text{pp}}$  is the proton-proton cross-section,  $n_{\text{tar}}$  is the target proton density, and  $n_{\text{crp}}$  is the number density of CR protons, which we dynamically evolve with the CR proton module of AREPO (Pfrommer et al., 2017a).

The third line represents the momentum diffusion (Fermi-II reacceleration) with a momentum-dependent diffusion  $D_{pp}(p)$  while the last line describes spatial CR diffusion with the diffusion tensor  $\mathbf{K}$ . Because we do not resolve the necessary scales and plasma processes to directly follow diffusive shock acceleration via the adiabatic and diffusive terms, we have to treat Fermi-I acceleration and reacceleration in form of an analytic subgrid model via the source term  $Q(p,t)$  in our code. We defer the explicit treatment of spatial CR diffusion, as well as CR streaming, to future studies.

### Loss Processes

We note that energy losses are in general time dependent as photon fields, magnetic fields and electron number densities change in time. We will suppress the explicit time dependence in the following formulae for simplicity. Coulomb losses (Gould, 1972a) are

described by

$$\dot{p}_c(p) = -\frac{3\sigma_T n_e c}{2\beta^2} \left[ \ln\left(\frac{m_e c^2 \beta \sqrt{\gamma - 1}}{\hbar \omega_{pl}}\right) + \ln(2) \left(\frac{\beta^2}{2} + \frac{1}{\gamma}\right) + \frac{1}{2} + \left(\frac{\gamma - 1}{4\gamma}\right)^2 \right], \quad (4.2)$$

where  $\sigma_T = 8\pi e^4 (m_e c^2)^{-2}/3$  is the Thomson cross-section,  $\hbar$  is the reduced Planck constant,  $m_e$  the electron mass,  $\beta = p(1 + p^2)^{-1/2}$  is the dimensionless CR electron velocity, and  $\gamma = (1 + p^2)^{1/2}$  is the Lorentz factor of CR electrons. The electron density is  $n_e = n_{\text{gas}} X_H x_e$  where  $X_H$  is the hydrogen mass fraction and  $x_e = n_e/n_H$  is the ionization fraction, the ratio of electron density-to-hydrogen density, which is denoted by  $n_H$ . The plasma frequency is  $\omega_{pl} = \sqrt{4\pi e^2 n_e/m_e}$  and  $e$  denotes the elementary charge.

Charged particles experience synchrotron losses in magnetic fields and experience inverse Compton scattering off of photon fields (Rybicki and Lightman, 1986). Synchrotron losses are given by

$$\dot{p}_s(p) = -\frac{4\sigma_T p^2 B^2}{3m_e c \beta 8\pi}, \quad (4.3)$$

and inverse Compton processes by

$$\dot{p}_{ic}(p) = -\frac{4\sigma_T p^2}{3m_e c \beta} \varepsilon_{\text{ph}}, \quad (4.4)$$

where the total radiation field is a sum over the cosmic microwave background (CMB) radiation and star light,  $\varepsilon_{\text{ph}} = \varepsilon_{\text{star}} + \varepsilon_{\text{cmb}}$ . The momentum loss rate of the bremsstrahlung loss process is given by

$$\dot{p}_b(p) = -\frac{16}{3} \alpha \left(\frac{e^2}{m_e^2 c^3}\right)^2 \gamma \chi [E(p)], \quad (4.5)$$

where  $\alpha$  is the fine-structure constant and the function  $\chi [E(p)]$  is provided by Koch and Motz (1959). The total energy loss rate is given by the sum of all losses:

$$\dot{p}(p, t) = \dot{p}_c(p) + \dot{p}_s(p) + \dot{p}_{ic}(p) + \dot{p}_b(p). \quad (4.6)$$

### Fermi-I Acceleration and Reacceleration

Diffusive shock acceleration also known as Fermi-I acceleration is an important energy gain process for CR electrons. It is a combination of direct acceleration of electrons from the thermal pool and of reacceleration of a fossil electron distribution  $f_{\text{pre}}$  in the pre-shock region, if present.

The total spectrum in the post-shock region is obtained by evaluating adiabatic changes and spatial diffusion of equation (4.1) at the shock. The analytic solution of the total post-shock spectrum is (Bell, 1978b; Drury, 1983; Blandford and Eichler, 1987)

$$f_{\text{post}}(p) = f_{\text{reac}}(p) + f_{\text{acc}}(p), \quad (4.7)$$

where the reaccelerated and accelerated spectrum are

$$f_{\text{reac}}(p) = (\alpha_{\text{acc}} + 2)p^{-\alpha_{\text{acc}}} \int_{p_{\text{inj}}}^p p'^{\alpha_{\text{acc}}-1} f_{\text{pre}}(p') dp' \quad \text{and} \quad (4.8)$$

$$f_{\text{acc}}(p) = C_{\text{acc}} p^{-\alpha_{\text{acc}}} \Theta(p - p_{\text{inj}}), \quad (4.9)$$

respectively, where  $C_{\text{acc}}$  is the normalization and  $p_{\text{inj}}$  is the injection momentum of the accelerated spectrum. The spectral index  $\alpha_{\text{acc}}$  is calculated by

$$\alpha_{\text{acc}} = \frac{r + 2}{r - 1}, \quad (4.10)$$

where  $r = \rho_{\text{post}}/\rho_{\text{pre}}$  denotes the shock compression ratio, i.e. the ratio of post-shock to pre-shock gas density. We also take cooling processes into account, which lead to a modified spectrum with a momentum cutoff (Enßlin et al., 1998; Zirakashvili and Aharonian, 2007; Pinzke and Pfrommer, 2010) of the form

$$\tilde{f}_{\text{post}}(p) = f_{\text{post}}(p) \left[ 1 + a \left( \frac{p}{p_{\text{acc}}} \right)^b \right]^c \exp \left[ - \left( \frac{p}{p_{\text{acc}}} \right)^2 \right], \quad (4.11)$$

where we adopt the parameters  $a = 0.66$ ,  $b = 2.5$ , and  $c = 1.8$  and  $p_{\text{acc}}$  is the cutoff momentum of the (re)accelerated spectrum

$$p_{\text{acc}} = \frac{v_{\text{post}}}{c} \sqrt{\frac{3e(r-1)}{4\sigma_{\text{T}}}} \times \left[ \frac{B_{\text{pre}}^2/(8\pi) + \varepsilon_{\text{ph}}}{rB_{\text{pre}}} + \frac{B_{\text{post}}^2/(8\pi) + \varepsilon_{\text{ph}}}{B_{\text{post}}} \right]^{-1/2}, \quad (4.12)$$

where  $v_{\text{post}}$  is the post-shock velocity in the shock rest frame and  $B_{\text{pre}}$  and  $B_{\text{post}}$  are the pre- and post-shock magnetic fields. Here, we assume a parallel shock geometry so that the magnetic field strength is constant across the shock. We postpone a modelling of the dependencies of the maximum electron energy on magnetic obliquity and amplified magnetic fields via plasma effects such as the non-resonant hybrid instability driven by the CR proton current propagating upstream of the shock (Bell, 2004).

### Fermi-II Reacceleration

Stochastic acceleration, originally proposed by Fermi (1949), describes the energy gains of CRs through random collisions with plasma waves and turbulence. As the gain per collision process is of second order in the velocity ratio of collision counterpart to particle, it is also referred to as Fermi-II reacceleration (Petrosian, 2012). However, Coulomb cooling is too fast for stochastic acceleration from the thermal pool to be efficient in cluster and galactic environments (Petrosian, 2001). Therefore, the Fermi-II process is only efficient in reaccelerating a fossil non-thermal electron distribution.

Fermi-II reacceleration by turbulent magnetic fields was investigated in galaxy clusters as primary energy source for diffusive radio emission from CR electrons in the Coma

cluster (Jaffe, 1977; Schlickeiser et al., 1987). There are different energy transfer channels of turbulent energy injection into CR, e.g. via magnetosonic waves (Ptuskin, 1988) or via transit time damping (TTD) of compressible fast magnetosonic modes (Brunetti and Lazarian, 2007, 2011).

CRs gain energy in turbulent reacceleration through transit time damping. The momentum diffusion in equation (4.1) is given by

$$D_{pp} = D_0 p^2 \quad (4.13)$$

where the physics of turbulent reacceleration is encapsulated in the constant  $D_0$  (Pinzke et al., 2017). The momentum diffusion time is  $\tau_{pp} = p^2/(4D_{pp})$  which is  $\tau_{pp} = 1/(4D_0)$  according to equation (4.13).

## 4.2.2 Numerical Discretisation

### General Setup

In order to solve equation (4.1) numerically, we apply three discretisations to the CR electron phase space density  $f = f(\mathbf{x}, p, t)$ . (i) We discretise  $f$  in configuration space with Lagrangian tracer particles, (ii) we discretise the momentum spectrum of every tracer particle with piecewise constant values per momentum bin, and (iii)  $f$  is discretised in time. The momentum grid is equally spaced in logarithmic space and we use  $N$  bins between the lowest momentum  $p_{\min}$  and highest momentum  $p_{\max}$ . The bin centres are located at

$$p_i = p_{\min} \exp\left[\left(i + \frac{1}{2}\right) \Delta \ln p\right] \quad \text{for } i = 0, 1, \dots, N-1, \quad (4.14)$$

and the bin edges are given by

$$p_{i-\frac{1}{2}} = p_{\min} \exp(i \Delta \ln p) \quad \text{for } i = 0, 1, \dots, N, \quad (4.15)$$

where  $\Delta \ln p = \ln(p_{\max}/p_{\min})/N$  is the grid spacing. The spectrum is defined on all bin centers and is evolved in time from  $t$  by a time step  $\Delta t$  with an operator split approach,

$$f(\mathbf{x}, p, t + \Delta t) = \mathcal{A}_{\text{diff}}\left(\frac{\Delta t}{2}\right) \mathcal{A}_{\text{adv}}(\Delta t) \mathcal{A}_{\text{diff}}\left(\frac{\Delta t}{2}\right) f(\mathbf{x}, p, t). \quad (4.16)$$

Adiabatic changes, Fermi-I (re)acceleration, cooling, and injection are calculated with an advection operator  $\mathcal{A}_{\text{adv}}$  and diffusion in momentum space is calculated with a diffusion operator  $\mathcal{A}_{\text{diff}}$  that both advance the solution for the time step of their arguments.

The advection operator is based on a flux-conserving finite volume scheme with a second-order piecewise linear reconstruction of the spectrum. The terms  $\partial/\partial p \{f(p)[p(\nabla \cdot \mathbf{v})/3 - \dot{p}]\}$ , which include cooling and partially adiabatic changes, are

interpreted as advection in momentum space in order to calculate fluxes across the bin edges given in equation (4.15). In addition, we use the non-linear van Leer flux limiter (van Leer, 1977). The remaining terms for injection, Fermi-I (re)acceleration and adiabatic changes, are treated as an inhomogeneity of the partial differential equation (for details, see appendix 3.3.2). Our implementation is second-order accurate in time and momentum space.

The diffusion operator is based on a finite difference scheme with a semi-implicit Crank–Nicolson algorithm, which is accurate to second order in time and to first order in momentum space (for details, see appendix 3.3.2).

### Time Steps and Characteristic Momenta

The overall time step  $\Delta t$  in equation (4.16) is determined by

$$\Delta t = \min(\Delta t_{\text{adv}}, \Delta t_{\text{diff}}), \quad (4.17)$$

the minimum of the time step for advection and diffusion,

$$\Delta t_{\text{adv}} = C_{\text{CFL}} \left[ \max \left( \frac{|\dot{p}(p)|}{\Delta p} \right) + \frac{|\Delta n / \Delta t|}{n} \right]^{-1} \quad \text{and} \quad (4.18)$$

$$\Delta t_{\text{diff}} = C_{\text{CFL}} \left[ \max \left( \frac{D_{pp}(p)}{p^2} \right) \right]^{-1}, \quad (4.19)$$

respectively, where  $\Delta n / \Delta t$  is the density change of the background gas and the parameter  $C_{\text{CFL}}$  is the Courant–Friedrichs–Lewy number for which we use  $C_{\text{CFL}} = 0.7$  in our simulations. In principle, the maxima in equations (4.18) and (4.19) have to be evaluated for all momentum bins, i.e. for  $i \in [0, N-1]$ . However, in the absence of Fermi-I (re)acceleration, the momentum range of the advection and diffusion operator decreases due to rapidly cooling of the spectrum at low and high momenta. We therefore cut the spectrum at  $f_{\text{cut}}$  below which we treat numerical values of the spectrum as zero. Hence, there is a low- and a high-momentum cutoff

$$p_{\text{lcutoff}} = \min(\{p : f(p) \geq f_{\text{cut}}\}) \quad \text{and} \quad (4.20)$$

$$p_{\text{hcutoff}} = \max(\{p : f(p) \geq f_{\text{cut}}\}), \quad (4.21)$$

respectively, and the related indices of the momentum bins

$$i_{\text{lcutoff}} = \max[0, \min(\{i : p_i < p_{\text{lcutoff}}\}) - 2] \quad \text{and} \quad (4.22)$$

$$i_{\text{hcutoff}} = \min[N, \max(\{i : p_i > p_{\text{lcutoff}}\}) + 3] \quad (4.23)$$

in between which the maxima in equations (4.18) and (4.19) have to be evaluated, i.e. for  $i \in [i_{\text{lcutoff}}, i_{\text{hcutoff}}-1]$ . We consider two extra bins in equations (4.22) and (4.23) due to the ghost cells of the advection operator. The cutoff momenta and the related indices are calculated after every time step.

For clarity, we provide a synopsis of all important momenta and related bin indices:

- $p_{\min}$  and  $p_{\max}$  are the minimum and maximum momenta of our momentum grid, respectively. The corresponding indices are  $i_{\min} = 0$  and  $i_{\max} = N-1$ .
- $p_{\text{lcut}}$  ( $p_{\text{hcut}}$ ) describes the momentum below (above) which the spectrum is treated as zero. The corresponding indices  $i_{\text{lcut}}$  and  $i_{\text{hcut}}$  account for the ghost cells of the advection operator and are given in equations (4.22) and (4.23).
- $p_{\text{low}}$  and  $p_{\text{high}}$  denote the transition momenta between the numerical and the analytical solution for the low- and high-momentum regime, respectively. The definition is given in section 4.2.3.
- $p_{\text{cool}}$  is the momentum related to inverse Compton and synchrotron cooling in the analytical solution. In the case of freely cooling it coincides with the high-momentum cooling cutoff. In the case of Fermi-I (re)acceleration and injection it is the transition momentum from a source dominated to a steady-state spectrum (see section 4.2.3).
- $p_{\text{acc}}$  is the maximum momentum of Fermi-I (re)acceleration where spatial diffusion and cooling balance each other.
- $p_{\text{inj}}$  is the injection momentum of Fermi-I (re)acceleration where the non-thermal spectrum is transitions to the non-thermal spectrum.

### Modelling Fermi-I (Re)Acceleration

We develop an algorithm to account for the Fermi-I process on our tracer particles and aim at reconstructing the discontinuous Rankine–Hugoniot jump conditions on the Lagrangian particle trajectories with the aid of a shock finder in a hydrodynamical scheme. To this end, we use the adaptive moving-mesh code AREPO (Springel, 2010) with CR protons (Pfrommer et al., 2017a) and employ the shock finder by Schaal and Springel (2015), which detects cells in the pre-shock region, the shock surface, and the post-shock zone. The shock direction is determined by the normalized negative gradient

$$\mathbf{n}_s = -\frac{\nabla \tilde{T}}{|\nabla \tilde{T}|} \quad (4.24)$$

of the pseudo temperature which is given by

$$k\tilde{T} = \frac{\mu m_p (P_{\text{th}} + P_{\text{crp}})}{\rho}, \quad (4.25)$$

where  $\mu$  is the mean molecular weight,  $m_p$  is the proton mass,  $\rho$  is the gas mass density, and  $P_{\text{th}}$  and  $P_{\text{crp}}$  denote the thermal and CR proton pressure, respectively. Cells of the *shock zone* are identified by (i) converging flows, i.e. they have a negative velocity divergence, while (ii) spurious shocks are filtered out and (iii) the algorithm applies a safeguard in

the form of a lower limit to the temperature and density jump (from pre- to post-shock quantities) to prevent false-positive detections of numerical noise. The *shock surface* cell is identified with the cell in the shock zone that shows a maximally converging flow along the shock direction. Pre- and post-shock quantities are obtained from the first cells outside the shock zone in the direction of shock propagation and opposite to it, respectively. The algorithm determines the Mach number  $\mathcal{M}$  by the pressure jump and calculates a fraction  $\zeta_e(\theta)$  of the shock-dissipated energy  $E_{\text{diss}}$  that is converted into the acceleration of CR electrons,

$$\Delta E_{\text{cre}} = \zeta_e(\theta) E_{\text{diss}}. \quad (4.26)$$

Here,  $\theta$  is the upstream magnetic obliquity, which is the angle between the direction of shock propagation and the magnetic field. In this paper, we assume an acceleration efficiency of  $\zeta_e = 10^{-3}$ . This corresponds to a ratio of accelerated CR electron to proton energies of  $\Delta E_{\text{cre}}/\Delta E_{\text{crp}} = 10^{-2}$  for efficient CR proton acceleration (Pfrommer et al., 2017a). We defer a discussion of the obliquity dependent acceleration of CR electrons to future studies. We point out that our description is flexible and can be easily adapted to include new particle-in-cell simulation results on the shock acceleration of CR electrons (e.g. Guo et al., 2014a,b; Park et al., 2015).

As soon as the tracer particle reaches a shock zone cell, we keep the background density fixed in order to prevent adiabatic heating before encountering the shock. When the tracer particle transitions from the shock zone to the shock surface cell, we first calculate the reaccelerated spectrum if there is any fossil spectrum and secondly, the directly accelerated spectrum.<sup>2</sup> The ambient density of the tracer particles is then set to the post-shock gas density. In order to model reacceleration and direct acceleration, we assume continuous injection as a subgrid model and adopt the source functions<sup>3</sup>

$$Q_{\text{reac}}(p) = \frac{f_{\text{reac}}(p)}{\Delta t} \text{ and} \quad (4.27)$$

$$Q_{\text{acc}}(p) = \frac{C_{\text{acc}}}{\Delta t} p^{-\alpha_{\text{acc}}} \Theta(p - p_{\text{inj}}), \quad (4.28)$$

where  $\Delta t$  is the the time difference between two MHD time steps.

As described above, the efficiency of direct Fermi-I acceleration depends on the total dissipated energy at the shock, which is numerically broadened to a few cells in finite-volume codes such as AREPO. By contrast, Fermi-I reacceleration only depends on the amplitude of the fossil electron distribution in the pre-shock region (see equation 4.8), which is known at the shock surface cell. In both cases, the slope is solely determined by the Mach number.

<sup>2</sup>We store only one spectrum in memory per tracer particle. Therefore, we first need to evaluate the integral in equation (4.8) before computing the primary electron spectrum due to diffusive shock acceleration.

<sup>3</sup>We use the terminology *acceleration* to describe the production of CR electrons via diffusive shock acceleration and *injection* to describe the generation of secondaries through hadronic interactions.

To model direct acceleration, we calculate and apply the source function for acceleration of equation (4.28) for every time step during which the tracer particle resides in a shock surface or in the post-shock cells for the numerical reasons given above. By contract, the source function for reacceleration (equation 4.27) is only applied during one MHD time step after the tracer particle has encountered the shock surface cell.

We calculate  $\alpha_{\text{acc}}$  from the density jump at the shock,  $r = \rho_{\text{post}}/\rho_{\text{pre}}$ , where the pre-shock density communicated to the shock cell via the AREPO shock finder, and the post-shock density is obtained via

$$\rho_{\text{post}} = \rho_{\text{pre}} \frac{(\gamma_{\text{eff}} + 1)\mathcal{M}^2}{(\gamma_{\text{eff}} - 1)\mathcal{M}^2 + 2}, \quad (4.29)$$

where the effective adiabatic index is given by

$$\gamma_{\text{eff}} = \frac{\gamma_{\text{crp}}P_{\text{crp}} + \gamma_{\text{th}}P_{\text{th}}}{P_{\text{crp}} + P_{\text{th}}} \quad (4.30)$$

with  $\gamma_{\text{th}} = 5/3$  for gas and  $\gamma_{\text{crp}} = 4/3$  for CR protons.

In order to determine the energy of the freshly accelerated CR electrons, we demand its energy density to be a fixed fraction of the freshly accelerated CR proton energy density at the shock. In practice, we attach the accelerated spectrum to the thermal Maxwellian,

$$f_{\text{th}}(p) = 4\pi n_{\text{e,th}} \left( \frac{m_e c^2}{2\pi k_B T} \right)^{3/2} p^2 \exp\left(-\frac{m_e c^2 p^2}{2k_B T}\right) \quad (4.31)$$

at the injection momentum  $p_{\text{inj}}$  which determines the normalization

$$C_{\text{acc}} = f_{\text{th}}(p_{\text{inj}}) p_{\text{inj}}^{\alpha_{\text{acc}}}. \quad (4.32)$$

We use this normalization and the energy of accelerated CR electrons  $\Delta E_{\text{cre}}$ , see equation (4.26), to determine the injection momentum by the condition

$$\int_0^\infty f_{\text{th}}(p_{\text{inj}}) p_{\text{inj}}^{\alpha_{\text{acc}}} p^{-\alpha_{\text{acc}}} \Theta(p - p_{\text{inj}}) E_{\text{e,kin}}(p) dp = \frac{\Delta E_{\text{cre}}}{V_{\text{cell}}}, \quad (4.33)$$

where  $E_{\text{e,kin}}(p) = \left[ \sqrt{1 + p^2} - 1 \right] m_e c^2$  is the kinetic energy and  $V_{\text{cell}}$  is the volume of the AREPO cell, in which the particle resides.

### 4.2.3 Analytical Solutions

The time-scale of all electron cooling processes decreases for low and for high momenta as can be seen in Figure 4.1, where we show the cooling times as a function of momentum. Hence, for very low momenta and very high the cooling time-scales become smaller than the typical time step of an MHD simulation. In order to have an efficient calculation of the CR electron spectrum, which advances on time steps similar to the MHD time step, we use analytical solutions for low and high momenta together with the fully numerical treatment for intermediate momenta. We call the combination of both treatments *semi-analytical solution*.

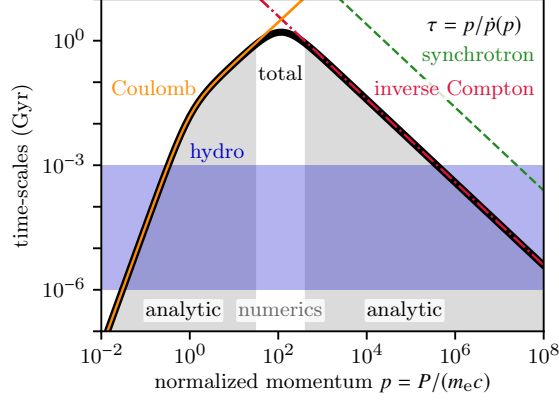


Figure 4.1: Characteristic time-scales for electron cooling ( $n_{\text{gas}} = 10^{-3} \text{ cm}^{-3}$ ,  $B = 5 \mu\text{G}$ ,  $\varepsilon_{\text{ph}} = 6\varepsilon_{\text{cmb}}$ ,  $z = 0$ ) and typical hydrodynamical time steps adopted in simulations of the ISM and galaxy formation (blue band). The grey area shows the ranges where either Coulomb or inverse Compton plus synchrotron cooling dominate and where analytical solutions can be used. Transition momenta of numerical and analytical solutions are  $p_{\text{low}} = 3 \times 10^1$  and  $p_{\text{high}} = 4 \times 10^2$ .

### General Solutions

We follow the derivations described by Sarazin (1999) which we summarise here. The starting point for the analytical solution of the cooling term in equation (4.1) is the momentum loss of an individual electron. Its momentum is shifted from the initial momentum  $p_{\text{ini}}$  to the momentum  $p$  during a time interval of  $\Delta t$

$$\int_{p_{\text{ini}}}^p \frac{1}{\dot{p}(p')} dp' = \Delta t. \quad (4.34)$$

Equation (4.34) is solved for the initial momentum  $p_{\text{ini}}(p, \Delta t)$ , which is used in the analytical solution of the cooled spectrum

$$f(p, t_0 + \Delta t) = f(p_{\text{ini}}(p, \Delta t), t_0) \frac{\dot{p}(p_{\text{ini}}(p, \Delta t), t_0 + \Delta t)}{\dot{p}(p, t_0)}. \quad (4.35)$$

The cooled spectrum can be interpreted as a momentum shift of the initial spectrum at time  $t_0$  multiplied with a momentum-dependent cooling factor. If there is no initial spectrum at  $t_0$  and if the source function  $Q(p, t)$  is constant and continuous in time, the spectrum after time  $t$  is self-similar:

$$f_{\text{self}}(p, t) = f_{\text{steady}}(p) - f_{\text{steady}}(p_{\text{ini}}(p, t)) \frac{\dot{p}(p_{\text{ini}}(p, t))}{\dot{p}(p)}, \quad (4.36)$$

where we use the steady-state solution

$$f_{\text{steady}}(p) = \frac{1}{|\dot{p}(p)|} \int_p^\infty Q(p) dp. \quad (4.37)$$

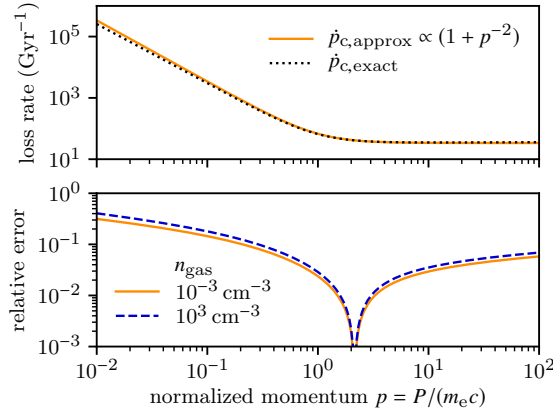


Figure 4.2: Comparison between exact and approximate formulae for Coulomb losses (equations (4.2) and (4.38)). The top panel shows the loss rates for a gas of density  $1 \times 10^{-3} \text{ cm}^{-3}$  and the bottom panel shows the relative error of the approximate formula for two different gas densities.

This means that the self-similar solution is derived by subtracting the cooled steady-state solution from the original steady-state solution. The self-similar spectrum consists of three characteristic momentum ranges, i.e. low, intermediate, and high momenta. For low and high momenta, where the cooling times are smaller than the current time step, the spectrum is already in steady state. In the intermediate momentum range, the spectrum is dominated by the source spectrum as we show later.

The analytical solutions of the cooled spectrum in equation (4.35) and of the self-similar spectrum in equation (4.36) need a functional representation of the spectrum at time  $t_0$  for the entire momentum range. As the spectrum is calculated on a discrete momentum grid with piecewise constant values, we calculate an interpolation function at every time with the Steffen's method (Steffen, 1990), which is cubic and monotonic between neighbouring discrete momenta. This interpolation function is used to calculate the analytic solution after a time step  $\Delta t$ .

In the following, we present the analytical solutions for both low and high momenta. We use a source function  $Q(p) = \dot{C}_{\text{acc}} p^{-\alpha_{\text{acc}}}$  for the self-similar solution of acceleration and cooling. We note that we have  $\dot{C}_{\text{acc}} = C_{\text{acc}}/\Delta t$  for our discretisation and that a source function for injection by hadronic processes with  $Q(p) = \dot{C}_{\text{inj}} p^{-\alpha_{\text{inj}}}$  gives similar results for the self-similar solution. Note that the self-similar solution is not used in our code (see also section 4.2.3) but in order to compare simulation results to their analytic solutions.

### Solution for Low Momenta

Coulomb losses are dominating at small momenta. The analytical solution requires calculating the integral in equation (4.34) and solving for the initial momentum  $p_{\text{ini}}(p, \Delta t)$ . In general, this cannot be done in closed analytic form for the exact Coulomb loss rate

given in equation (4.2). We therefore use an approximation (Pinzke et al., 2013)

$$\dot{p}_c(p) = b_c \left(1 + p^{-2}\right) \text{ with } b_c = \frac{-3\sigma_T n_e c}{2} \ln\left(\frac{m_e c^2}{\hbar\omega_{pl}}\right), \quad (4.38)$$

which is accurate to  $< 30\%$  for momenta  $10^{-2} \leq p \leq 10^2$  as can be seen in Figure 4.2. The integral for the momentum shift in equation (4.34) evaluated with the approximate form of the Coulomb loss rate is

$$\int \frac{1}{\dot{p}_c(p)} dp = \frac{1}{-b_c} [p - \arctan(p)] \approx \frac{1}{-b_c} \left(\frac{p^3}{3 + p^2}\right), \quad (4.39)$$

where we used a Padé approximation (Brezinski, 1996) in the last step. The momentum shift due to Coulomb cooling is then given by

$$p_{ini}(p, \Delta t) = \frac{1}{3} \left[ a + \left( a^3 + \frac{9}{2} \sqrt{4a^4 + 81a^2} + \frac{81a}{2} \right)^{1/3} + a^2 \left( a^3 + \frac{9}{2} \sqrt{4a^4 + 81a^2} + \frac{81a}{2} \right)^{-1/3} \right], \quad (4.40)$$

with  $a = p^3 / (3 + p^2) - b_c \Delta t$ . The analytical solution for the cooled spectrum (see equation (4.35)) is given by

$$f(p, \Delta t) = f[p_{ini}(p, \Delta t), 0] \frac{1 + [p_{ini}(p, \Delta t)]^{-2}}{1 + p^{-2}}. \quad (4.41)$$

The self-similar spectrum is given by

$$f_{self}(p, \Delta t) = \frac{\dot{C}_{acc}}{(1 - \alpha_{acc})} \left\{ \frac{p^{-\alpha_{acc}+1}}{\dot{p}_c(p)} - \frac{[p_{ini}(p, \Delta t)]^{-\alpha_{acc}+1}}{\dot{p}_c[p_{ini}(p, \Delta t)]} \frac{1 + [p_{ini}(p, \Delta t)]^{-2}}{1 + p^{-2}} \right\} \quad (4.42)$$

where we use the exact Coulomb loss rate for the first term in the bracket in order to satisfy  $f_{self} \rightarrow f_{steady}$  for  $\Delta t \rightarrow \infty$ .

### Solution for High Momenta

For large momenta, inverse Compton and synchrotron cooling are dominating and both loss rates have the same momentum scaling. We define for convenience the sum of both as

$$\dot{p}_{ic+s}(p) = \dot{p}_{ic}(p) + \dot{p}_s(p) = p^2 b_{ic+s} \quad (4.43)$$

where  $b_{\text{ic+s}} = -4\sigma_{\text{T}} (B^2/8\pi + \varepsilon_{\text{ph}}) / (3m_e c \beta)$  denotes the momentum independent factor of both loss rates. The momentum shift during a time interval  $\Delta t$  according to equation (4.34) is

$$p_{\text{ini}}(p, \Delta t) = \frac{p}{1 - p/p_{\text{cool}}(\Delta t)} \quad (4.44)$$

where  $p_{\text{cool}}(\Delta t) = (-b_{\text{ic+s}}\Delta t)^{-1}$  is the cooling cutoff of IC and synchrotron losses. In the following, we omit the explicit time dependence of  $p_{\text{cool}}(\Delta t)$ . The analytical solution of the cooled spectrum (see equation (4.35)) is given by

$$f(p, \Delta t) = \begin{cases} f\left(\frac{p}{1 - p/p_{\text{cool}}}, 0\right) \left(1 - \frac{p}{p_{\text{cool}}}\right)^{-2}, & p < p_{\text{cool}} \\ 0, & p \geq p_{\text{cool}} \end{cases} \quad (4.45)$$

and the solution of the self-similar spectrum (see equation (4.36)) is

$$f_{\text{self}}(p, \Delta t) = \frac{\dot{C}_{\text{acc}} p^{-(\alpha_{\text{acc}}+1)}}{b_{\text{ic+s}}(1 - \alpha_{\text{acc}})} \begin{cases} \left(1 - \frac{p}{p_{\text{cool}}}\right)^{\alpha_{\text{acc}}-1}, & p < p_{\text{cool}}, \\ 1, & p \geq p_{\text{cool}}. \end{cases} \quad (4.46)$$

### Adiabatic Changes and Cooling

Pure adiabatic changes due to expansion or compression of the background gas leave the phase space density of the CR electrons invariant (Enßlin et al., 2007). An initial spectrum of the form

$$f_{\text{ini}}(p) = C p^{-\alpha} \Theta(p - q) \quad (4.47)$$

with normalisation  $C$ , slope  $\alpha$  and low-momentum cutoff  $q$  transforms into

$$f(p) = C x^{(\alpha+2)/3} p^{-\alpha} \Theta\left(p - x^{1/3} q\right) \quad (4.48)$$

due to an adiabatic change of the background density from  $n_{\text{ini}}$  to  $n$  and  $x = n/n_{\text{ini}}$  denotes the the ratio of final-to-initial density. Similar to the analytical description for cooling processes, this evolution can be interpreted as a shift in momentum space from an initial momentum  $p_{\text{ini}}$  to momentum  $p$  by  $p_{\text{ini}}(p, x) = p x^{-1/3}$  and an overall scaling with the factor  $x^{2/3}$

$$f(p, x) = x^{2/3} f_{\text{ini}}\left(p x^{-1/3}\right). \quad (4.49)$$

Our code adopts this equation in combination with the analytical description of radiation and Coulomb cooling processes. The evolution of the CR electron spectrum during small time intervals  $\Delta t$  and for small density ratios  $x = n(t + \Delta t)/n(t)$  is described by

$$f(p, t + \Delta t) = x^{2/3} f\left[p_{\text{ini}}\left(\frac{p}{x^{1/3}}, \Delta t\right), t\right] \frac{\dot{p}\left[p_{\text{ini}}\left(p x^{-1/3}, \Delta t\right)\right]}{\dot{p}\left(p x^{-1/3}\right)}, \quad (4.50)$$

where  $p_{\text{ini}}(p, \Delta t)$  denotes the momentum shift due to cooling as given in equation (4.40) for low momenta and in equation (4.44) for high momenta.

### Injection, Fermi-I (Re)Acceleration and Cooling

The analytic solution for the case of cooling and CR electron injection, by hadronic interactions or by our subgrid model of Fermi-I acceleration and reacceleration, is in principle given by the self-similar solution in equation (4.36) at time  $t$ . However, we cannot use the self-similar solution because (i) injection and (re)acceleration source function and cooling rates are generally time-dependent, (ii) we need to evolve the previously existing spectrum, and (iii) we evolve the spectrum on differential time steps  $\Delta t$  from time  $t_n$  to  $t_{n+1}$ . For large momenta with  $p/\dot{p}_{\text{ic+s}}(p) < \Delta t$ , we use the analytic steady-state solution. For the remaining momentum range, we use an operator-split method. First, we calculate injection and Fermi-I (re)acceleration during a half time step

$$f\left(p, t_n + \frac{\Delta t}{2}\right) = f(p, t_n) + \frac{\Delta t}{2} Q(p). \quad (4.51)$$

We then calculate the effect of cooling and adiabatic changes on  $f(p, t_n + \Delta t/2)$  during a full time step. Finally, we account for injection and (re)acceleration during another half time step to obtain the spectrum at time  $t_{n+1}$ ,

$$f(p, t_{n+1}) = f\left[p_{\text{ini}}\left(\frac{p}{x^{1/3}}, \Delta t\right), t + \frac{\Delta t}{2}\right] \frac{\dot{p}\left[p_{\text{ini}}\left(px^{-1/3}, \Delta t\right)\right]}{x^{-2/3}\dot{p}(px^{-1/3})} + \frac{\Delta t}{2} Q(p). \quad (4.52)$$

### Combining Analytical and Numerical Solutions

In general, the momentum loss rate  $\dot{p}(p)$  is the sum of all loss processes which complicates the integral in equation (4.34) and the analytical solution for  $p_{\text{ini}}(p, \Delta t)$ . As we have seen in the preceding subsections, analytical solutions are possible for both low momenta where Coulomb losses are dominating and for high momenta where inverse Compton and synchrotron losses are dominating. Our code determines the transition momenta of the numerical and analytical solutions,

$$p_{\text{low}} = \max(\{p : \tau_{\text{c}}(p) < \epsilon\tau_{\text{b+ic+s}}(p) \wedge \tau_{\text{c}}(p) \leq \tau_{\text{hyd}}\}) \quad (4.53)$$

$$p_{\text{high}} = \min(\{p : \tau_{\text{ic+s}}(p) < \epsilon\tau_{\text{b+c}}(p) \wedge \tau_{\text{ic+s}}(p) \leq \tau_{\text{hyd}}\}) \quad (4.54)$$

for low and high momenta, respectively. We also take the constraints due to the hydrodynamical time-scale  $\tau_{\text{hyd}}$  into account. The characteristic cooling time-scales are  $\tau_{\text{c}} = p/\dot{p}_{\text{c}}(p)$  for Coulomb losses,  $\tau_{\text{b}} = p/\dot{p}_{\text{b}}(p)$  for bremsstrahlung, and  $\tau_{\text{ic+s}} = p/\dot{p}_{\text{ic+s}}(p)$  for IC and synchrotron cooling. The transition momentum is determined by a free parameter, which we set to  $\epsilon = 0.1$ . The characteristic cooling time-scales and the transition momenta are displayed in Figure 4.1.

We determine corresponding indices of the transition momentum bins as

$$i_{\text{low}} = \max[0, \max(\{i : p_i < p_{\text{low}}\}) - 2] \text{ and} \quad (4.55)$$

$$i_{\text{high}} = \min[N, \min(\{i : p_i > p_{\text{high}}\}) + 3]. \quad (4.56)$$

between which the numerical solution is applied, i.e. for the momentum bins  $p_i$  with  $i \in [i_{\text{low}}, i_{\text{high}}]$ . Analytical solutions are calculated for low-momentum bins  $p_i$  with  $i \in [0, i_{\text{low}}+2]$  and high-momentum bins with  $i \in [i_{\text{high}}-3, N-1]$ . At the indices  $i_{\text{low}}+2$  and  $i_{\text{high}}-3$ , we calculate the ratio of numerical to analytical solution in the low- and high-momentum regime

$$C_{\text{low}} = \frac{\mathcal{A}_{\text{adv}}^{\text{num}}(\Delta t)f(p_{i_{\text{low}}+2}, t)}{\mathcal{A}_{\text{adv}}^{\text{ana}}(\Delta t)f(p_{i_{\text{low}}+2}, t)} \text{ and} \quad (4.57)$$

$$C_{\text{high}} = \frac{\mathcal{A}_{\text{adv}}^{\text{num}}(\Delta t)f(p_{i_{\text{high}}-3}, t)}{\mathcal{A}_{\text{adv}}^{\text{ana}}(\Delta t)f(p_{i_{\text{high}}-3}, t)}, \quad (4.58)$$

respectively, where  $\mathcal{A}_{\text{adv}}^{\text{num}}$  is the numerical advection operator and  $\mathcal{A}_{\text{adv}}^{\text{ana}}$  the analytical advection operator for low and high momenta.

The analytical solutions in the low- and high-momentum regime are multiplied with these ratios in order to guarantee a continuous spectrum. Hence, the evolved spectrum at momentum bin  $p_i$  is given by

$$f(p_i, t + \Delta t) = \begin{cases} C_{\text{low}}\mathcal{A}_{\text{adv}}^{\text{ana}}(\Delta t)f(p_i, t) & \text{for } i \in [0, i_{\text{low}}+1] \\ \mathcal{A}_{\text{adv}}^{\text{num}}(\Delta t)f(p_i, t) & \text{for } i \in [i_{\text{low}}+2, i_{\text{high}}-3] \\ C_{\text{high}}\mathcal{A}_{\text{adv}}^{\text{ana}}(\Delta t)f(p_i, t) & \text{for } i \in [i_{\text{high}}-2, N-1]. \end{cases} \quad (4.59)$$

### 4.3 Idealised One-Zone Tests

In order to demonstrate the validity of CREST, we first conduct idealised one-zone tests. These setups evolve the CR electron spectrum without an MHD simulation, hence necessary parameters for the spectral evolution are defined by hand. These tests demonstrate that our code is able to accurately and correctly simulate adiabatic processes, non-adiabatic cooling, acceleration and diffusion in momentum space.

#### 4.3.1 Adiabatic Changes

Adiabatic changes are mediated through the velocity divergence terms in equation (4.1). Due to phase space conservation upon adiabatic changes, a decreasing (increasing) gas density leads to decreasing (increasing) normalisation and a shift of the CR electron spectrum towards smaller (larger) momenta. In Figure 4.3, we follow the evolution of the

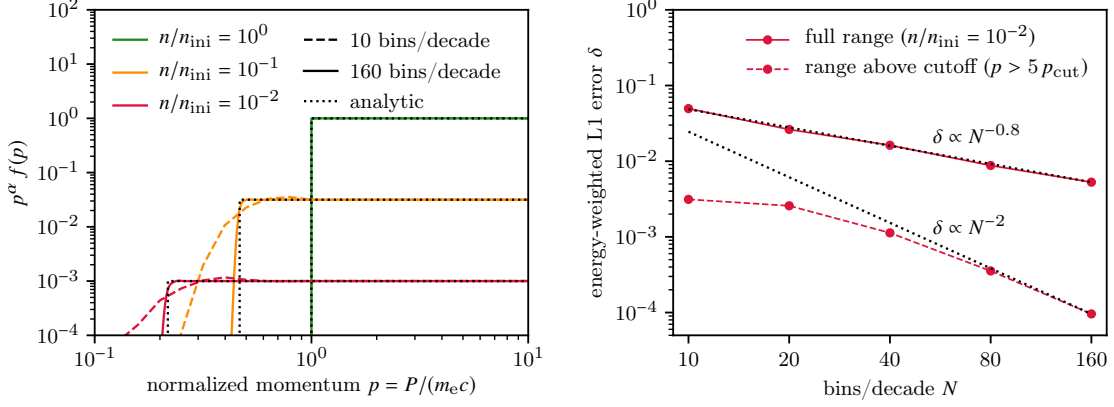


Figure 4.3: Adiabatic expansion of an initial power-law spectrum with  $\alpha = 2.5$ . Left: coloured dashed and solid lines represent the simulations with 10 and 160 bins per decade, respectively. The analytical solutions are shown as black dotted lines. Right: the energy-weighted relative L1 error for the entire momentum range and for momenta much larger than the cutoff of the analytical solution  $p_{cut} = 10^{-2/3}$ .

spectrum during an adiabatic expansion over an expansion factor of  $10^{-2}$ . The energy-weighted L1 error between the simulated spectrum  $f_{sim}$  and the analytical spectrum  $f_{ana}$  is calculated according to the formula

$$\delta = \frac{\int |f_{sim}(p) - f_{ana}(p)| T(p) dp}{\int f_{ana}(p) T(p) dp}, \quad (4.60)$$

and decreases for increasing number of momentum bins  $N$ . The error scaling for the entire momentum range shows the effect of the slope limiter, which uses a second order accurate scheme for smooth parts of the spectrum and resorts to a first order scheme near jumps or strong gradients to prevent numerical oscillations. However, in the range above the cutoff the error scales as  $\delta \propto N^{-2}$  as expected for a second-order accurate numerical scheme. We note that cooling and momentum diffusion normally lead to a smooth spectrum without sharp features. Hence, adiabatic changes are calculated with second-order accuracy.

### 4.3.2 Freely Cooling Spectrum

A CR electron spectrum may experience cooling due to Coulomb, bremsstrahlung, inverse Compton and synchrotron losses. Figure 4.4 shows the cooling of an initial power-law spectrum with spectral index of  $\alpha = 2.5$  for a setup with 10 bins per decade. We compare the fully numerical solution to the semi-analytical solution, which uses the analytical solution in the shaded momentum ranges and the fully numerical solution in the range in between, where all cooling processes modify the initial power law. The fully

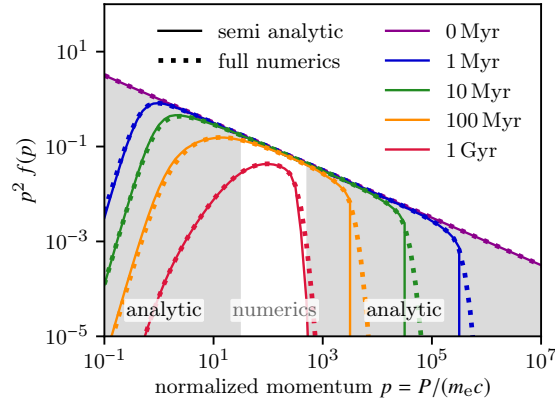


Figure 4.4: Freely cooling power-law spectrum with  $\alpha = 2.5$ . We compare the fully numerical and semi-analytical solutions, for which we adopt analytical solutions in the shaded momentum range. The simulations use 10 bins per decade and the relevant parameters are  $n_{\text{gas}} = 10^{-3} \text{ cm}^{-3}$ ,  $B = 5 \mu\text{G}$  and  $\varepsilon_{\text{ph}} = 6 \varepsilon_{\text{cmb}}$ .

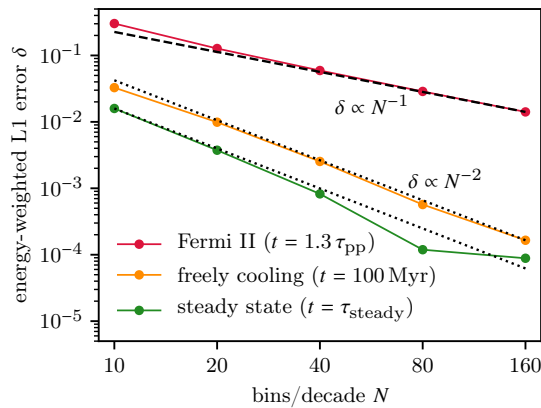


Figure 4.5: Energy-weighted relative L1 errors for cooling, steady-state and Fermi-II reacceleration tests.

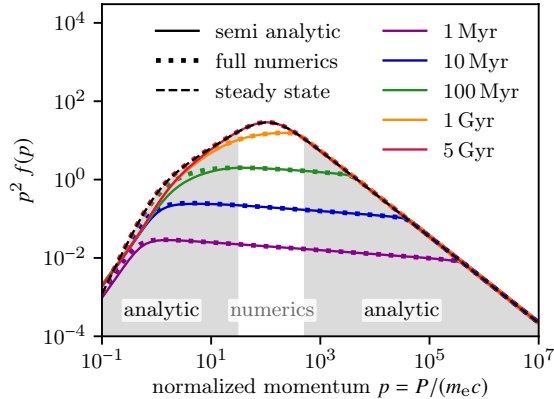


Figure 4.6: Build up of a steady-state spectrum due to continuous injection and cooling. The solid line and the dotted lines show the semi-analytical and the fully numerical simulations, respectively. The analytical steady-state solution is shown with a dashed line. The simulations use 10 bins per decade and a power-law source function with  $\alpha = 2.1$ . The relevant parameters are  $n_{\text{gas}} = 10^{-3} \text{ cm}^{-3}$ ,  $B = 5 \mu\text{G}$  and  $\varepsilon_{\text{ph}} = 6 \varepsilon_{\text{cmb}}$ .

numerical solution matches the semi-analytical solution except for the high-momentum cutoff which displays a larger diffusivity for the fully numerical scheme. The error of the fully numerical solution with  $N$  bins is calculated according to equation (4.60) where we take the simulation with double resolution as  $f_{\text{ana}} \approx f_{2N}$ . The error scaling is shown in Figure 4.5 and is second-order accurate, i.e.  $\delta \propto N^{-2}$ .

### 4.3.3 Steady-State Spectrum

The combination of cooling and continuous source function  $Q(p, t)$ , e.g. acceleration or injection, in equation (4.1) leads to the build up of a self-similar spectrum. The self-similar spectrum agrees with the steady-state spectrum for momenta that have smaller cooling time-scales in comparison to the simulation time. Hence, the self-similar spectrum completely approaches the steady-state spectrum for very long times. We show this evolution in Figure 4.6 where we compare the results of the fully numerical and the semi-analytical simulations as well. Both simulations agree relatively well and approach the steady-state solution. However, there is a small deviation of the semi-analytical simulation visible in the Coulomb regime at around  $p = 1$ . This is a consequence of the approximations adopted that enable an analytical solution for Coulomb cooling. Nevertheless, we prefer the semi-analytical simulation as it generally outperforms in efficiency in comparison to the fully numerical simulation (it is faster by a factor of  $\sim 10^4$  for this specific setup). The error of the fully numerical solution compared to the analytical steady-state solution (see equations (4.37) and (4.60)) is shown in Figure 4.5 and scales

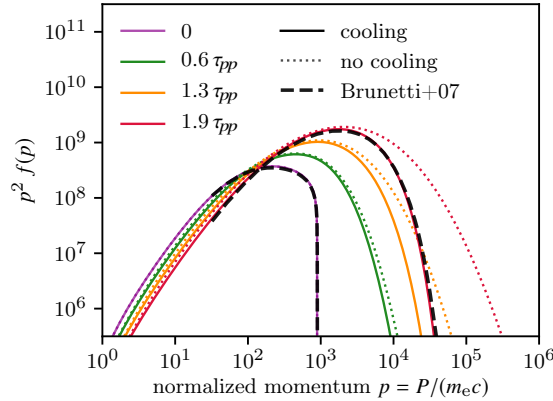


Figure 4.7: Fermi-II reacceleration with and without cooling of a relic spectrum in comparison to a reference study (Brunetti and Lazarian, 2007). The semi-analytical and fully numerical simulations that include cooling are indistinguishable. The relevant parameters are  $n_{\text{gas}} = 10^{-3} \text{ cm}^{-3}$ ,  $B = 1 \mu\text{G}$ ,  $\varepsilon_{\text{ph}} = \varepsilon_{\text{cmb}}$  and  $\tau_{pp} = 0.2 \text{ Gyr}$ . The time steps given in multiples of  $\tau_{pp}$  are 0, 127, 254, and 381 Myr.

with  $\delta \propto N^{-2}$ .

#### 4.3.4 Fermi-II Reacceleration

In addition to adiabatic changes, cooling, Fermi-I (re)acceleration, and injection, the CR electron spectrum may experience Fermi-II reacceleration, which is described by the momentum diffusion terms in equation (4.1) and which increases the energy of the spectrum. We adopt a typical value for the diffusion time of  $\tau_{pp} = 0.2 \text{ Gyr}$  in our tests. In Figure 4.7, we show two simulations with and without cooling for a high resolution of 160 bins per decade for Fermi-II reacceleration. Both simulations start with the same initial spectrum, which we have taken from a study on Fermi-II reacceleration of CR electrons by Brunetti and Lazarian (2007). The simulation with cooling approaches a limit for high momenta where cooling dominates over the reacceleration by the Fermi-II process. The result of the simulation with cooling matches the reference simulation by Brunetti and Lazarian (2007) very well. The simulation without cooling shows the main effect of Fermi-II reacceleration, i.e. diffusion in momentum space and a shift towards higher particle energies.

Figure 4.5 shows the error scaling of the different simulations with number of bins per momentum decade. The error is calculated with equation (4.60). However, for the simulations of freely cooling and momentum diffusion, we compare the result at given resolution  $f_N$  to the double resolution, i.e.  $f_{\text{ana}} \approx f_{2N}$ . The implemented Crank–Nicolson scheme is only accurate to first order in momentum space as can be seen by the  $\delta \propto N^{-1}$

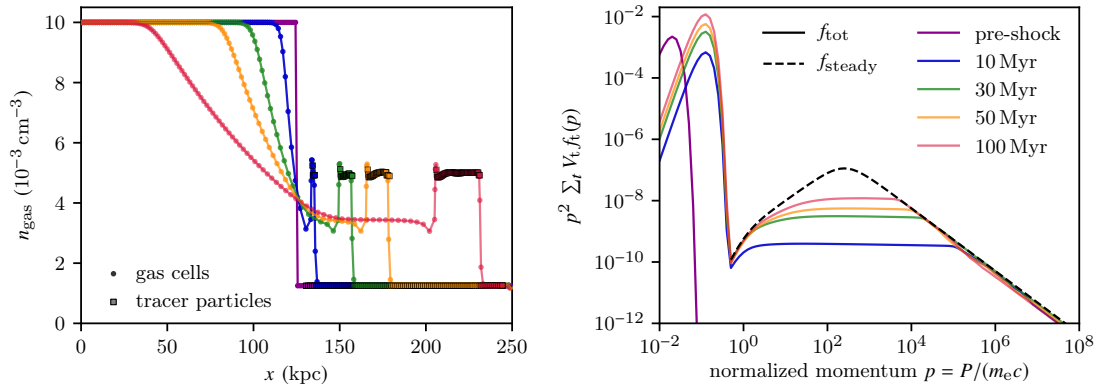


Figure 4.8: 1D shock-tube test of a strong shock ( $\mathcal{M} = 8.43$ ,  $\alpha_{\text{acc}} = 2.0$ ) with 200 cells and 100 tracer particles. The left-hand panel shows the gas density profiles together with the tracer particles on which we evolve the CR electron spectra at different times. The right-hand panel shows the different total volume integrated thermal and CR electron spectra and the theoretically expected steady-state spectrum (dashed), for which we adopt  $\alpha_{\text{acc}} = 2.02$  instead of the theoretical value 2.0 to account for the numerical scatter of the shock compression ratio (see Figure 4.9). We adopt the parameters  $B = 1 \mu\text{G}$  and  $\varepsilon_{\text{ph}} = 6 \varepsilon_{\text{cmb}}$ .

scaling. We consider this result for the Fermi-II reacceleration as a proof of concept. The improvement of the diffusion operator is straightforward but beyond the scope of this paper. The simulation of freely cooling and steady state show an error scaling of  $\delta \propto N^{-2}$  which reflects our second-order accurate scheme for advection with a slope limiter.

## 4.4 Hydrodynamical Simulations

In addition to idealised one-zone tests, we demonstrate that CREST works in tandem with a hydrodynamical code. To this end, we use the second-order accurate, adaptive moving-mesh code AREPO (Springel, 2010; Pakmor et al., 2016c) for simulations with ideal MHD (Pakmor and Springel, 2013). CR protons are modelled as a relativistic fluid with a constant adiabatic index of  $\gamma_{\text{crp}} = 4/3$  in a two-fluid approximation (Pfrommer et al., 2017a). We include Lagrangian tracer particles, which are velocity field tracers (Genel et al., 2013) and are passively advected with the gas and on which we solve the CR electron transport equation in post processing on every MHD time step.

To assess the validity of our setup, we investigate two different hydrodynamical scenarios, shock-tube simulations and 3D Sedov–Taylor blast-wave simulations. This enables us to probe Fermi-I acceleration and reacceleration, cooling and adiabatic processes in more realistic setups. The CR electron spectrum is calculated in post-processing separately for every tracer particle and the relevant parameters for the spectral evolution are taken from

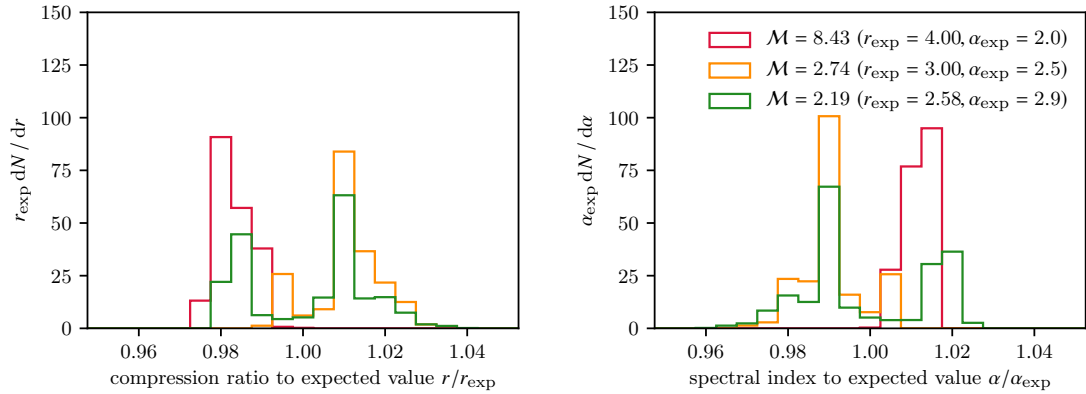


Figure 4.9: Histograms of the compression ratio (left-hand panel) and spectral index (right-hand panel), which are both normalised to their expected values for three different 1D shock-tube tests, which use the parameters given in table 4.1. The histograms account for all tracer particles at all time steps provided they experience an acceleration event.

Table 4.1: Initial values of our shock-tube setups. The parameters  $n_L = 1 \times 10^{-2} \text{ cm}^{-3}$ ,  $P_{\text{th,L}} = 2.62 \times 10^{-11} \text{ erg cm}^{-3}$  and  $P_{\text{crp,L}}/P_{\text{th,L}} = 2$  for the left initial state and  $n_R = 0.125 \times 10^{-2} \text{ cm}^{-3}$  and  $P_{\text{crp,R}}/P_{\text{th,R}} = 1$  for the right initial state are the same for all simulations.

$P_{\text{th,R}} \text{ (erg cm}^{-3}\text{)}$	$P_{\text{th,L}}/P_{\text{th,R}}$	$\mathcal{M}$	$r$	$\alpha_{\text{acc}}$
$1.06 \times 10^{-13}$	247.0	8.43	4.0	2.0
$3.14 \times 10^{-13}$	23.4	2.74	3.0	2.5
$1.89 \times 10^{-12}$	13.9	2.19	2.58	2.9

the gas cells which contain the tracer particles.

#### 4.4.1 Shock Tubes

First, we perform a series of shock-tube tests (Sod, 1978) in AREPO with various shock strengths. The fluid is composed of gas and CR protons and we take CR acceleration at the shock in account (Pfrommer et al., 2017a) with CR proton shock acceleration efficiency of  $\zeta_{\text{crp}} = 0.1$ . In our 1D setups, we use a box with 250 kpc side length and 200 cells. In addition 100 tracer particles are located in the initial state on the right-hand side. For the 3D simulations, we use a box of dimension  $250 \times 25 \times 25$  kpc with  $200 \times 20 \times 20$  cells and  $100 \times 10 \times 10$  tracer particles in the initial state on the right-hand side. The tracer particles initially only contain a thermal electron spectrum. The initial states of the Sod shock-tube problem are laid down in table 4.1. We vary the thermal pressure  $P_{\text{th,R}}$  in order to obtain a desired Mach number  $\mathcal{M}$  and 1D acceleration spectral index  $\alpha_{\text{acc}}$ , which is a function of

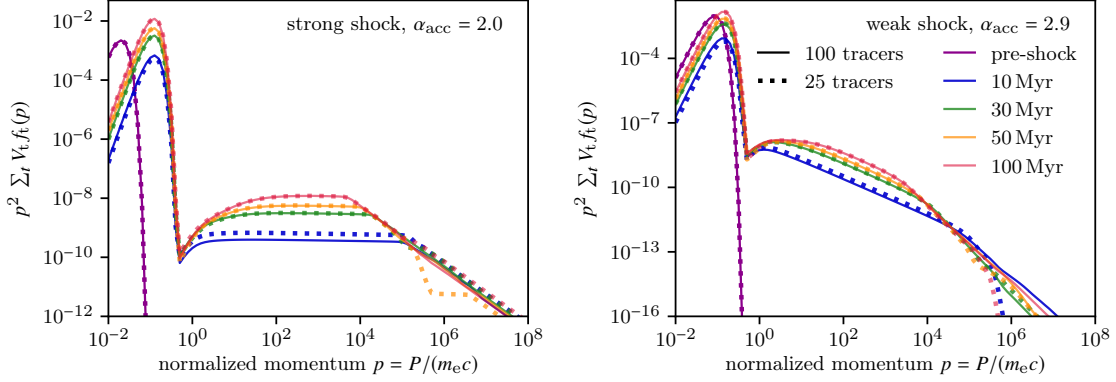


Figure 4.10: Tracer particle resolution study for 1D shock tubes of a strong shock (left-hand panel) and a weak shock (right-hand panel). The solid lines display the simulation with 100 tracer particles, which is for the strong shock identical to the right-hand panel in Figure 4.8, and the dotted line displays the simulation with 25 tracer particles. Low-resolution runs show temporary dips, but generally match the high-resolution runs well.

the shock compression ratio  $r$ , i.e.  $\alpha_{\text{acc}} = (r + 2)/(r - 1)$ .

Figure 4.8 shows a 1D shock-tube test of a strong shock ( $\mathcal{M} = 8.43$ ,  $\alpha_{\text{acc}} = 2.0$ ). The left-hand panel shows the gas density together with the tracer particles for different snapshots. The right-hand panel shows the thermal and CR electron spectra as a volume integrated sum of the tracer particle spectra, which have thermal spectra in the initial state. Except for the initial state at  $t = 0$ , we sum up only spectra from those particles that have already encountered the shock front. Due to the initial inhomogeneity, a shock develops and propagates into the state on the right-hand side where the first tracer particle crosses the shock after  $\sim 5$  Myr. As soon as a tracer particle encounters the shock front, CR electron acceleration is triggered, i.e. we use a source term of the form  $Q_e(p) \propto p^{-\alpha_{\text{acc}}}$  in the transport equation (see equations (4.1) and (4.9)). The CR electron spectra experience losses due to Coulomb, bremsstrahlung, inverse Compton, and synchrotron interactions at the same time. Hence, the total spectrum has the form of a self-similar spectrum (see equation (4.36)).

The spectrum in Figure 4.8 approaches a steady state in the momentum regime, which has a shorter cooling time in comparison to the time since the first shock encounter. The total spectrum is similar to our idealised one-zone test, which simulates only one spectrum that experiences continuous cooling and injection. However, the simulation with AREPO uses many tracer particles which experience acceleration only for limited amount of time when the particle resides in a shock surface or post shock cell of the hydrodynamical simulation. This clearly demonstrates that the combination of numerical and analytical solutions produces an effective, stable and accurate algorithm.

As pointed out before, the spectral index  $\alpha_{\text{acc}}$  of the accelerated spectrum depends on

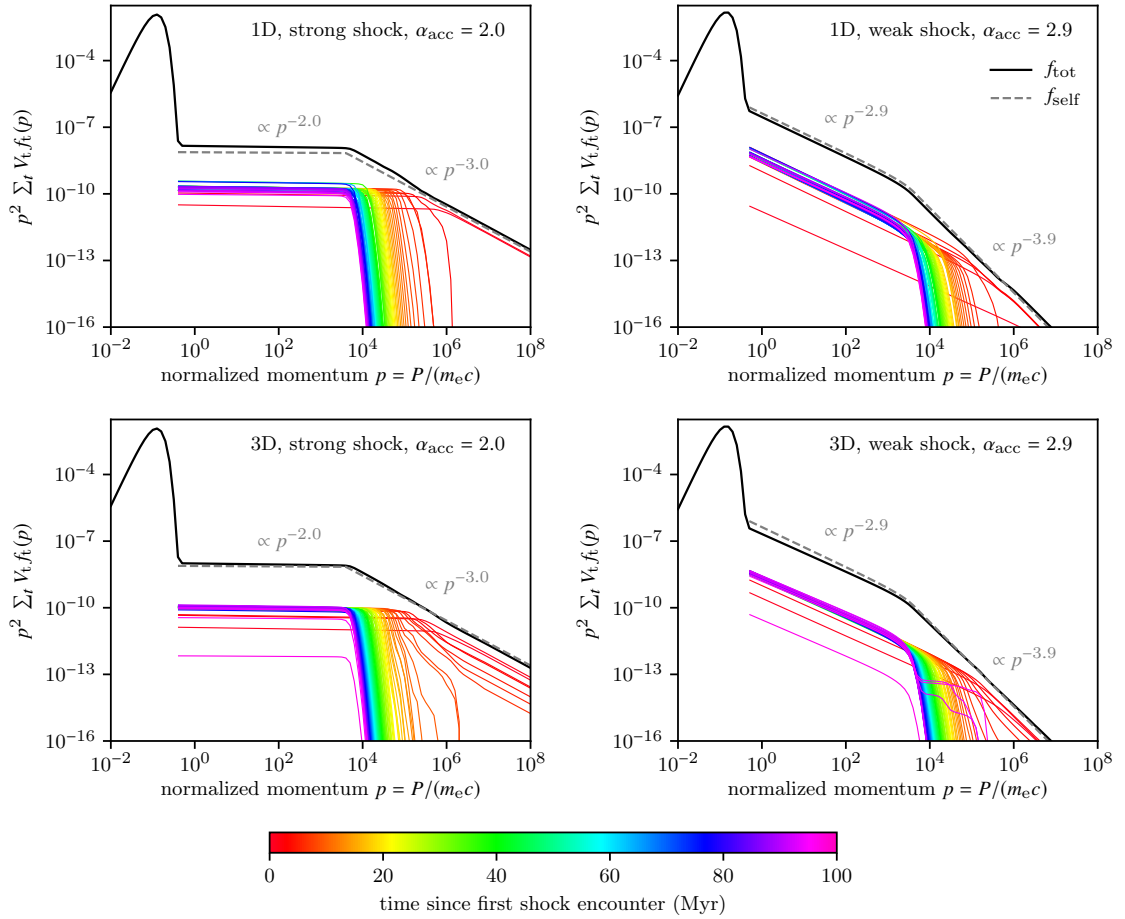


Figure 4.11: Total thermal and CR electron spectra at 100 Myr (black solid lines) and partial spectra of 100 time intervals since first shock encounter (coloured thin solid lines) for 1D and 3D shock-tube simulations (top and bottom, respectively) of strong and weak shocks (left- and right-hand panels, respectively). The theoretically expected steady-state spectrum (dashed) matches the total spectrum very well. Inverse Compton and synchrotron cooling lead to steeper spectra for large momenta. Note that Coulomb and bremsstrahlung cooling is neglected here.

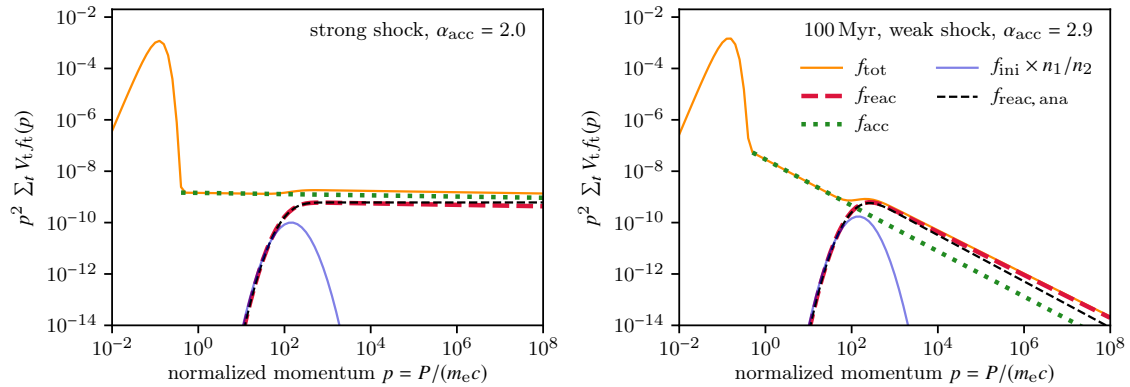


Figure 4.12: Comparison of direct acceleration (green dotted) and reacceleration (red dashed) without cooling in 1D shock-tube simulations for a strong and a weak shock (left- and right-hand panels, respectively). We show the initial relic spectrum (blue) and the total spectrum after the acceleration event (orange). The theoretically expected reacceleration spectrum matches the simulation very well.

the shock compression ratio which is subject to numerical inaccuracies. In Figure 4.9, we show histograms for ratios of the numerically obtained value of shock compression to its expected value  $r/r_{\text{exp}}$  and ratios of the numerically obtained value of spectral index to its expected value  $\alpha/\alpha_{\text{exp}}$  for three different shock strengths (or equivalently Mach numbers). Here, we calculate the shock compression ratio with equation (4.29), which depends on the Mach number and which is formally only accurate for a single polytropic fluid. However, this calculation yields better results in comparison to the shock compression ratio directly calculated by the AREPO shock finder. The resulting numerical error for the Mach number is typically better than one per cent (and deteriorates up to two per cent for weak shocks).

A resolution test of the number of tracer particles is shown in Figure 4.10, which displays the total spectra for 25 and 100 tracer particles for strong and weak shocks. The low-resolution spectra can show temporary dips due to poor sampling of the tracer particles in space, in particular at high momenta. However, low-resolution runs are stable and reproduce the general result of high-resolution runs. This demonstrates that our code produces stable and accurate results (only limited by the sampling rate) with respect to a coarser sampling of the tracer particles than the gas cells.

The total spectrum is a sum of all tracer particle spectra as we show in Figure 4.11. There, we plot the results of 1D and 3D simulations for strong and weak shocks. Note that we only consider inverse Compton and synchrotron cooling for clarity. Each panel shows the total spectrum, the theoretically expected self-similar spectrum, and partial sums of spectra of 100 equally spaced time intervals since the first shock encounter. Those particles that have most recently crossed the shock (red lines) experience simultaneously acceleration and cooling and show a self-similar spectrum. The spectra of those particles

that have encountered the shock some time ago (orange to purple lines) show an exponential high-momentum cutoff resulting from the freely cooling CR electron population. The total spectrum has the slope of the acceleration spectrum for those momenta which have cooling times longer than 100 Myr, i.e.  $p \lesssim 10^4$  for these setups. At larger momenta,  $p \gtrsim 10^4$ , the slope of the total spectrum steepens to  $\alpha_{\text{acc}} + 1$  as expected from equation (4.46). The total spectra for all setups match the theoretically expected self-similar spectra very well, although slight deviations are visible. These follow from the numerical scatter of the shock compression ratio in AREPO. We note that the computation of the CR electron spectrum with CREST is faster than the hydrodynamical simulation by a factor of about 20 in the 3D shock-tube simulations.

In addition to direct acceleration of primary CR electrons at the shock, a previously existing non-thermal CR electron population can be reaccelerated at the shock. We show the resulting spectra for a strong and a weak shock after 100 Myr in Figure 4.12. The setups are similar to the simulations presented above except for the previously existing non-thermal relic spectrum and except for the fact that we deactivated CR electron cooling for clarity here. As soon as a tracer particle encounters the shock, it experiences both, reacceleration of the initial relic spectrum and direct acceleration of a primary power-law spectrum. Each panel shows the initial relic spectrum (blue), the total spectrum after the acceleration event (orange), the directly accelerated spectrum (green dashed line), and the reaccelerated spectrum (red dashed line). The theoretically expected reaccelerated spectrum is also shown (black dashed line) and matches the simulated reacceleration spectrum. The slope of the reaccelerated spectrum in the weak-shock case deviates slightly from its theoretical expectation because of numerical scatter of the shock compression ratio (see Figure 4.9).

In the case of a strong shock, the primary accelerated spectrum dominates over the reaccelerated spectrum, hence the total spectrum is only weakly modified by reacceleration (see Figure 4.12). In contrast, the reaccelerated spectrum dominates the total spectrum for large momenta at weak shocks. This is important for observable signatures such as, e.g. the flux of radio emission. We note that the relative strength between direct acceleration and reacceleration depends on the details of shock acceleration, which we do not resolve with our hydrodynamical simulations. In our setup, we convert a fixed fraction of the accelerated CR proton energy into CR electrons at the shock which leads to a larger normalisation for steeper spectra. Other shock acceleration models, e.g. thermal leakage models (Kang and Ryu, 2011), predict different relative strengths of reacceleration to direct acceleration.

#### 4.4.2 Sedov–Taylor Blast Wave

In addition to the shock-tube tests we perform simulations of spherical shocks in order to test acceleration and cooling in tandem with adiabatic CR electron expansion. We setup a 3D Sedov–Taylor problem with an energy-driven spherical shock which expands into a medium with negligible pressure. We use a symmetric 3D box with  $200^3$  cells, 100 pc side

#### 4.4. HYDRODYNAMICAL SIMULATIONS

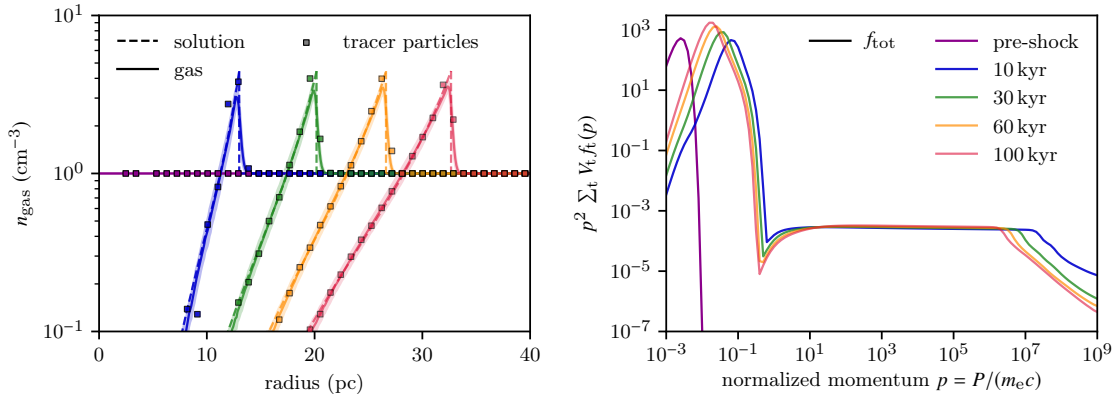


Figure 4.13: 3D Sedov–Taylor blast-wave simulation with  $200^3$  gas cells and  $\sim 30^3$  tracer particles. The left-hand panel shows the radial gas density profile (solid), the theoretical solution (dashed) and the spherically-averaged density of the tracer particles within concentric shells (points) for different times. The right-hand panel shows the total initial thermal spectrum (purple) and the total spectrum of particles, which have crossed the shock, at four characteristic times.

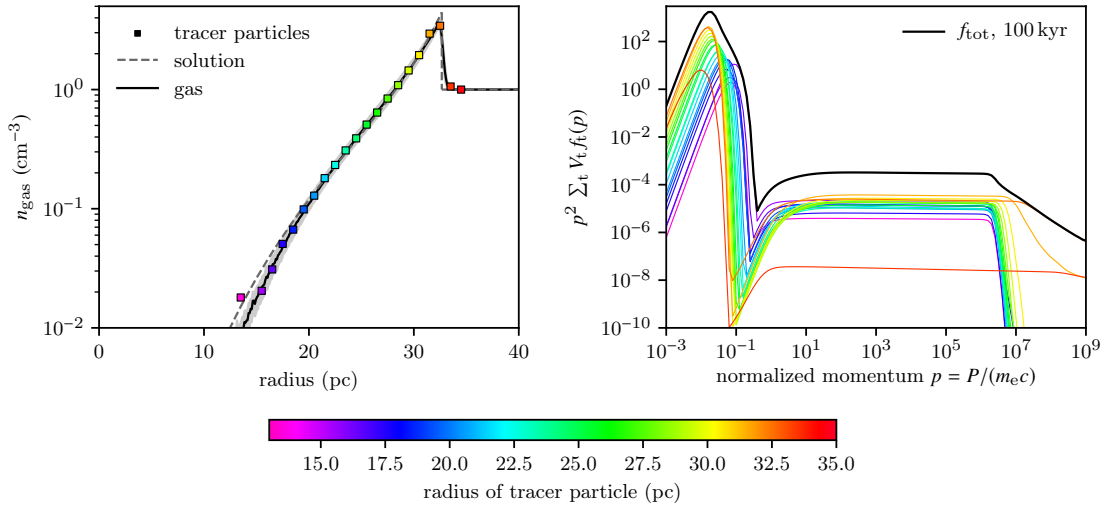


Figure 4.14: Spherically-averaged tracer particle density (left-hand panel) and the contribution of tracer particles to the total spectrum (right-hand panel) for the 3D Sedov–Taylor blast-wave simulation at 100 kyr. The colour indicates the different radii of tracer particles, which correspond to different times since shock crossing. The radial bins for the tracer particles have a width of 1 pc and the grey band denotes the density scatter of the simulation.

length and the following parameters for the initial conditions: The gas number density of the ambient medium is  $n_{\text{gas}} = 1 \text{ cm}^{-3}$ , has a temperature of  $T = 10^4 \text{ K}$  and a thermal adiabatic index of  $\gamma_{\text{th}} = 5/3$ . We inject an initial thermal energy of  $E_0 = 10^{51} \text{ erg}$  into the central cell. The tracer particles are initially located on a regular Cartesian mesh with  $30^3$  grid points of which we excise a small spherical region around the centre. The tracer particles initially only contain a thermal electron spectrum.

The left-hand panel of Figure 4.13 shows the simulated gas density profile for different snapshots together with the theoretical solution and the spherically-averaged density of the tracer particles within concentric shells. As expected for a single polytropic fluid, the shock radius of the 3D explosion evolves as

$$r_{\text{shock}}(t) = \left( \frac{E_0}{\alpha \rho_0} \right)^{1/5} t^{2/5}, \quad (4.61)$$

where  $\rho_0$  is the ambient mass density and  $\alpha$  the self-similarity parameter of the Sedov (1959) solution. In our simulation, we adopt a CR shock acceleration efficiency of  $\zeta_{\text{CR}} = 0.1$ , which yields an effective adiabatic index  $\gamma_{\text{eff}} = 1.58$  and a self-similarity parameter  $\alpha = 0.57$  (Pais et al., 2018a). We note that the tracer particles experience a slightly smaller density jump of  $r \approx 4$  in comparison to the theoretically expected value of  $r = 4.45$  in this setup due to the narrow density jump of the theoretical solution and the limited spatial resolution of the hydrodynamical simulation.

The right-hand panel of Figure 4.13 shows the total electron spectrum, where we only take the spectrum of those particles into account which have already crossed the shock front except for the initial spectrum with all tracer particles. It is apparent that the total spectrum is approximately constant for all snapshots at momenta  $10^1 \lesssim p \lesssim 10^6$  where the time-scales of Coulomb, inverse Compton, and synchrotron cooling are longer than our simulation time. This is a consequence of constant kinetic and total energy of the shock of a Sedov–Taylor blast wave. In the thin-shell approximation, all mass is contained in a shell of radius  $r_{\text{shock}}$  that expands with velocity  $v_{\text{post}} = 2v_{\text{shock}}/(\gamma_{\text{eff}} + 1)$ , which yields a constant kinetic energy of  $E_{\text{kin}} = 32\pi E_0 / [75\alpha(\gamma_{\text{eff}} + 1)^2] \approx 0.35E_0$ . A fraction of this energy goes into CR electrons, and particles that have recently crossed the shock dominate the spectrum. We note that we obtain robust results for the CR electron spectrum although the tracer particles are more coarsely sampled than the gas cells by a factor of  $\sim 6^3$ .

The contribution to the total spectrum of tracer particles at different radii is shown in Figure 4.14. Red lines represent the radial bin at which only a fraction of tracer particles experience shock acceleration. Hence, their spectra are subdominant to the total spectrum. The total spectrum is dominated by particles whose distance to the centre is close the maximum of the radial gas density profile as they all experience shock acceleration and have not yet lost energy due to adiabatic expansion. Yellow to purple lines represent particles which are located towards inner radii and which are effected by cooling due to adiabatic expansion and non-adiabatic processes. These tests demonstrate that our code also handles adiabatic expansion together with acceleration and cooling of CR electrons.

We note that the CR electron spectrum is efficiently calculated with `CREST`, which is faster than the hydrodynamical simulation by a factor of about 460.

## 4.5 Conclusions

We have presented our stand-alone post-processing code `CREST` that evolves the spectra of CR electrons on Lagrangian trajectories spatially and temporally resolved. So far, we model the spatial CR electron transport as advection with the gas and defer modelling CR electron streaming and (spatial) diffusion to future work. All important physical cooling processes of CR electrons are included, i.e. adiabatic expansion, Coulomb cooling, and radiative processes such as inverse Compton, synchrotron and bremsstrahlung cooling. In addition to adiabatic compression, we account for non-adiabatic energy gain processes such as diffusive shock acceleration and reacceleration as well as Fermi-II reacceleration via particle interactions with compressible turbulence.

The CR electron cooling times at very low and very high momenta are much smaller than typical time steps in simulations of galaxy formation or the ISM. Hence, we develop a hybrid algorithm that combines numerical and analytical solutions to the Fokker–Planck equations such that the resulting code works efficiently and accurately on the MHD time step. We demonstrate in a number of code validation simulations that the result of our hybrid algorithm is as good as the fully numerical solution, which is however computationally considerably more expensive. This hybrid treatment decreases the computational cost of evolving the CR electron spectrum and renders cosmological simulations with CR electrons feasible.

`CREST` has been extensively tested in idealized one-zone models and alongside hydrodynamical simulations of the `AREPO` code. Idealized one-zone tests demonstrate that isolated terms of the Fokker–Planck equation are accurately captured with our code. The `AREPO` simulations show (i) that `CREST` works very well and efficiently together with a hydrodynamical code at almost negligibly additional computational cost, (ii) that the total spectrum, which is the sum of singular spectra on tracer particles, evolves as expected, and (iii) that the spatial sampling of the tracer particles quickly converges with increasing number of tracer particles. In particular, our results are robust to a coarser sampling of the tracer particles in comparison to the resolution of our unstructured mesh. Future studies will show how the spectral properties depend on the spatial sampling rate in more complex simulations of realistic environments. We note that our algorithm (and code) can in principle be combined with every (magneto)hydrodynamical code that has Lagrangian tracer particles on which the comoving Fokker–Planck equations for the CR electron spectrum is solved.

The presented method allows studying the evolution of the CR electron spectrum in the ISM, in galaxies and galaxy clusters as well as for AGN jets in great detail. It enables to link the non-thermal physics to observables such as  $\gamma$ -ray and radio measurements and to distinguish leptonic and hadronic emission scenarios. These include SNRs where we can

gain insight which environmental parameter (mean density, density fluctuations, magnetic field strength) determines the dominating emission scenario. It will further allow us to perform self-consistent studies on the evolution of the Fermi bubbles or galactic outflows in MHD simulations and to test models that rely on star formation or on AGN activity. This insight will be key for a more profound understanding of the most important feedback processes during the formation of galaxies. Finally, our code `CREST` will enable us to self-consistently follow the CR electron spectrum during the evolution of galaxy clusters, it can possibly help to understand the enigmatic formation scenarios of radio relics and radio haloes and how they relate to the dynamical state of clusters.

# 5 Evolution and Observational Signatures of the Cosmic Ray Electron Spectrum in SN 1006

This chapter presents our work published in Winner et al. (2020). Supernova remnants (SNRs) are believed to be the source of Galactic cosmic rays (CRs). SNR shocks accelerate CR protons and electrons which reveal key insights into the non-thermal physics by means of their synchrotron and  $\gamma$ -ray emission. The remnant SN 1006 is an ideal particle acceleration laboratory because it is observed across all electromagnetic wavelengths from radio to  $\gamma$ -rays. We perform three-dimensional (3D) magnetohydrodynamics (MHD) simulations where we include CR protons and follow the CR electron spectrum. By matching the observed morphology and non-thermal spectrum of SN 1006 in radio, X-rays and  $\gamma$ -rays, we gain new insight into CR electron acceleration and magnetic field amplification. 1. We show that a mixed leptonic-hadronic model is responsible for the  $\gamma$ -ray radiation: while leptonic inverse-Compton emission and hadronic pion-decay emission contribute equally at GeV energies observed by *Fermi*, TeV energies observed by imaging air Cherenkov telescopes are hadronically dominated. 2. We show that quasi-parallel acceleration (i.e. when the shock propagates at a narrow angle to the upstream magnetic field) is preferred for CR electrons and that the electron acceleration efficiency of radio-emitting GeV electrons at quasi-perpendicular shocks is suppressed at least by a factor ten. This precludes extrapolation of current one-dimensional plasma particle-in-cell simulations of shock acceleration to realistic SNR conditions. 3. To match the radial emission profiles and the  $\gamma$ -ray spectrum, we require a volume-filling, turbulently amplified magnetic field and that the Bell-amplified magnetic field is damped in the immediate post-shock region. Our work connects micro-scale plasma physics simulations to the scale of SNRs.

## 5.1 Introduction

Supernova remnants (SNR) accelerate particles to TeV energies at their shock fronts via diffusive shock acceleration (DSA, Krymskii, 1977; Axford et al., 1977; Blandford and Ostriker, 1978; Bell, 1978a,b) and are believed to be the source of cosmic rays (CR) in our Galaxy (Reynolds, 2008). The remnant of the type Ia supernova SN 1006, also known as the Chinese supernova, is an ideal laboratory to study CR acceleration.

The shell-type remnant has been observed at various wavebands, e.g. in the radio (Gardner and Milne, 1965; Dyer et al., 2009), infrared (Winkler et al., 2013), optical (Winkler et al., 2003), X-ray (Winkler and Long, 1997; Bamba et al., 2003; Cassam-Chenaï et al., 2008; Li et al., 2018) and  $\gamma$ -ray regime (Acero et al., 2010; Abdo et al., 2010; Condon et al., 2017). It is located approximately 400 pc above the galactic plane within a distance of 1.45 to 2.2 kpc (Winkler et al., 2003; Katsuda, 2017). SN 1006 shows a bilateral symmetry (also called bipolar), i.e. it has radio bright limbs in the northeast (NE) and southwest (SW) which are separated by a dim centre. The location of these spatially coincide with those in non-thermal X- and  $\gamma$ -rays.

Observations made with the ROSAT and ASCA satellites showed that the X-ray emission at the edges of SN 1006 is due to CR electrons which are accelerated at the shock front and emit synchrotron radiation (Koyama et al., 1995; Willingale et al., 1996). The same population of CR electrons is responsible for the radio emission. However, the  $\gamma$ -ray emission could be a result of CR protons inelastically interacting with the ambient gas (hadronic model) and/or CR electrons scattering off of ambient photons via the inverse Compton (IC) effect (leptonic model). It has been discussed whether the  $\gamma$ -ray emission of SN 1006 is predominantly of hadronic (Berezhko et al., 2012; Miceli et al., 2014) or of leptonic origin (Petruk et al., 2011; Araya and Frutos, 2012; Acero et al., 2015; Xing et al., 2019).

The observed morphology in radio and X-rays has been discussed in context of the orientation of the magnetic field and the acceleration mechanism of CR electrons. In the equatorial-belt model, the magnetic field direction is aligned along the southeast (SE) to northwest (NW) direction and the CR electron acceleration is isotropic or preferentially quasi-perpendicular (Fulbright and Reynolds, 1990; Reynolds, 1996; Petruk et al., 2009; Schneider et al., 2010). However, this equatorial-belt model of the magnetic field is in contradiction to the inferred magnetic orientation in radio polarization observations which suggest a magnetic field aligned along the NE-SW direction (Reynoso et al., 2013). This problem is resolved by the polar cap model which relies on a magnetic field oriented along the NE to SW direction and preferentially quasi-parallel acceleration (Völk et al., 2003). Azimuthal variations of X-ray cutoff frequencies (Rothenflug et al., 2004; Katsuda et al., 2010) and of the ratio of radii between the forward shock and contact discontinuity (Cassam-Chenaï et al., 2008) favour the polar cap model. The polar cap model is further supported by 3D MHD simulations (Bocchino et al., 2011; Schneider et al., 2015).

The observed synchrotron radiation is an indicator of strong magnetic fields. Analysis of the thin X-ray synchrotron rims at SN 1006 suggests post-shock magnetic fields of 70 to 200  $\mu$ G (Ressler et al., 2014). Analysis of the multi-frequency spectrum including the  $\gamma$ -ray data finds effective (one-zone) magnetic fields of 30  $\mu$ G in the case of a leptonic model and 120  $\mu$ G in the case of a hadronic model for the  $\gamma$ -ray emission (Acero et al., 2010).

As the remnant SN 1006 evolves in a homogeneous environment high above the galactic plane, the remnant is surrounded by interstellar magnetic fields of the order of 1  $\mu$ G. Therefore, other mechanisms than adiabatic compression of the magnetic fields must be

responsible for generating effective magnetic fields with  $B \gg 10 \mu\text{G}$  in the downstream of the shock. First, the non-resonant hybrid instability which is driven by CR protons at the shock amplifies magnetic fields (Bell, 2004). Studies of amplified fields at SNRs (Pohl et al., 2005) and at relativistic pair plasma shocks (Chang et al., 2008; Keshet et al., 2009) show that these fields are quickly damped. Secondly, the interaction of the shock with small scale density inhomogeneities of the surrounding interstellar medium can drive a small-scale dynamo which can strongly amplify the magnetic field (Giacalone and Jokipii, 2007; Ji et al., 2016).

The amplification of magnetic fields is supported by observations of other SNRs, e.g. the variability of X-ray hot spots of the SNR RXJ1713.7-3946 is an indicator of magnetic field amplification up to values larger than 1 mG (Uchiyama et al., 2007). Another example of highly amplified magnetic fields is the SNR Vela Jr (RXJ0582.0-4622). The analysis of X-ray filaments suggests highly amplified downstream magnetic fields of  $B \gtrsim 100 \mu\text{G}$  which favors a hadronic model for the observed  $\gamma$ -ray emission (Bamba et al., 2005; Berezhko et al., 2009). However, a leptonic model with weaker magnetic fields cannot be ruled out (Tanaka et al., 2011) or is favored if magnetic fields are strongly damped to  $\sim 10 \mu\text{G}$  in the downstream of the shock (Sushch et al., 2018).

Here, we study these topics with 3D MHD simulations of the remnant SN 1006 together with magnetic-obliquity dependent acceleration of CR protons and electrons. We follow the spectrum of CR electrons spatially and temporally resolved in order to compare simulations with the observed multi-frequency spectrum and morphology at different wavebands.

Our work has the following structure. We present our simulation setup in Section 5.2. Then we present our best-fit model and discuss whether the high energy  $\gamma$ -ray emission is due to leptonic or hadronic processes in Section 5.3. We continue with the discussion on obliquity dependent acceleration of CR electrons in Section 5.4 and damping of amplified magnetic fields in Section 5.5. After that, we discuss the influence of various parameters onto the spectrum in Section 5.6. We conclude with a discussion of our results in Section 5.7. Throughout this work, we denote photon energies by  $E$ , electron energies and normalized (dimensionless) momenta by  $E_e$  and  $p_e = P_e/(m_e c)$ , and proton energies and normalized momenta by  $E_p$  and  $p_p = P_p/(m_p c)$ . Here,  $P_e$  and  $P_p$  are the physical electron and proton momenta in units of  $\text{g cm s}^{-1}$ , respectively,  $m_e$  and  $m_p$  are the electron and proton masses, respectively, and  $c$  is the speed of light.

## 5.2 Simulation Setup

### 5.2.1 Simulation Codes

We perform 3D MHD simulations with the second-order accurate, adaptive moving-mesh code AREPO (Springel, 2010; Pakmor et al., 2016c) which employs an unstructured mesh that is defined as the Voronoi tessellation of a set of mesh-generating points. We

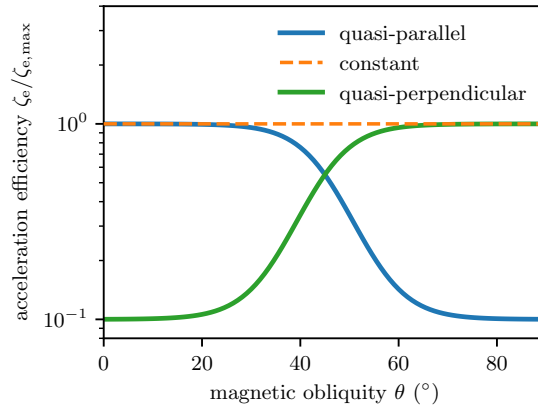


Figure 5.1: Obliquity-dependent electron acceleration efficiency for three base acceleration models. Best fits are produced with the preferred quasi-parallel acceleration efficiency (blue).

account for the transport of CR protons which are treated as a relativistic fluid with an effective adiabatic index of  $4/3$  (Pfrommer et al., 2017a). We employ the shock finder (Schaal and Springel, 2015) which localises and characterises shocks according to the Rankine–Hugoniot jump conditions and inject CR energy into the Voronoi cells of the shock and immediate post-shock regime (Pfrommer et al., 2017a). We account for the dominant advective transport of CR protons and neglect CR streaming and diffusion. While a combination of adiabatic gains due to the converging flow at the shock and spatial diffusion (close to the Bohm limit) gives rise to diffusive shock acceleration (Blandford and Eichler, 1987), we do not resolve the growth of non-resonant Bell (2004) modes of the hybrid instability in our simulations. In consequence, we describe diffusive shock acceleration as well as Bell amplification in form of subgrid models detailed below in Sections 5.2.2 and 5.2.3.

In addition, we follow the evolution of the CR electron spectrum spatially and temporally resolved in post-processing with the CREST code (Winner et al., 2019). CR electrons are evolved according to the Fokker–Planck equation on Lagrangian tracer particles while taking adiabatic changes and cooling via Coulomb losses, synchrotron emission, and IC processes into account. If tracer particles encounter the shock front, we model Fermi-I acceleration via injecting a fraction of the dissipated thermal energy into a momentum power-law spectrum with logarithmic slope  $\alpha_e$ . As a result, we obtain the CR proton energy density and the CR electron momentum spectrum at every time and at every point in our 3D simulation domain.

### 5.2.2 Magnetic Obliquity-Dependent Acceleration

The efficiency of proton acceleration, for quasi-parallel shocks (with magnetic field aligned close to the shock normal) can be up to 10 to 20 per cent of the initial shock kinetic energy, and the efficiency drops to zero for quasi-perpendicular shocks (Caprioli and Spitkovsky, 2014a), which is a consequence of the effective excitation of the non-resonant hybrid instability at quasi-parallel shocks that enables efficient CR proton acceleration (Caprioli and Spitkovsky, 2014b; Caprioli et al., 2015). We thus adopt an acceleration efficiency for CR protons that depends on the upstream magnetic obliquity  $\theta$ , the angle between the shock normal and the upstream magnetic field according to (Pais et al., 2018a)

$$\zeta_p(\theta) = \frac{\zeta_{p,\max}}{2} \left[ \tanh\left(\frac{\theta_{\text{crit}} - \theta}{\delta}\right) + 1 \right] \quad (5.1)$$

where  $\zeta_{p,\max} = 0.15$  is the efficiency in quasi-parallel configurations,  $\theta_{\text{crit}} = \pi/4$  the critical obliquity, and  $\delta = \pi/18$  the shape parameter. We define the acceleration efficiency as the ratio of accelerated CR energy density to the total shock-dissipated energy density,  $\zeta_{p,e} = \varepsilon_{\text{CRp,e}}/\varepsilon_{\text{diss}}$ .

Following the algorithm described in Winner et al. (2019), we inject a CR electron spectrum once a Lagrangian tracer particle crosses the shock and use the parametrized form of the 1D CR electron momentum spectrum (in units of particles per unit volume)

$$f_e(p_e, \theta) = C_e(\theta) p_e^{-\alpha_e} \Theta(p_e - p_{\text{inj}}) \times \left[ 1 + a \left( \frac{p_e}{p_{\text{cut}}} \right)^b \right]^c \exp\left[-\left(\frac{p_e}{p_{\text{cut}}}\right)^2\right], \quad (5.2)$$

where we adopt the parameters  $a = 0.66$ ,  $b = 2.5$ , and  $c = 1.8$  and treat the electron spectral index  $\alpha_e$  and the (normalized) cutoff momentum  $p_{\text{cut}}$  as free parameters that we vary in this work.

The normalisation  $C_e$  and injection momentum  $p_{\text{inj}}$  are calculated for every Lagrangian particle by attaching the non-thermal power-law spectrum to a thermal Maxwellian. We require that the energy moment of the distribution function equals the CR electron energy density,

$$\varepsilon_{\text{CRe}} = m_e c^2 \int_0^\infty f_e(p_e) \left[ \sqrt{1 + p_e^2} - 1 \right] dp_e, \quad (5.3)$$

which we compare to the dissipated energy density at the shock according to our specific model of obliquity dependent shock acceleration that we describe now.

The acceleration efficiency of CR electrons  $\zeta_e$  depends on the magnetic obliquity angle  $\theta$

$$\zeta_e(\theta) = \frac{\zeta_{e,\parallel} - \zeta_{e,\perp}}{2} \left[ \tanh\left(\frac{\theta_{\text{crit}} - \theta}{\delta}\right) + 1 \right] + \zeta_{e,\perp} \quad (5.4)$$

where  $\zeta_{e,\parallel}$  is the quasi-parallel acceleration efficiency for  $\theta = 0$  and  $\zeta_{e,\perp}$  is the quasi-perpendicular efficiency for  $\theta = \pi/2$  (i.e. for  $90^\circ$ ). Ab initio, the functional form of equation (5.4) is not known. Thus we explore three different models that are motivated by different lines of physics arguments and confront them to observational data.

One-dimensional (1D) particle-in-cell simulations of non-relativistic, high Mach number, *quasi-parallel* shocks (Park et al., 2015) find the onset of acceleration of non-thermal electrons and protons, in agreement with the predictions of the theory of diffusive shock acceleration. On the other hand, full particle-in-cell simulations show indications that electrons may be possibly even more efficiently accelerated at *quasi-perpendicular*, high-Mach number shocks (Riquelme and Spitkovsky, 2011; Bohdan et al., 2017; Xu et al., 2019). The electron acceleration efficiency is 0.1 by energy relative to the downstream thermal electrons (Xu et al., 2019), which have a fraction of 0.1 of the energy of the downstream thermal protons (Spitkovsky, private comm.). Combining this, we obtain an overall acceleration efficiency relative to the dissipated energy of about  $\varepsilon_{\text{CRe}}/\varepsilon_{\text{diss}} \approx 10^{-2}$  for *quasi-perpendicular* strong shocks. By contrast, the electron acceleration efficiency of *quasi-parallel* strong shocks is  $\varepsilon_{\text{CRe}}/\varepsilon_{\text{diss}} \lesssim 10^{-3}$  (Park et al., 2015; Xu et al., 2019).

This motivates our *quasi-perpendicular acceleration model*, for which we assume  $\zeta_{e,\perp} = 10\zeta_{e,\parallel}$ . This would be the correct model provided we can extrapolate the short simulation time of physical seconds to the SNR live time of more than 1000 years and provided there are no multi-dimensional effects that interfere with the extrapolations of these 1D particle-in-cell simulations. We contrast this model with two alternative models: in our *quasi-parallel acceleration model*, we assume  $\zeta_{e,\parallel} = 10\zeta_{e,\perp}$  and in a third model we adopt a *constant acceleration efficiency*,  $\zeta_e(\theta) = \zeta_{e,\text{max}}$ .

The maximum acceleration efficiency of CR electrons  $\zeta_{e,\text{max}} = \max(\zeta_{e,\parallel}, \zeta_{e,\perp})$  is a free parameter which is set such that a spectral fit to radio data is obtained. We obtain values of  $\zeta_{e,\text{max}} < 10^{-3}$  which reflect that the ratio of electron-to-proton acceleration efficiency is  $\zeta_{e,\text{max}}/\zeta_{p,\text{max}} < 10^{-2}$  (Schlickeiser, 2002; Zweibel, 2013). The obliquity dependency of quasi-parallel, constant, and quasi-perpendicular acceleration models are shown in Figure 5.1.

### 5.2.3 Initial Conditions

In order to model the remnant of the Type Ia SN 1006, we inject  $10^{51}$  erg of thermal energy into the central cell of a periodic 3D box with 22 pc length. We use two setups, the first with a resolution of  $10^6$  cells for parameter space studies and the second with a high resolution of  $5 \times 10^6$  cells for morphological studies. The cells are distributed in five shells around the centre and the average cell density per box length decreases from the first to the last shell as shown in Table 5.1. The centres of the cells are then perturbed by 10 per cent of the local average cell length before we relax the mesh via Lloyd's algorithm (Lloyd, 1982) in order to obtain glass-like configurations. We chose a higher cell density in the centre of our simulation box because of the fast initial adiabatic expansion of this central region. Tracer particles are initially sampled on positions of the cell centres except for a

Table 5.1: Resolution per box length (22 pc) in shells from the centre. The low resolution contains  $10^6$  cells and the high resolution  $5 \times 10^6$  cells.

radius $r$ (pc)	low resolution	high resolution
3.1	300	300
6.2	200	250
9.3	100	200
12.4	75	150
15.6	50	100

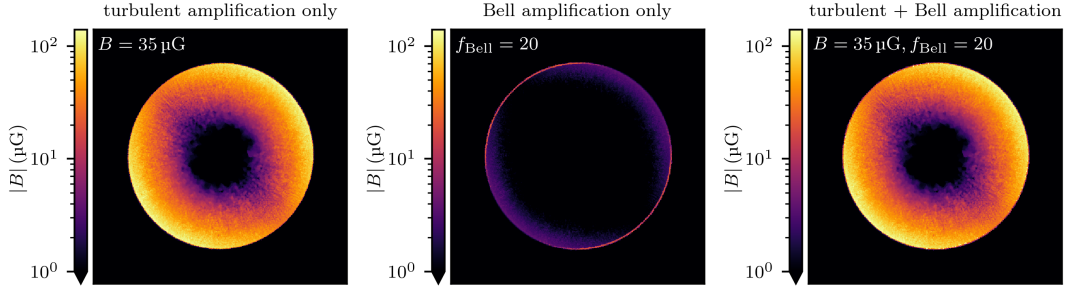


Figure 5.2: Magnetic field morphology in a slice through the centre of our simulated remnant. The left-hand panel shows the magnetic field strength for turbulent amplification only, the central panel shows the effect of Bell amplification only, and the right-hand panel shows the magnetic field strength as result of both, turbulent and Bell amplification. The maps have a side length of 21 pc or  $42.5'$  at a distance of 1660 pc.

small exclusion region within a radius 0.55 pc around the centre due to high numerical noise before the shock has developed numerically over a few cells.

As initial conditions, we adopt a gas number density of  $n = 0.12 \text{ cm}^{-3}$ , a mean molecular weight of  $\mu = 1.25$ , and temperature of  $T = 5.1 \times 10^3 \text{ K}$ . The initial magnetic field is oriented along the diagonal of the plane of the sky and has an absolute value of  $B = 1 \mu\text{G}$ . This setup leads to an energy driven, spherical shock wave driving into a homogeneous medium. We ignore the free expansion phase of the remnant as it's influence onto the final radius is smaller than 10 per cent (Pais et al., 2018b).

### 5.2.4 Magnetic Modelling

The magnetic field in the simulation is affected by three physical processes. First, the adiabatic compression at the shock enhances the magnetic field. However, only the component perpendicular to the shock normal is amplified by a factor  $n_{\text{post}}/n_{\text{pre}}$  where  $n_{\text{pre}}$  and  $n_{\text{post}}$  are the pre- and post-shock gas densities, respectively.

Secondly, we model the effect of a turbulent dynamo that is generated as a result of the interaction between pre-shock turbulence, clumping and the shock (Ji et al., 2016) which leads to high post-shock fields. Throughout our work, we multiply the magnetic field of our MHD solution inside the SNR and behind the shock front by an amplification factor and refer to an equivalent magnetic field strength instead of the amplified field (which differs for quasi-parallel and -perpendicular shock morphologies). Hence, a field of  $B = 35 \mu\text{G}$  is equivalent to a turbulent amplification of the post-shock fields by a factor of 35 for the parallel shock configuration and reaches a field strength of  $140 \mu\text{G}$  for the perpendicular shock configuration in the equatorial region.

Thirdly, we employ the amplification of magnetic fields via the non-resonant hybrid instability which is driven by the CR proton current in the pre-shock region (Bell, 2004). This so called Bell amplification drives strong perpendicular magnetic fields that are responsible for the efficient acceleration of CR protons (and possibly also CR electrons) in the quasi-parallel regime. We compute a cell-averaged value of the amplified field with

$$|B_{\text{amp}}| = |B| \left( \frac{f_{\text{Bell}} - 1}{2} \left[ \tanh\left(\frac{\theta_{\text{crit}} - \theta}{\delta}\right) + 1 \right] + 1 \right) \quad (5.5)$$

which follows the obliquity dependency of CR proton acceleration. We parametrize the Bell amplification by an amplification factor  $f_{\text{Bell}}$  which can reach values of about 30 (Bell, 2004).

We note that both amplification processes hardly overlap as the Bell amplified fields are quickly damped in the post-shock region whereas the turbulently amplified magnetic field starts to build up in the post-shock region as the small-scale dynamo emerges but saturates only after a finite time and distance from the shock.

Figure 5.2 shows the resulting magnetic morphology in a slice through the centre of our simulated remnant. In the left-hand panel, the magnetic field is only amplified by the turbulent dynamo (and by adiabatic compression) to values of  $B = 35$  to  $140 \mu\text{G}$  for quasi-parallel and -perpendicular geometries, respectively. The shock front encounters small-scale density inhomogeneities which inject vorticity according to Crocco's theorem (1937) that leads to a turbulent cascade and a small-scale dynamo, which amplifies the post-shock magnetic field. This process saturates if the magnetic energy density reaches about 10 per cent of the kinetic energy density in the post shock medium (Schekochihin et al., 2004; Cho et al., 2009; Kim and Ostriker, 2015; Federrath, 2016). In the post-shock rest frame, the velocity of the post-shock medium is  $v = 3/4v_s$  with a shock velocity of  $v_s \approx 3000 \text{ km/s}$  at 1000 years. Hence the maximum possible value of the turbulently amplified magnetic field (neglecting adiabatic cooling) is given by

$$B_{\text{max,turb}} \approx \sqrt{0.1 \times 8\pi \frac{4\mu m_p n}{2} \left(\frac{3}{4}v_s\right)^2} \approx 250 \mu\text{G}, \quad (5.6)$$

where  $n = 0.12 \text{ cm}^{-3}$  is the pre-shock density. This is larger than the  $140 \mu\text{G}$  field that our best-fit model requires in the quasi-perpendicular regions. In the quasi-parallel regions,

a lower magnetic field of  $35 \mu\text{G}$  is realised as the turbulent dynamo acts on magnetic seed values that are four times smaller due to the absence of adiabatic compression for the parallel field geometry, but saturates at the same time as for the quasi-perpendicular regions. Thus, our magnetic field strengths in the remnant are overall in agreement with values of  $90 \mu\text{G}$  inferred from the analysis of X-ray filaments in the NE of SN 1006 (Morlino et al., 2010).

In the central panel of Figure 5.2, we show the magnetic morphology for Bell amplification only. Bell amplification scales with the magnetic obliquity due to obliquity dependent acceleration of CR protons as shown in Equation (5.6) such that it steeply declines towards quasi-perpendicular regions. Due to its small spatial extent at the shock front, the Bell amplified magnetic field barely influences the cooling of the CR electron spectrum. Note that the field strengths of approximately  $4 \mu\text{G}$  in the quasi-perpendicular regions are solely due to adiabatic compression.

The right-hand panel of Figure 5.2 shows the magnetic field as a result of both amplification processes. As explained before, the magnetic field is dominated by the turbulent amplification and the Bell-amplified field plays a minor role for the overall magnetic morphology.

### 5.2.5 Non-Thermal Radiative Transfer

Non-thermal synchrotron and IC emission is calculated from the simulated CR electron spectra. We assume an isotropic distribution of pitch angles for synchrotron emission and follow the analytic approximation by Aharonian et al. (2010). For the IC emission, we include the Klein-Nishina cross section (Blumenthal and Gould, 1970). In contrast to CR electrons, the simulations evolve only the energy density of CR protons  $\varepsilon_{\text{CRp}}$ . In order to calculate hadronic  $\gamma$ -ray emission, we calculate a 1D CR proton spectrum of the form

$$f_p(p_p) = C p_p^{-\alpha_p} \Theta(p_p - q) \exp \left[ - \left( \frac{p_p}{p_{\text{max}}} \right)^2 \right], \quad (5.7)$$

where  $\alpha_p$  is the logarithmic momentum slope,  $q = 0.5$  is the minimum momentum, and  $p_{\text{max}} = 2.1 \times 10^5$  is the (normalized) maximum momentum. The normalisation  $C$  is calculated for every cell such that the energy moment of the distribution function equals the proton energy density,  $\varepsilon_{\text{CRp}} = m_p c^2 \int f_p(p_p) [(1 + p_p^2)^{1/2} - 1] dp_p$ . Hadronic gamma ray emission is then obtained with parametrizations of the cross-section of neutral pion production at low ( $E_{p,\text{kin}} < 10 \text{ GeV}$ ) and high proton energies (Yang et al. 2018; Kafexhiu et al. 2014, Werhahn et al. in prep.).

The synthetic noise map is based on the noise power spectrum of the excess map of SN 1006. To detect the noise, we exclude the emission from the NE and SW lobes masking the original excess map from Acero et al. (2010) with a sharp cutoff calculated taking the absolute value of the minimum of the excess counts. The power spectrum of SN 1006 is obtained via a 2D Fourier transform of the masked dataset. We fit the power spectrum

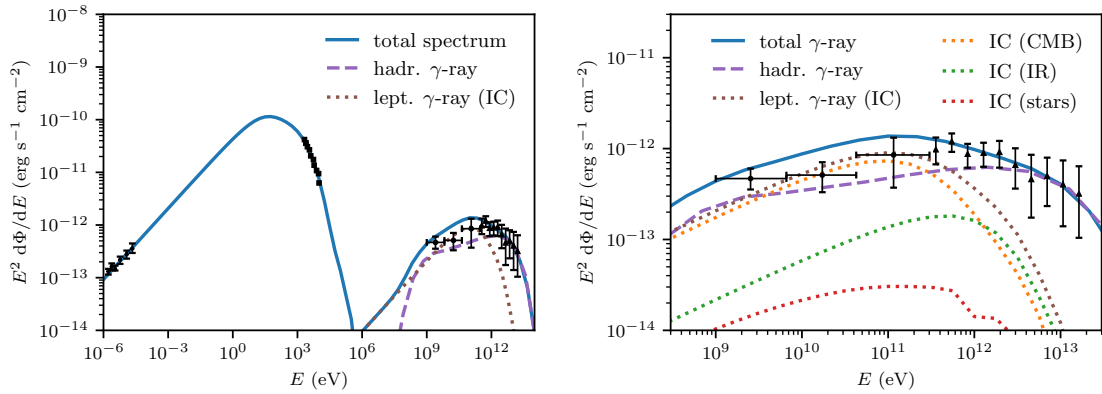


Figure 5.3: Best-fit multi-frequency spectrum of SN 1006. The CR spectra have spectral indices of  $\alpha_e = 2.1$  for electrons and  $\alpha_p = 1.9$  for protons. Important parameters are gas density of  $n = 0.12 \text{ cm}^{-3}$ , distance of  $D = 1660 \text{ pc}$ , equivalent magnetic field of  $B = 35 \mu\text{G}$  (as a result of a turbulent dynamo), and Bell amplification by a factor of 20. The simulated spectrum is compared with observational data in radio (Reynolds, 1996), X-rays (Bamba et al., 2008), and in  $\gamma$ -rays from *Fermi* (Abdo et al., 2010) and HESS (Acero et al., 2010) (sum of two regions).

with the following function in  $k$ -space

$$P(k) = A \exp\left(-\frac{k^2}{2\sigma^2}\right) + Bk^{-2} \quad (5.8)$$

where  $\sigma_k$  is the standard deviation in  $k$ -space and the variables  $A$  and  $B$  determine the relative strength of the Gaussian and the power-law tail. The fitted power spectrum is converted into a real noise map via 2D inverse Fourier transform and added in postprocessing to the previously PSF-convolved simulation map.

## 5.3 Leptonic versus Hadronic Model

In this section, we present our best-fit simulation together with its multi-frequency spectrum and maps of radio, X-ray, and  $\gamma$ -ray surface brightness. We compare these to observations and discuss whether leptonic or hadronic emission is dominating in the high energy  $\gamma$ -ray regime.

### 5.3.1 Multi-Frequency Spectrum

In Figure 5.3, we present the multi-frequency spectrum of our best-fit simulation. The simulation uses a homogeneous gas density of  $n = 0.12 \text{ cm}^{-3}$ , an equivalent magnetic

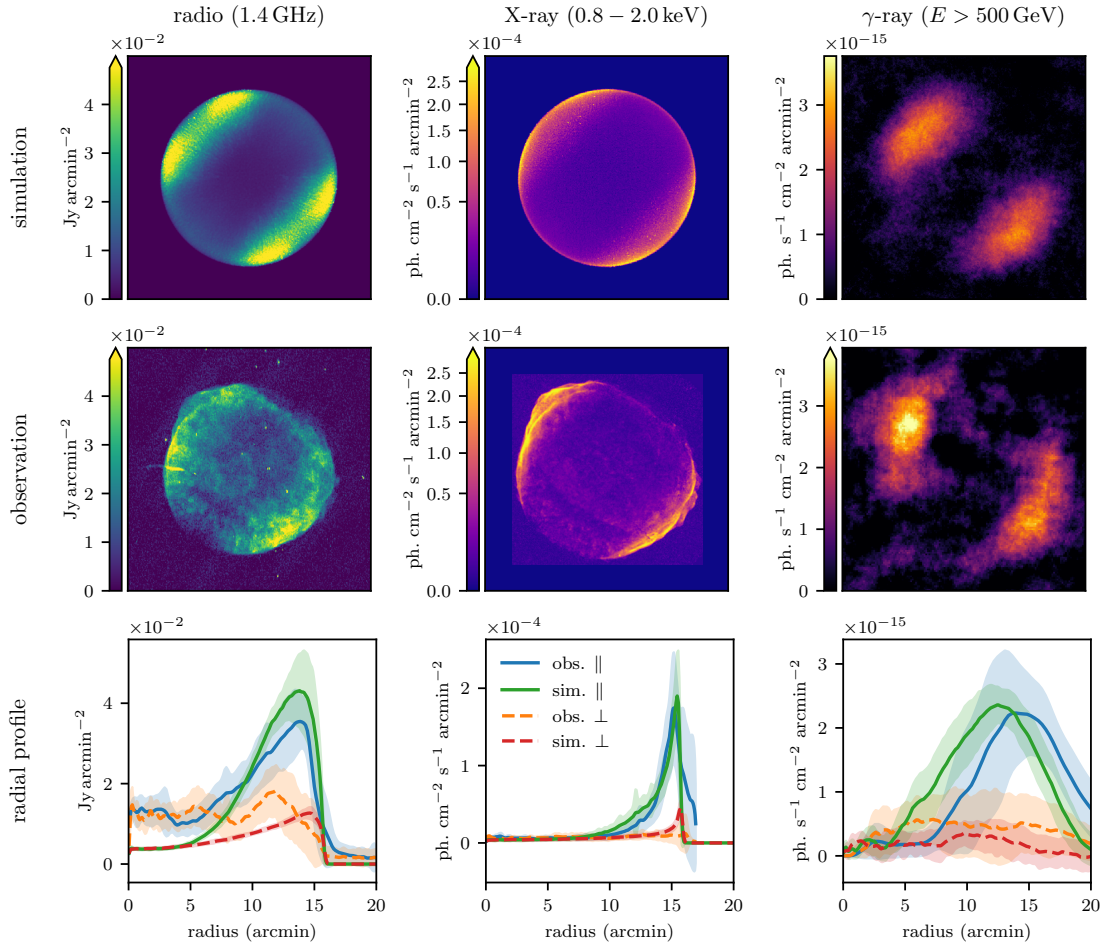


Figure 5.4: Morphological comparison of our best-fit simulation with preferred *quasi-parallel acceleration* to 1.4 GHz radio data (Dyer et al., 2009) (left column), to 2 keV to 4.5 keV X-ray data (Cassam-Chenai et al., 2008) (middle column), and to HESS  $\gamma$ -ray data above 500 GeV (Acero et al., 2010) (right column). The top row shows our simulated maps and in the middle row observations are presented. In the bottom row, we show radial profiles for data in sectors with opening angle of  $\pi/3$  aligned parallel and perpendicular to the magnetic field. Our simulated  $\gamma$ -ray map is convolved with a 2D Gaussian profile with  $\sigma = 0.042^\circ$  similar to the HESS PSF and contains Gaussian noise with the observed amplitude and correlation structure (as quantified through the power spectrum where we cut the signal regions). The maps have a side length of 21 pc or  $42.5'$  at a distance of 1660 pc.

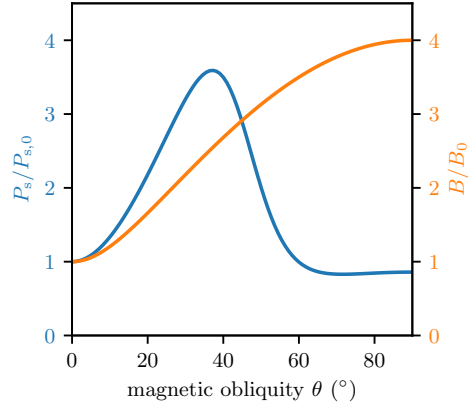


Figure 5.5: Angular dependency of synchrotron emission (blue) and adiabatically compressed magnetic field (orange) relative to their values at  $0^\circ$  for our best-fit quasi-parallel acceleration model.

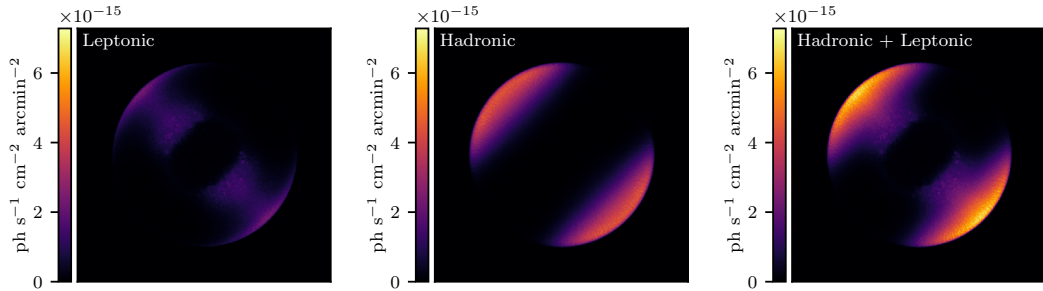


Figure 5.6:  $\gamma$ -ray maps ( $E > 500$  GeV) of our best-fit quasi-parallel acceleration model. We compare the leptonic IC emission (left), the hadronic pion-decay emission (middle) and the total  $\gamma$ -ray emission (right), which is dominated by the hadronic component. The maps have a side length of 21 pc or  $42.5'$  at a distance of 1660 pc.

field of  $B = 35 \mu\text{G}$ , a Bell amplification by the factor 20 at the shock front, a CR electron spectral index of  $\alpha_e = 2.1$ , and a maximum CR electron acceleration momentum of  $p_{\text{cut}} = 3.5 \times 10^7$ . In our best-fit model, CR electron acceleration is most efficient in quasi-parallel configurations. We discuss how variations of these parameters or prescriptions impact the spectrum or the emission morphologies in Sections 5.4 to 5.6.

The radius of our simulated remnant and the observed angular size of  $0.5'$  yields a distance to the remnant of  $D = 1660 \text{ pc}$ . We leave the electron acceleration efficiency  $\zeta_{e,\text{max}}$  as a free parameter in order to fit the observed radio data. The spectrum fits the data very well with an acceleration efficiency of  $\zeta_{e,\text{max}} = 5 \times 10^{-4}$ . The synchrotron spectrum has a spectral index of  $\alpha_s = (\alpha_e - 1)/2 = 0.55$  up to photon energies of  $E \approx 10 \text{ eV}$ . At larger photon energies the synchrotron spectrum is sensible to the cooling of the underlying CR electron spectrum and its cutoff. The dominant electron momentum<sup>1</sup> for emission at synchrotron frequency  $\nu_s$  is

$$p_e \approx 5 \times 10^3 \left( \frac{\nu_s}{1 \text{ GHz}} \right)^{1/2} \left( \frac{B}{5 \mu\text{G}} \right)^{-1/2}. \quad (5.9)$$

Hence, the dominant momentum for 1 keV X-rays at  $35 \mu\text{G}$  is  $p_e \approx 3 \times 10^7$  which is close to the maximal electron acceleration momentum. This explains the synchrotron cutoff at X-ray energies.

At even larger photon energies, in the GeV to TeV  $\gamma$ -ray range, the photon spectrum is a combination of leptonic emission from IC and hadronic  $\gamma$ -ray emission from CR protons interacting with the ambient gas. We assume that the IC emission results from CRe interactions with three black-body photon fields: the cosmic microwave background (CMB), an infrared field with  $T_{\text{IR}} = 30 \text{ K}$ , and a star light photon field  $T_{\text{star}} = 4100 \text{ K}$  (see Section 5.6 for details of the adopted radiation fields). Leptonic emission is dominating over hadronic emission at *Fermi*  $\gamma$ -ray energies from 1 to 100 GeV. For photon energies larger than 100 GeV, the IC spectrum falls off as it is influenced by the maximal momentum of the underlying CR electrons. Hadronic  $\gamma$ -ray emission is therefore dominating at very-high  $\gamma$ -ray energies observed by the High Energy Stereoscopic System (HESS).

### 5.3.2 Non-Thermal Emission Morphologies

In Figure 5.4, we compare simulated and observed morphology of SN 1006. We present three simulated surface brightness maps of radio, X-ray, and  $\gamma$ -ray emission (top row) together with the corresponding images from observations (middle row). Observational images are rescaled such that the integrated surface brightness corresponds to the spectral data. In addition, we show radial profiles for regions quasi-parallel and quasi-perpendicular to the magnetic field (bottom row). Radial profiles are created by selecting sectors of size

<sup>1</sup>We obtain this formula by replacing the kernel  $F(E/E_c)$  in the synchrotron emissivity by Dirac's  $\delta$  distribution at its expectation value  $E/E_c = 4\pi m_e c v / (3eB) \approx 2.13$ , e.g. see equation (D1) in Aharonian et al. (2010).

$\pi/3$  around the magnetic field vector (NE to SW direction) and around the perpendicular vector to the magnetic field in the plane of the sky (SE to NW direction).

Our simulated radio map (top left panel of Figure 5.4) matches well the observed map of SN 1006 (mid left panel). It is a combination of single dish observations with the Green Bank Telescope and interferometric observations with the Very Large Array at 1.4 GHz (Dyer et al., 2009). The map shows bright polar caps in the NE and SW direction and regions of low surface brightness in the centre, the NW and SE direction.<sup>2</sup> The polar caps are bright due the efficient acceleration of CR electrons in these regions with quasi-parallel shock acceleration. Regions with low surface brightness are characterised by an acceleration efficiency of CR electrons that is smaller by a factor of 10 (see Figure 5.1) due to the quasi-perpendicular shock morphology.

This comparison is quantified through the radial profiles for the quasi-parallel and quasi-perpendicular regions (bottom left panel), demonstrating a very good agreement except for the central regions which show a slightly elevated emission in the observations. After acceleration at the shock, the CR electrons are advected downstream, cool adiabatically and suffer radiation losses so that the central region of the remnant experiences low radio synchrotron surface brightness. Our simulations do not explicitly account for a turbulent dynamo and may thus underestimate the level of magnetic fluctuations inside the SNR. There may even be reacceleration of CR electrons at magnetic reconnection sites or by interacting with the MHD turbulence that counteracts some of the CR electron cooling processes.

Each polar cap shows two bright spots at an angle of  $\theta \approx 35^\circ$  that exceed the emission at the parallel orientation of  $\theta \approx 0^\circ$ . The reason for this is a competition of two effects that have different azimuthal dependencies. At quasi-perpendicular shock morphologies, the ambient magnetic field is adiabatically compressed by a factor of four at the shock front and remains unaltered at quasi-parallel shock morphologies. Our quasi-parallel acceleration efficiency (see equation 5.4) shows the opposite behaviour and peaks at quasi-parallel morphologies. It turns out that the adiabatic magnetic field amplification increases faster with the increasing obliquity angle than the acceleration efficiency decreases, which results in the particular azimuthal behaviour of the radio surface brightness that is shown in Figure 5.5.

We draw similar conclusions from the comparison between observation and simulation of the X-ray surface brightness map (central column of Figure 5.4) for 0.8 keV to 2 keV photons. The simulated X-ray map (top central panel) has a similar morphology in comparison to the simulated radio map. Polar caps are visible which are a consequence of the efficient acceleration of CR electrons in quasi-parallel regions where the magnetic field is parallel to the shock normal. The emission in the polar caps also peaks at around an angle of  $\theta \approx 35^\circ$  away from the magnetic field axis. Regions where the magnetic field is perpendicular to the shock normal have a lower surface brightness.

The simulated X-ray map shows rims contrary to the simulated radio map where the

---

<sup>2</sup>The bright elongated source in the eastern rim is a background radio galaxy (Cassam-Chenai et al., 2008).

emitting regions shows a larger extend towards the centre. This is because the CR electron momentum that emits X-ray synchrotron emission (see equation 5.9) is close to the maximum acceleration momentum  $p_{\text{cut}} = 3.5 \times 10^7$ . These CR electrons cool fast by means of synchrotron emission in strong magnetic fields and by adiabatic expansion as the SNR expands. Therefore, the spectrum at electron momenta relevant for X-ray emission plummets towards the centre. Strong non-thermal X-ray emission is therefore only present at the shock front where CR electrons are freshly accelerated to the X-ray synchrotron emitting momentum. The simulated X-ray map matches the observed X-ray map (middle centre panel of Figure 5.4) which is processed from *Chandra* observations (Cassam-Chenaï et al., 2008). The radial profiles (bottom centre panel) show again excellent agreement between simulation and observation in quasi-parallel and quasi-perpendicular regions.

In the right column, we compare simulation and observation in the  $\gamma$ -ray band above  $E_\gamma > 500$  GeV. The simulated  $\gamma$ -ray map (top right panel of Figure 5.4) is a sum of leptonic and hadronic  $\gamma$ -ray emission. The map is convolved with a 2D Gaussian profile with  $\sigma = 0.042^\circ$  similar to the HESS point spread function (PSF).<sup>3</sup> In addition, we add Gaussian noise with the observed amplitude and correlation structure (as quantified through the power spectrum where we cut the signal regions). The map shows two bright, elongated emission regions tracing out a quasi-parallel shock morphology. These regions spatially coincide with those in the radio and X-ray. However, no emission is visible in the centre and in the quasi-perpendicular regions in contrast to the radio and X-ray maps. The morphology of the simulated  $\gamma$ -ray map matches that of the observed map (middle right panel of Figure 5.4). Observations were made with HESS and analysed by Acero et al. (2010). The radial profiles (bottom right panel) show very good agreement between our simulation and the observation.

In Figure 5.6, we show the  $\gamma$ -ray maps of leptonic and hadronic emission as well as the sum of both processes. Leptonic emission (left panel) results from IC interactions with three photon fields, of which the IC emission from CMB photons is dominant. IC emission produces thin rims in the quasi-parallel regions where the CR electron efficiency is at its maximum. There are tails of IC emission parallel to the magnetic field towards the centre because the CR electron spectrum is less affected by synchrotron cooling in comparison to the regions of larger obliquity angles where the magnetic field is compressed adiabatically. In our model, quasi-perpendicular regions do not shine via IC emission as the CR electron acceleration efficiency there is lower by a factor of 0.1 in comparison to the quasi-parallel region.

Hadronic emission (centre panel of Figure 5.6) is calculated from the decay of neutral pions resulting from the interaction of CR protons with the protons of the gas. CR protons are accelerated efficiently in quasi-parallel regions whereas the efficiency drops to zero for quasi-perpendicular regions. Therefore, hadronic processes produce extended, bright polar caps in  $\gamma$ -rays. There is no hadronic  $\gamma$ -ray emission towards the centre as CR protons

<sup>3</sup>The HESS PSF has a 68 per cent containment radius of  $R_{68} = 0.064^\circ$  (Acero et al., 2010). This corresponds to  $\sigma \approx R_{68}/1.515$  for a 2D Gaussian profile (Stycz, 2016).

cool adiabatically and the target gas density is decreasing as a power law in radius.

## 5.4 Obliquity-Dependent Acceleration

In the previous section, we have presented a simulation with preferred quasi-parallel electron acceleration which matches the multi-frequency spectrum and the morphology of SN 1006. Because there is still an ongoing debate whether CR electrons can be efficiently accelerated in quasi-perpendicular or quasi-parallel configurations, we show that alternative acceleration scenarios are not able to reproduce the observed morphology. In the following, we critically compare our quasi-parallel acceleration model to simulations with constant, i.e. obliquity independent, and preferred quasi-perpendicular acceleration of CR electrons. However, in all cases, CR protons are accelerated in quasi-parallel configurations (Caprioli and Spitkovsky, 2014a). For reference, the obliquity dependent acceleration efficiencies are presented in Figure 5.1.

### 5.4.1 Quasi-Parallel Acceleration Efficiency

As explained in Section 5.3, Figures 5.3 and 5.4 show the total multi-frequency spectrum and the emission maps of SN 1006 and demonstrate that overall this model provides a very good quantitative match to the observations while there are differences in detail. We expect that the inclusion of more realism in the simulations will also model these small-scale feature. In particular, including density fluctuations and small-scale interstellar turbulence so that the interaction with the shock produces a turbulent dynamo and magnetic field fluctuations may produce the observed patchy radio morphology and ripples in the shock surface. This could then explain the appearance of several shocks in projection in the X-ray surface brightness map. The same effect may then also slightly reduce the IC flux and improve the fit in the *Fermi* band. Finally the asymmetry of the elongated  $\gamma$ -ray emitting regions being brighter in the North and dimmer in the South could originate from a large-scale gradient that boosts the hadronic pion-decay flux relative to the Southern counterpart (Pais & Pfrommer in prep.).

### 5.4.2 Constant Acceleration Efficiency

Figure 5.7 shows the non-thermal emission maps of the simulation with constant acceleration efficiency (top row), observations (mid row), and radial profiles (bottom row) in the radio (1.4 GHz), X-ray (0.8 keV to 2 keV), and  $\gamma$ -ray band ( $E > 500$  GeV). The simulation with constant acceleration efficiency uses the same parameters as before with one exception: to fit the multi-frequency spectrum to the radio data points, we need to adopt an electron acceleration efficiency of  $\zeta_{e,\max} = 2 \times 10^{-4}$ . It is apparent that the simulated radio and X-ray surface brightness maps have bright regions in the SE and NW which do not match those of the observations. Radial profiles illustrate this mismatch. On the

## 5.4. OBLIQUITY-DEPENDENT ACCELERATION

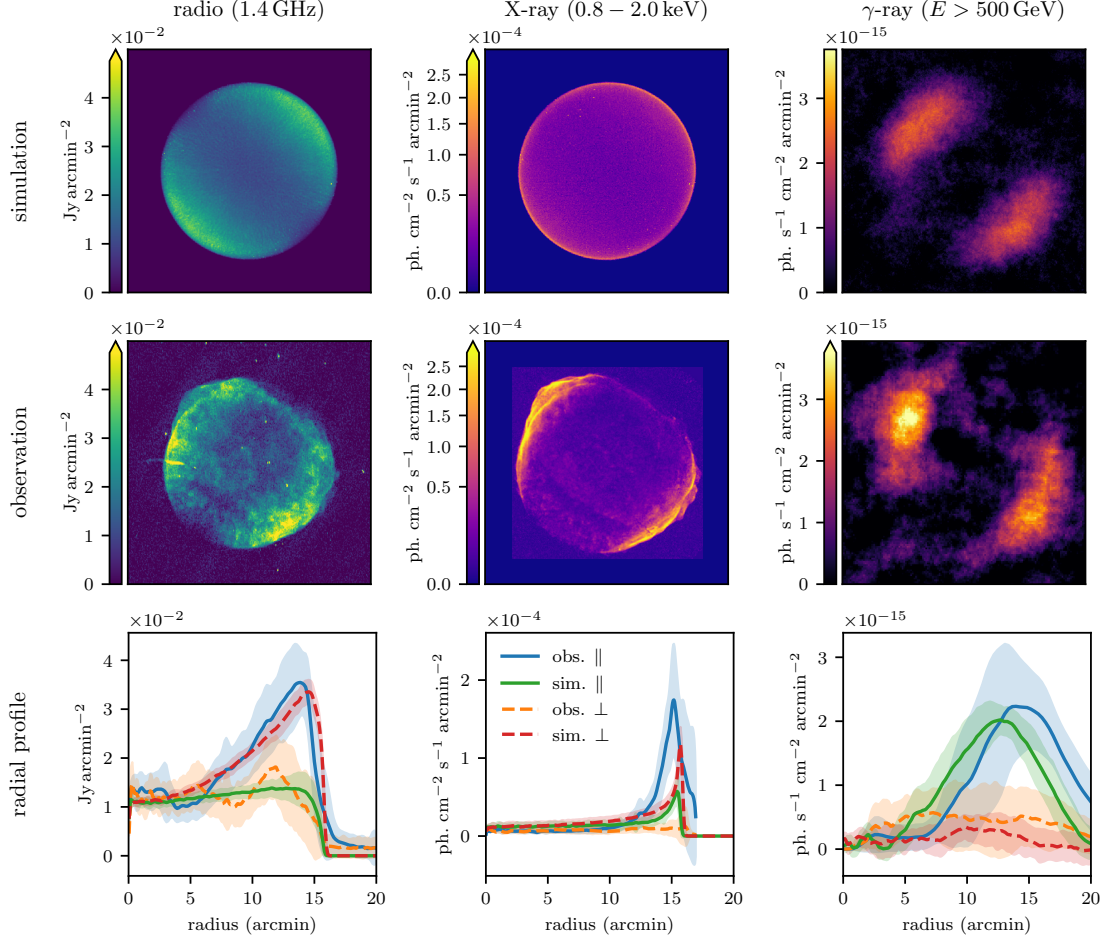


Figure 5.7: Morphological comparison of our simulation with a *constant, i.e. obliquity independent, acceleration*; details as in Figure 5.4. The leptonic synchrotron emission in the radio and X-rays does not match the observations in these bands (Dyer et al., 2009; Cassam-Chenaï et al., 2008). The simulated  $\gamma$ -ray map is dominated by the hadronic emission and in agreement with HESS observations (Acero et al., 2010). The maps have a side length of 21 pc or  $42.5'$  at a distance of 1660 pc.

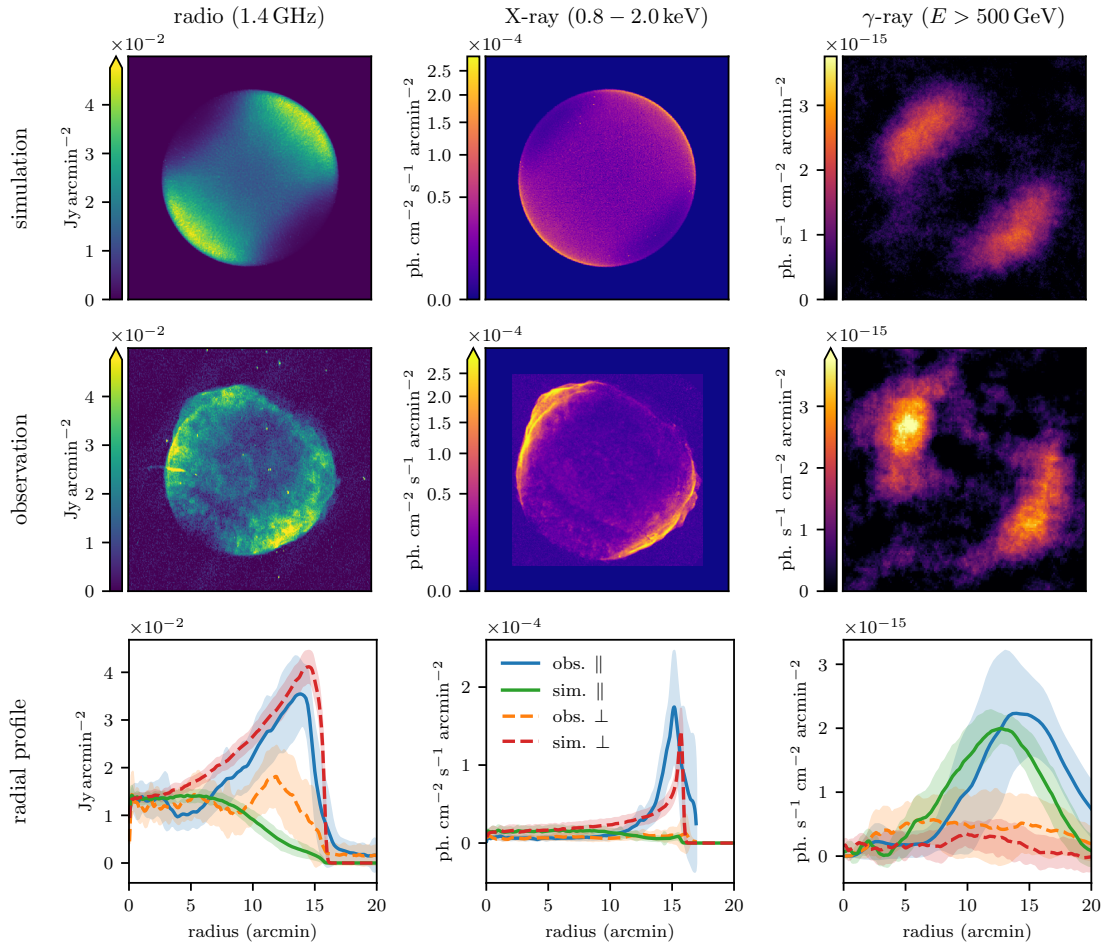


Figure 5.8: Morphology of the simulations with preferred *quasi-perpendicular acceleration* efficiency of CR electrons; details as in Figure 5.4. The leptonic synchrotron emission in the radio and X-rays does not match the observations in these bands (Dyer et al., 2009; Cassam-Chenaï et al., 2008). The simulated  $\gamma$ -ray map is dominated by the hadronic emission and in agreement with HESS observations (Acero et al., 2010). The maps have a side length of 21 pc or  $42.5'$  at a distance of 1660 pc.

contrary, the simulated  $\gamma$ -ray surface brightness map is in agreement with observation as the emission is dominated by CR protons which are accelerated at quasi-parallel configurations. A rotation of the magnetic field by  $90^\circ$  in the plane of sky cannot resolve the mismatch in radio and X-ray as it would lead to a mismatch in the  $\gamma$ -ray maps.

### 5.4.3 Quasi-Perpendicular Acceleration Efficiency

Figure 5.8 shows the non-thermal emission maps of the simulation with quasi-perpendicular acceleration (top row), observations (mid row) and radial profiles (bottom row). The simulation with quasi-perpendicular acceleration efficiency uses the same parameters as before with one exception: to fit the multi-frequency spectrum to the radio data points, we need to adopt an electron acceleration efficiency of  $\zeta_{e,\max} = 2 \times 10^{-4}$ . This acceleration scenario again leads to bright radio and X-ray regions in the SE and NW which are in disagreement with observations. However, there is an agreement for the  $\gamma$ -ray maps which are dominated by hadronic emission.

These two alternative obliquity dependencies for CR electron acceleration, i.e. constant and quasi-perpendicular, cannot reproduce the observed morphologies of SN 1006. This favours the preferred quasi-parallel acceleration of CR electrons.

## 5.5 Amplification and Damping of Magnetic Fields

In this section, we demonstrate the case for volume-filling strong magnetic fields, potentially amplified by a turbulent dynamo, in order not to overproduce the  $\gamma$ -ray data points. In addition to these volume-filling magnetic fields in the post shock region, we model the amplification of magnetic fields via the non-resonant hybrid instability driven by CR protons in the upstream region close to the shock. These amplified magnetic fields decay due to strong ion-neutral collisional damping. In this section, we explain the influence of these fields and draw phenomenological conclusions on their damping length scale.

### 5.5.1 Turbulent Magnetic Amplification

As shown in Section 5.3, we obtain good agreement of the simulated multi-frequency spectrum with observations if there is a volume-filling amplified magnetic field (turbulently amplified fields) with an equivalent strength of  $B = 35 \mu\text{G}$  and if the field is additionally amplified on a short range by a factor of 20 directly at the shock via the non-resonant hybrid instability (Bell-amplified fields). In order to distinguish between the observational signatures of the different amplification processes, we first show simulations without any (volume-filling) turbulently amplified magnetic fields and present simulations in which the Bell-amplified magnetic fields persist on a long range, i.e. they decay adiabatically with  $B = (n/n_s)B_{\text{amp}}$  because the amplified Alfvén wave field is purely transverse to background magnetic field (and as such to the shock normal for parallel shocks). Here,

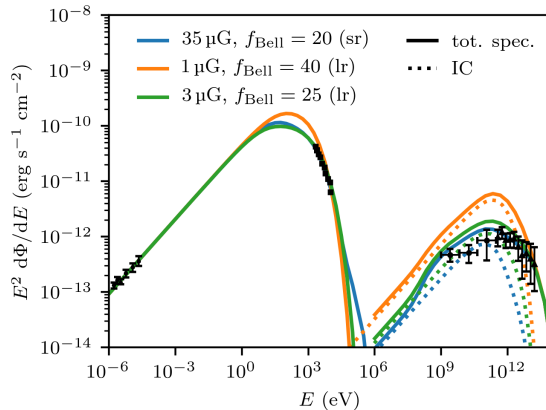


Figure 5.9: Multi-frequency spectra of models with short-range (sr) and long-range (lr) Bell-amplified magnetic fields. The spectrum in the  $\gamma$ -ray regime is a sum of IC emission (dotted) and hadronic  $\gamma$ -rays (not shown). The blue lines represent our best-fit model with volume-filling field (as result of a turbulent dynamo) and short range Bell-amplified fields. Orange and green lines represent models with typical ISM magnetic fields with long-range Bell-amplified magnetic fields but without a volume-filling amplification by a turbulent dynamo.

$n$  denotes the current number density,  $n_s$  is the number density at the shock front,  $B_{\text{amp}}$  denotes the Bell-amplified magnetic field at the shock.

Figure 5.9 compares the multi-frequency spectra of our best-fit (blue lines) to models with long-range Bell-amplified magnetic fields (orange and green lines). The models with long-range magnetic fields include typical values of the large-scale ISM magnetic field. A long-range Bell amplification by a factor  $f_{\text{Bell}} = 40$  together with an ISM field of  $1 \mu\text{G}$  (orange lines) leads to an overproduction of  $\gamma$ -ray emission as a large CR electron acceleration efficiency of  $\zeta_{e,\text{max}} = 2.2 \times 10^{-3}$  is required in order to reproduce observational radio data. A larger ISM field of  $3 \mu\text{G}$  together with long-range Bell-amplified fields by a factor a factor  $f_{\text{Bell}} = 25$  has a lower  $\gamma$ -ray emission that is close to observational  $\gamma$ -ray data ( $\zeta_{e,\text{max}} = 8 \times 10^{-4}$ ).

Although this model with long-range Bell-amplified magnetic fields reproduces the observed multi-frequency spectrum fairly well it clearly fails to reproduce the observed morphology which is shown in Figure 5.10. As before, we show simulations (top row), observations (middle row), and radial profiles (bottom row) for the radio (left column), X-ray (central column), and  $\gamma$ -ray band (right column).

The simulated radio map (top left panel of Fig. 5.10) has two polar caps which are brighter and more confined in comparison to our best-fit simulation with short-range Bell-amplified magnetic fields in Figure 5.4. This is due to the sustained amplified magnetic fields which dramatically increase the synchrotron luminosity at radio frequencies. Although we chose an CR electron maximal acceleration efficiency to be  $\zeta_{e,\text{max}} = 8 \times 10^{-4}$

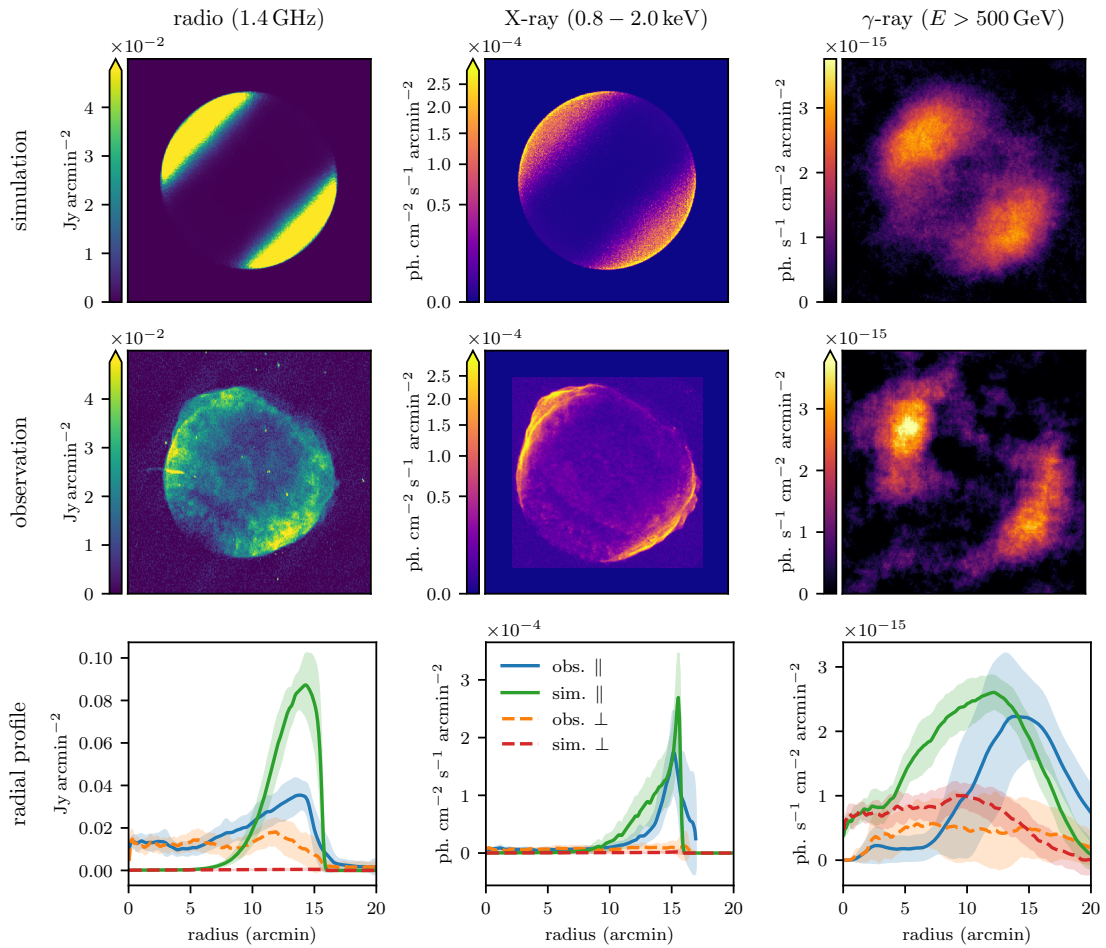


Figure 5.10: Morphology of simulations with a long-range Bell-amplified magnetic field that decays in proportion to the adiabatic expansion of the gas,  $B = B_{\text{amp}}n/n_{\text{shock}}$  (because of its transverse polarization). The radio, X-ray, and  $\gamma$ -ray morphologies are in disagreement with observations. The maps have a side length of 21 pc or  $42.5'$  at a distance of 1660 pc.

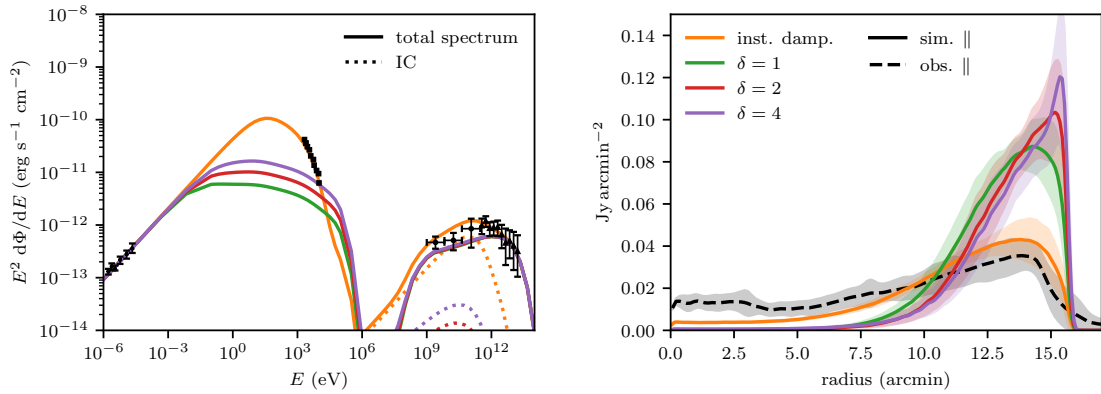


Figure 5.11: Multi-frequency spectra (left) and radial profiles of radio surface brightness maps (right) for different decay models of the Bell-amplified magnetic field via plasma effects. The model of instantaneous damping (orange solid) is our best-fit model and is in agreement with observations. Other models assume  $B = (n/n_{\text{shock}})^{\delta} B_{\text{amp}}$ .

such that the simulated spectrum fits the radio data, the radial profile (bottom left of Fig. 5.10) shows a clear mismatch to the radio observations. This is a consequence of the fast synchrotron cooling of CR electrons in the strong magnetic fields so that the central regions of the simulated remnant are devoid of radio emission.

The simulated X-ray map (top centre panel of Fig. 5.10) has a similar morphology in comparison to the simulated radio map. It shows bright polar caps that are significantly wider than the observed X-ray rims (mid centre panel). In addition, the simulated  $\gamma$ -ray map (right column) is in disagreement with observations and fill in the central parts of SN 1006 unlike the HESS observations. Leptonic  $\gamma$ -rays are contributing significantly to the emission at  $E \approx 500$  GeV because the small volume of the radio-emitting regions require a larger CR electron acceleration efficiency in comparison to our best-fit model with short-range Bell-amplified fields.

We therefore conclude that a volume-filling magnetic field, potentially amplified by a turbulent dynamo, is necessary in order to reproduce the observed multi-frequency spectrum and morphology.

### 5.5.2 Magnetic Amplification via the Bell Instability

As shown before, we obtain good agreement of the simulated multi-frequency spectrum with observations if magnetic fields are amplified by a factor of 20 directly at the shock and decay immediately behind it. To determine the sensitivity of the non-thermal emission maps on the phenomenological model of the magnetic field decay, we present simulations in which the amplified magnetic fields decay significantly slower and adopt a scaling with

the gas density according to

$$B = \left( \frac{n}{n_s} \right)^\delta B_{\text{amp}}, \quad (5.10)$$

where  $\delta$  is the damping parameter.

Figure 5.11 shows multi-frequency spectra (left) and radial profiles of the radio maps (right) for our best-fit model with instantaneous damping and three models with different decay parameters  $\delta$ . It is evident, that only the simulation with instantaneous damping of amplified magnetic fields shows good agreement with the observed multi-frequency spectrum and the radial profile. Larger decay parameters lead to an increasing X-ray and  $\gamma$ -ray emissivity because CR electrons suffer strong cooling losses on shorter timescales. However, these simulations significantly deviate from observed profiles.

We therefore conclude that amplified magnetic fields driven by CR proton current at the shock have to decay on a very short length scale close to our discretized Voronoi cell size at the shock (corresponding to 100 gyroradii for TeV particles) and cannot be sustained for a long time in the post shock region.

## 5.6 Parameter Dependencies

The multi-frequency spectrum is influenced by several parameters. We first study the dependence of the spectra on different CR proton and electron spectral indices. Secondly, we present spectra for varying equivalent magnetic field strengths (possibly as a result of turbulent amplification), Bell amplification factors, maximum acceleration momentum. Finally, we study the influence of ambient photon fields and gas densities.

### 5.6.1 Spectral Index of CRs

Figure 5.12 shows the total (solid lines) and hadronic (dashed lines) high energy  $\gamma$ -ray spectra for CR proton spectral indices of  $\alpha_p = 1.9, 2.0,$  and  $2.1$ . We use a maximum CR proton momentum of  $p_{\text{max}} = 2.1 \times 10^5$  for  $\alpha_p = 1.9$  and  $p_{\text{max}} = 4.2 \times 10^5$  for the latter two indices (see equation 5.7). We adopt our best-fit leptonic spectrum with a CR electron spectral index of  $\alpha_e = 1.9$  (see Figure 5.3) to calculate the total spectrum. The hadronic spectrum for  $\alpha_p = 1.9$  agrees best with the observed data, which is especially visible for the first *Fermi* data point (at  $\approx 3$  GeV) and for the HESS data points above 1 TeV. A steeper proton spectral index leads to an overestimate of the  $\gamma$ -ray flux at GeV energies and at the same time to an underestimate at TeV energies. Hence, we use the best fitting value of  $\alpha_p = 1.9$  for further analysis of the spectrum.

We show the influence of the CR electron spectral index  $\alpha_e$  in Figure 5.13. Other parameters such as the equivalent magnetic field of  $B = 35 \mu\text{G}$ , the amplification factor of 20, and the maximum acceleration momentum of  $p_{\text{cut}} = 3.5 \times 10^7$  remain fixed. The left-hand panel of Figure 5.13 shows the multi-frequency spectrum. For clarity, we show

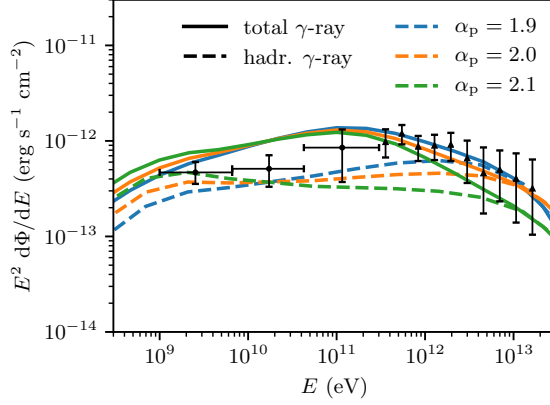


Figure 5.12: Total  $\gamma$ -ray spectra (solid lines) and hadronic  $\gamma$ -ray spectra (dashed lines) with different CR proton spectral indices  $\alpha_p$  are compared to *Fermi* and HESS data. A best-fit to observational data is given for a CR proton spectral index of  $\alpha_p = 1.9$ .

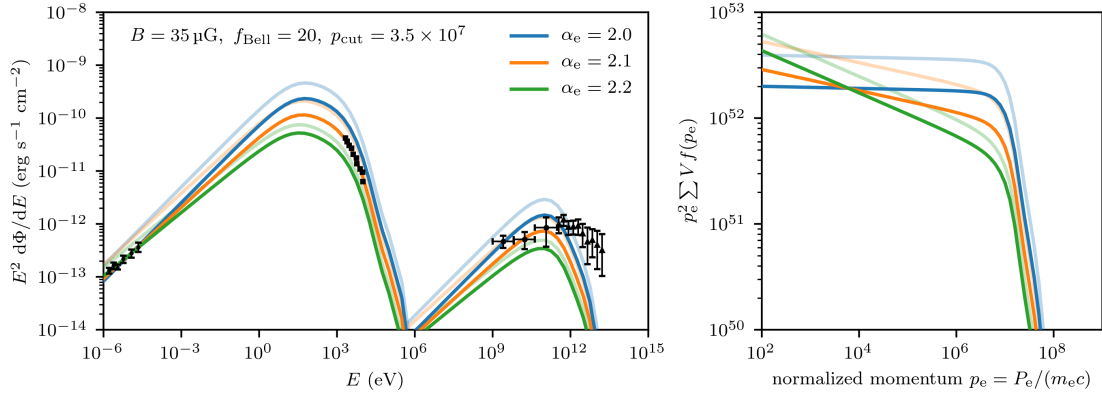


Figure 5.13: Multi-frequency spectra (left) and CR electron spectra (right) for different CR electron spectral indices  $\alpha_e$ . The multi-frequency spectra show only the leptonic emission and use only CMB photons for the IC calculation. Semi-transparent lines show the results using a maximal electron acceleration efficiency of  $\zeta_{e,\max} = 10^{-3}$  and opaque lines show spectra where  $\zeta_{e,\max}$  is chosen such that they are in agreement with observational radio data.

only the IC spectrum on CMB photons in the  $\gamma$ -ray range. The panel on the right hand side shows the total volume-weighted CR electron spectrum. Semi-transparent lines show the result for a fixed CR electron acceleration efficiency of  $\zeta_{e,\max} = 10^{-3}$  in both panels. Opaque lines show the same model, however with a renormalised CR electron acceleration efficiency such that the spectral radio data is fit. Acceleration efficiencies  $\zeta_{e,\max}$  of renormalised spectra are  $5.1 \times 10^{-3}$  for  $\alpha_e = 2.0$ ,  $5.4 \times 10^{-3}$  for  $\alpha_e = 2.1$ , and  $7.0 \times 10^{-3}$  for  $\alpha_e = 2.2$ .

In the following discussion, we refer to opaque lines with floating acceleration efficiency thus ensuring a match to radio data. A CR electron spectral index of  $\alpha_e = 2.0$ , which is the test-particle limit of DSA theory, leads to an overestimate of the  $\gamma$ -ray flux at energies of 10 to 100 GeV. Therefore a larger spectral index  $\alpha_e > 2.0$  is necessary in order to produce an agreement with  $\gamma$ -ray data. However, a spectral index of  $\alpha_e = 2.2$  leads to an underestimate of X-ray data which cannot be compensated by having a larger acceleration momentum  $p_{\text{cut}}$  because of the different spectral shape. Hence, a spectral index of  $\alpha_e = 2.1$  is our best fit which produces results compatible with X-ray and  $\gamma$ -ray data.

We have shown the influence of the CR electron and proton spectral index on the spectrum and that a good agreement with observations is obtained with the spectral indices  $\alpha_e = 2.1$  for electrons and  $\alpha_p = 1.9$  for protons. We use these two best-fit values throughout the rest of our parameter study.

There are several mechanisms which potentially lead to spectral indices that are different from the canonical value of  $\alpha = 2$  in the test-particle limit of diffusive shock acceleration (DSA) and to slight deviations of the electron and proton spectral indices. First, accelerated CRs provide a pressure component in addition to thermal pressure that changes the shock structure which is referred to as non-linear DSA (e.g. Eichler, 1979; Bell, 1987; Amato and Blasi, 2005; Reynolds, 2008). The incoming flow is gradually decelerated in a dynamical precursor that is generated by CRs diffusing ahead of the shock. A thermal subshock remains but the overall compression ratio from far upstream to downstream is increased. Low energetic particles, i.e. CR electrons and CR protons with small momenta, obtain a softer spectral index by experiencing a weaker shock. Particles with greater particle energies have a longer mean free path between scattering events and are able to experience the larger compression ratio. Second, the spectral index of accelerated particles in DSA depends on the escape probability (Bell, 1978a) which can be estimated with the diffusive spatial transport (Kirk et al., 1996; Lazarian and Yan, 2014). It is found that the spectral index follows the relation  $\alpha = 3r/(r - 1) \times [1 + (1 - \beta)/r] - 2$  where  $r$  is the shock compression ratio and  $\beta$  determines the diffusive transport via the relation  $\langle \Delta x^2 \rangle \propto t^\beta$ . Standard diffusion with  $\beta = 1$  gives  $\alpha = 2$  but anomalous transport in turbulent fields yields different diffusion schemes and different spectral indices (Duffy et al., 1995; Lazarian and Yan, 2014). Third, the spectrum of accelerated particles at SNRs can be steepened by geometric and time-dependent processes (Malkov and Aharonian, 2019) or non-local processes associated with changes of the magnetic field orientation along the shock front (Hanusch et al., 2019). Fourth, accelerated CRs self generate electric and magnetic fields which lowers the energy of the CRs and thereby modifies the spectrum (Zirakashvili and

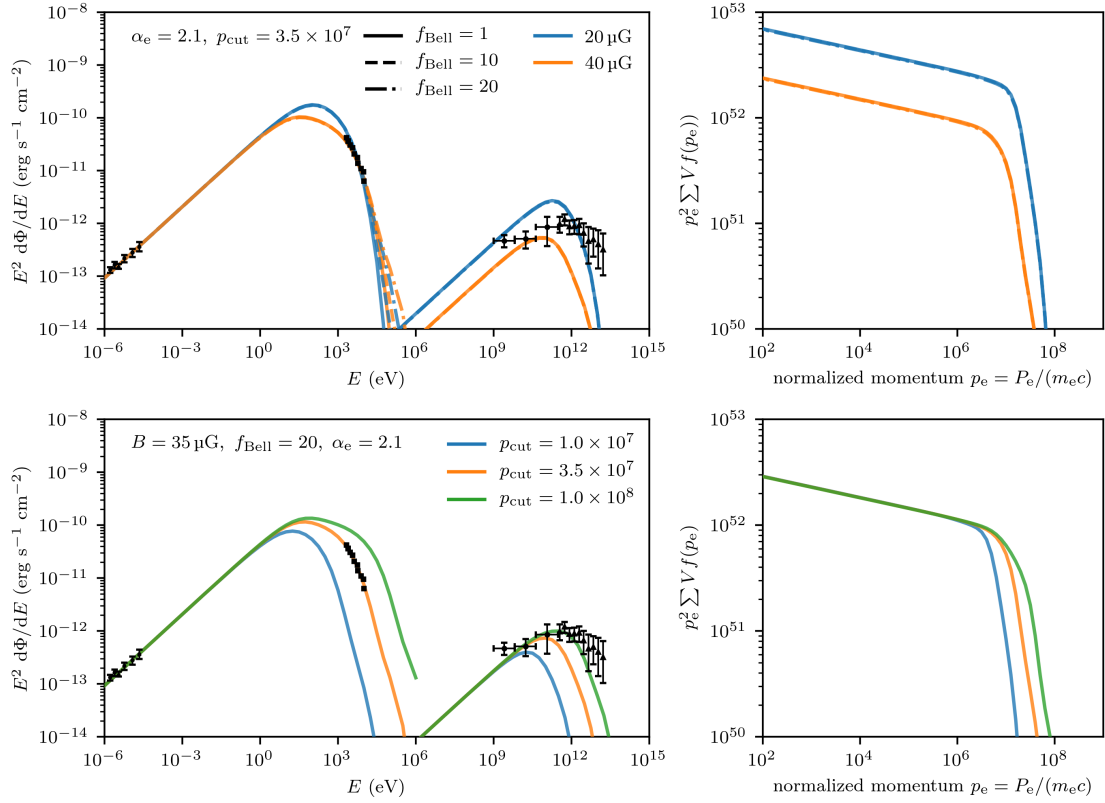


Figure 5.14: Multi-frequency spectra (left) and CR electron spectra (right) for different equivalent magnetic fields and Bell amplification factors (top row) and for different maximal acceleration momenta  $p_{\text{cut}}$  of CR electrons (bottom row). The acceleration efficiency is chosen such that the spectra fit observed radio data.

Ptuskin, 2015; Osipov et al., 2019; Bell et al., 2019), potentially in a way that is different for electrons and protons (Bell et al., 2019). Fifth, the inclusion of higher-order anisotropies of the CR spectrum near to shock shows that the spectral index changes as a function of magnetic obliquity and shock velocity (Bell et al., 2011; Takamoto and Kirk, 2015).

### 5.6.2 Magnetic Amplification and Maximum Momentum

We move on to study the influence of magnetic amplification and maximum CR electron momentum on the spectrum. In the following, we always refer to spectra that are obtained with a free floating CR electron acceleration efficiency  $\zeta_{e,\text{max}}$  such that a fit to spectral radio data is obtained.

The top row of Figure 5.14 shows how different equivalent magnetic fields and Bell amplification factors  $f_{\text{Bell}}$  shape the multi-frequency spectrum (left) and which CR electron

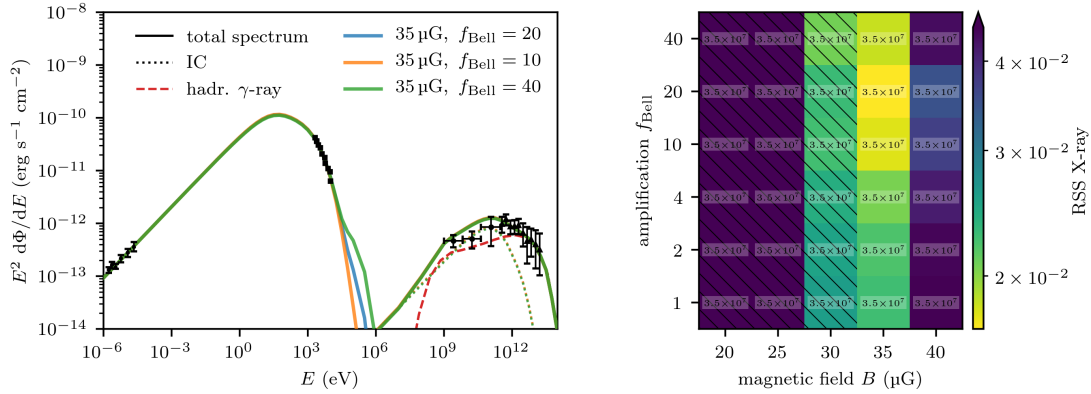


Figure 5.15: Best fit multi-frequency spectra (left) and parameter space (right) that is spanned by an equivalent magnetic field ( $x$ -axis), Bell amplification factor ( $y$ -axis), and maximum CR electron momentum (insets). The colour bar on the right hand side indicates the quality of fit to X-ray data in terms of the residual sum of squares (RSS). The RSS values are calculated in logarithmic space. Hatched parameter combinations indicate that simulations produce high  $\gamma$ -ray emission exceeding  $2.5\sigma$  uncertainties of observational data. This motivates our choice of  $35\ \mu\text{G}$  and a Bell amplification factor 10 for our best-fit model.

spectrum (right) is necessary to fit the radio data. For clarity, the multi-frequency spectrum only contains the leptonic spectra together with the IC emission on CMB photons. A strong magnetic field leads to fast cooling CR electrons such that the synchrotron spectrum is reduced at photon energies  $E \gtrsim 10\ \text{eV}$  while extending its tail to a slightly larger energy as can be seen in the left-hand panel. The orange lines representing simulations with a  $40\ \mu\text{G}$  field deviate at lower energies from the synchrotron power law in comparison to the blue lines representing simulations with a  $20\ \mu\text{G}$  field. The Bell amplification factor has only a minor influence on the synchrotron spectrum because these Bell-amplified fields are constrained to a small volume at the shock front. The acceleration efficiencies  $\zeta_{e,\text{max}}$  are  $1.3 \times 10^{-2}$  for the  $20\ \mu\text{G}$  equivalent field and  $4.3 \times 10^{-3}$  for  $40\ \mu\text{G}$ .

The top right panel of Figure 5.14 shows that the CR electron spectrum of the  $40\ \mu\text{G}$  simulation (orange line) is lower than that of the  $20\ \mu\text{G}$  (blue line) because a larger magnetic field requires a lower CR electron acceleration efficiency in order to fit observed radio data. This results in a lower CR electron spectrum which implies a lower IC emissivity as can be seen in the left-hand panel. Consequently, low magnetic fields with larger CR electron acceleration efficiencies are excluded because they overestimate the high-energy  $\gamma$ -ray spectrum.

The bottom row of Figure 5.14 shows the influence of the maximum acceleration momentum  $p_{\text{cut}}$  of CR electrons. The panel on the left-hand side shows the multi-frequency spectrum while the right-hand side shows the CR electron spectrum. Note that

while we fix  $p_{\text{cut}}$  for a given simulation, the effective spectral cutoff of our Lagrangian particles is dynamically evolving due to adiabatic processes and cooling losses so that the final cutoff of the total spectrum is a superposition of all individually transported spectral cutoffs. It is apparent that the maximum acceleration momentum is important for obtaining an agreement with spectral X-ray data. A too small maximum acceleration momentum underestimates the synchrotron spectrum at X-ray energies whereas a too large value leads to an overestimate. The cooling of the CR electron spectrum due to synchrotron and IC losses cannot compensate a too large maximum acceleration momentum because it leads to flattening of the synchrotron spectrum rather than a cutoff as suggest by the data.

We have shown, that the value of the turbulently amplified magnetic field, the Bell amplification factor, and the maximum acceleration momentum are essential for obtaining a multi-frequency spectrum that is in agreement with observations. We now extend our study to a larger parameter space of these values considering now hadronic  $\gamma$ -rays as well. Figure 5.15 shows the result of this study for the best-fit values of the spectral indices  $\alpha_p = 1.9$  for CR protons and  $\alpha_e = 2.1$  for electrons. The panel on the left-hand side shows the three best model which are in agreement with observations. Solid lines represent the total spectrum while dotted and dashed lines show the leptonic and hadronic  $\gamma$ -ray spectrum, respectively. The right-hand panel of Figure 5.15 shows the residual sum of squares (RSS) at X-ray energies in the parameter space of magnetic field and amplification factor indicated by the colours from yellow (good fit) to purple (bad fit). The RSS values are calculated with the logarithmic spectral values as they span an order of magnitude. For each combination of equivalent magnetic field and Bell amplification factor, we report the best-fit value of the maximum acceleration momentum of CR electrons. Hatched cells represent parameter combinations that overproduce the spectrum at  $\gamma$ -ray energies, i.e. a total spectrum exceeding  $2.5\sigma$  of at least one *Fermi* or HESS data point.

The parameter combination of an equivalent magnetic field of  $B = 35 \mu\text{G}$ , a Bell amplification factor of 20, and a maximum acceleration momentum of  $p_{\text{cut}} = 3.5 \times 10^7$  produces the best agreement with X-ray data while being compatible with  $\gamma$ -ray data. By construction, they also fit radio data. We note that there is some degeneracy between these values as well as other parameters, e.g. density, explosion energy and CR spectral index. Hence, slightly different combinations might result in similar agreement with observational data. However, certain ranges of magnetic fields strengths can be excluded because they either overestimate  $\gamma$ -ray data, e.g. combinations of a low magnetic fields and a large acceleration efficiency (see Figure 5.14), or they underestimate X-ray data due to fast cooling of CR electrons in strong magnetic fields. We conclude that volume-filling magnetic fields of  $B \approx 35 \mu\text{G}$  (possibly amplified through a turbulent small-scale dynamo) produce a good agreement with observations.

### 5.6.3 Ambient Photon Field and Density

We have discussed how the magnetic field indirectly influences the IC spectrum via the CR electron acceleration efficiency. We now discuss the direct influence of radiation fields

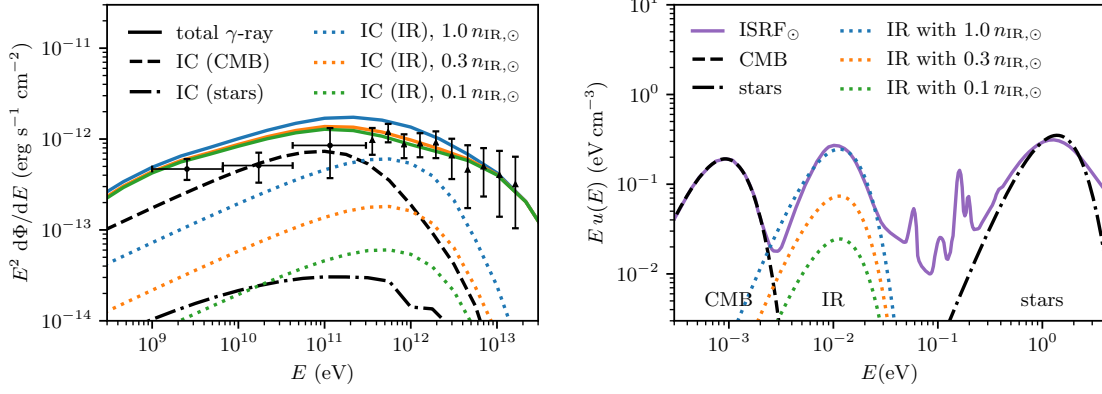


Figure 5.16: High energy  $\gamma$ -ray spectrum (left) and interstellar radiation fields (ISRF) (right). On the left hand side, the solid lines show the total  $\gamma$ -ray spectrum as sum of three IC components: CMB (dashed), IR (dotted), and star light (dash-dotted). Blue, orange, and green lines represent variable IR components where  $n_{\text{IR},\odot}$  is the density of infrared photons at the solar radius. On the right hand side, we show the ISRF at solar radius (Porter and Strong, 2005; Porter et al., 2008) and our three-component ISRF model used for IC calculation.

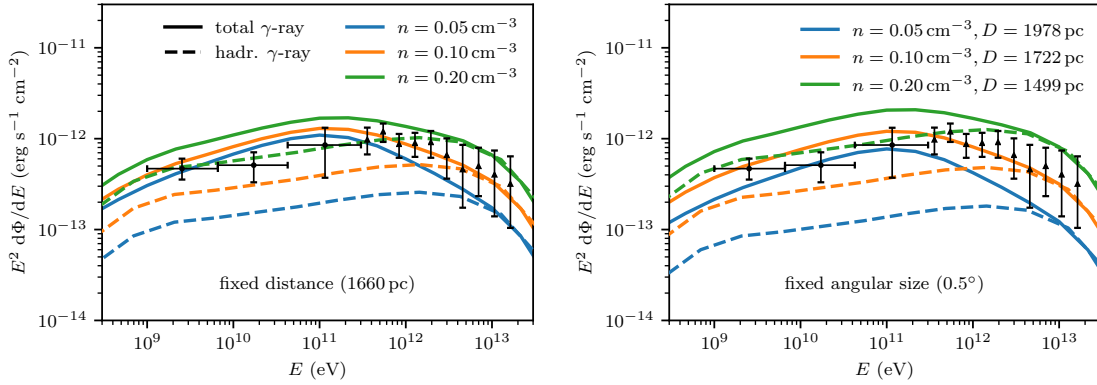


Figure 5.17: High energy  $\gamma$ -ray spectrum for varying ambient gas densities at a fixed distance of 1660 pc (left) and at a fixed angular size of  $0.5^\circ$  (right).

on the IC spectrum. Figure 5.16 shows the high energy  $\gamma$ -ray spectrum in the left-hand panel for three different photons fields which are shown in the right-panel together with the interstellar radiation field models at different locations in the Milky Way. The blue lines represent the spectrum that is obtained by fitting three black body spectra to the radiation field at the solar radius. Orange and green lines represent variations where  $n_{\text{IR}}$  is given by  $0.3 n_{\text{IR},\odot}$  and  $0.1 \times n_{\text{IR},\odot}$ , respectively. It is apparent that an infrared field similar to that of the solar radius leads to large total  $\gamma$ -ray spectrum (blue lines, left) exceeding  $\gamma$ -ray data from *Fermi* and HESS. The contribution of the IC spectrum produced by interaction of CR electrons with starlight photons is negligible as it is suppressed due to the Klein-Nishina effect. Lower infrared fields with  $n_{\text{IR}} \lesssim 0.3 \times n_{\text{IR},\odot}$  (orange, green) lead to a good agreement of the the total  $\gamma$ -ray spectrum with observations.

Finally, we explain the influence of ambient gas density onto the gamma-ray spectrum. Figure 5.17 shows the total  $\gamma$ -ray spectrum (solid lines) together with the hadronic  $\gamma$ -ray spectrum (dashed lines) for a fixed distance of 1660 pc to the remnant (left) and for a fixed angular size of  $0.5^\circ$  (right). The panel on the left-hand side shows the direct effect of a reduced target proton density for hadronic  $\gamma$ -ray production because it is directly proportional to the ambient gas density. Hence, the simulation with a low number density of  $n = 0.05 \text{ cm}^{-3}$  (blue lines) underestimates the  $\gamma$ -ray flux for  $E \gtrsim 1 \text{ TeV}$  whereas the simulation with a high number density of  $n = 0.2 \text{ cm}^{-3}$  (green lines) leads to an overestimate.

However, we cannot choose the density as a free parameter and must also take into account the size of the remnant which is larger for lower densities. The radius of the remnant in the adiabatic phase evolves with

$$R \propto \left( \frac{E_{\text{SN}} t^2}{n} \right)^{1/5} \quad (5.11)$$

according to the Sedov–Taylor solution where  $E_{\text{SN}}$  is the SNR explosion energy. If we fix the angular size of the SNR to the observed solid angle, the distance  $D$  has to scale in proportion with the radius. Consequently, the spectrum is influenced and scales according to

$$\frac{d\Phi}{dE} \propto D^{-2} \propto n^{2/5}. \quad (5.12)$$

This is shown in the right-hand panel of Figure 5.17, where a low (high) density leads to an even stronger underestimate (overestimate) of the  $\gamma$ -ray spectrum. The resulting distances are given in the plot.

Our best fit value  $n = 0.12 \text{ cm}^{-3}$  for the ambient density is well within the statistical and systematic uncertainties of the observations. Analysis of the SE rim with *XMM-Newton* yields post-shock densities from  $n_{\text{post}} = 1.44_{-0.11}^{+0.10}$  to  $1.99_{-0.17}^{+0.4}$   $\text{cm}^{-3}$  with the larger values arising due to CR shock modification and a pre-shock density of  $n_{\text{pre}} \approx 0.04 \text{ cm}^{-3}$  (Miceli et al., 2012) which is in agreement with  $n_{\text{pre}} = 0.05 \text{ cm}^{-3}$  obtained by Acero et al. (2007).

Comparable results are inferred from *Chandra* data which show that the pre-shock density is  $n_{\text{pre}} = 0.045^{+0.049}_{-0.020} \text{ cm}^{-3}$  (Winkler et al., 2014). Higher densities are found in the western part of the SN 1006 where the remnant interacts with an atomic cloud in the SW and an H $\alpha$ -bright cloud in the NW. In the NW, analysis of *Spitzer* data gives a post-shock density of  $n_{\text{post}} = 1.4 \pm 0.5 \text{ cm}^{-3}$  which yields a pre-shock density of  $n_{\text{pre}} = 0.35 \pm 0.125 \text{ cm}^{-3}$  using a standard shock compression ratio of four (Winkler et al., 2013). In the SW, analysis of X-ray data yields  $0.3 \text{ cm}^{-3}$  to  $0.5 \text{ cm}^{-3}$  for the pre-shock density (Miceli et al., 2014; Miceli et al., 2016).

## 5.7 Discussion and Conclusion

We have performed 3D MHD simulations of the remnant of SN 1006 with CR proton and electron physics which includes the spatial and temporal evolution of the CR electron spectrum. We account for leptonic emission processes, i.e. synchrotron and IC emission, and hadronic  $\gamma$ -ray emission, and present multi-frequency spectra and non-thermal emission maps in the radio, X-ray, and  $\gamma$  rays. We model the magnetic obliquity dependent CR proton acceleration following results of hybrid particle-in-cell simulations of Caprioli and Spitkovsky (2014a). In addition, we study different models of obliquity dependent CR electron acceleration (some of which are also inspired by recent particle-in-cell simulations) and explore the influence of various model parameters on the maps and non-thermal emission spectra.

Our main conclusions are summarised here.

- Because our simulations lack the dynamic range to fully resolve a turbulent dynamo caused by small-scale density fluctuations in the interstellar medium, and our model of the CR physics precludes the excitation and growth of the non-resonant hybrid instability (Bell, 2004), we model these processes in form of a subgrid model. To this end, we evoke a turbulent dynamo (or a similar plasma process) behind the shock to generate a volume-filling magnetic field inside the SNR with values of  $B = 35 \mu\text{G}$  ( $B = 140 \mu\text{G}$ ) in the quasi-parallel (quasi-perpendicular) regions. In this best-fit model, we additionally account for the amplification of magnetic fields by a factor of about 20 due to Bell's instability (with the same obliquity dependence as we adopt for the CR proton acceleration efficiency) and assume that the SNR expands into a homogeneous medium on large scales with an average gas number density of  $n = 0.12 \text{ cm}^{-3}$ .
- Leptonic and hadronic  $\gamma$ -ray emission are both important for explaining the observed  $\gamma$ -ray spectrum. In our model, hadronic pion-decay and leptonic emission (primarily from Compton-upscattering of CMB photons) are contributing to the emission at GeV  $\gamma$ -ray energies accessible to the *Fermi*  $\gamma$ -ray space telescope approximately by equal parts. Within our adopted large parameter space, we find no solution with a smaller IC  $\gamma$ -ray component that simultaneously matches the multi-frequency

spectrum and the non-thermal emission maps. However, hadronic emission is dominating at TeV energies that are observable by imaging air Cherenkov telescopes. We find, that the HESS  $\gamma$ -ray map at photon energies  $E > 500$  GeV is thus dominated by hadronic pion-decay emission.

- The model of preferentially *quasi-parallel shock acceleration of CR electrons* produces non-thermal emission maps and a multi-frequency spectrum that are in very good agreement with all observations. In this model, the electron acceleration efficiency of radio-emitting GeV electrons at quasi-perpendicular shocks is suppressed at least by a factor ten. The models of obliquity independent and *preferentially quasi-perpendicular shock acceleration* produce radio and X-ray maps that are in disagreement with observations. Because the simulated  $\gamma$ -ray map, which is dominated by hadronic emission, agrees with the observation, a rotation of the large-scale magnetic field by  $90^\circ$  in the plane of sky cannot resolve this disagreement. Hence, this precludes extrapolation of 1D plasma particle-in-cell simulations of particle acceleration at SNR shock conditions that favour preferentially quasi-perpendicular electron acceleration at shocks.
- The low level of observed  $\gamma$ -ray flux requires a volume-filling strong magnetic field so that most of the electron energy is emitted via synchrotron emission. The preference of quasi-parallel acceleration of protons and electrons argues for efficient amplification of magnetic fields via Bell's instability (or a similar plasma process). We demonstrate that these Bell-amplified magnetic fields have to decay on short length scales of order 100 gyroradii for TeV particles. Otherwise, CR electrons are subject to strong synchrotron losses which would lead to extended radial profiles of the radio and X-ray synchrotron emission at the shock that are in disagreement with observations. However, the exact value of the Bell amplification factor is only weakly constrained by the total spectrum because those amplified fields are confined to a small emission volume around the shock front.

Our work opens up a new avenue to study the physics of electron acceleration at shocks and connects plasma physics at collisionless shocks to astrophysical scales of SNRs in a novel and innovative manner.

# 6 Conclusions and Outlook

## 6.1 Conclusions

In this work, I have successfully developed and presented the new stand-alone code `CREST` that follows spatially and temporally resolved the evolution of CR electron spectra on Lagrangian tracer particles. It works as a post-processing code of MHD simulations with the `AREPO` code but adopting it to other MHD codes is possible.

The code evolves CR electron spectra according to the Fokker–Planck equation and models spatial transport of CR electrons by advection with the ambient gas. It includes all relevant cooling and gain processes of CR electrons. First, the code covers losses and gains of the spectrum by adiabatic expansion or compression of the ambient gas, respectively. Secondly, the code includes Coulomb cooling and radiative losses such as synchrotron radiation, bremsstrahlung, and inverse Compton emission. Thirdly, Fermi-I acceleration and reacceleration at shocks and Fermi-II acceleration by transit time damping is handled. The spectrum is evolved with an innovative hybrid numerical and analytical treatment that prevents short time steps due to fast cooling processes and enables the numerical evolution on time steps comparable to the MHD time step. This approach allows to track the spectrum accurately with high resolution and makes simulations of large astrophysical systems such as galaxies and galaxy clusters with CR electrons feasible. It enables to connect MHD simulations and CR physics to observations by means of non-thermal emission signatures that are multi-frequency spectra and spatially resolved maps of (non-thermal) radio, X-ray, and  $\gamma$ -ray emission.

I have thoroughly tested the code in idealized one-zone tests which allow for a direct comparison of the numerical results to analytical solutions or to the literature. In addition, the code has been tested on 1D and 3D MHD simulations of shock-tubes and 3D Sedov–Taylor blast wave simulations.

So far, the main application of this code has been the study of the remnant of SN 1006 which is an ideal laboratory for CR acceleration. I have addressed the issue whether the  $\gamma$ -ray emission is dominated by leptonic or hadronic emission. Both, CR protons and electrons, are necessary to explain the spectrum but the very high energy (TeV)  $\gamma$ -ray surface brightness map is dominated by hadronic emission due to sensitivity range of the HESS telescope. Furthermore, the obliquity-dependent acceleration mechanism of CR electrons has been discussed and compared to findings of PIC simulations. Although there are 1D PIC simulations suggesting preferentially quasi-perpendicular acceleration of CR electrons, the best agreement to the observed morphology is obtained with the model of

quasi-parallel acceleration. The acceleration of CRs is closely linked to the amplification of magnetic fields. CR protons which are preferentially accelerated in quasi-parallel regions drive the Bell instability which produces strong perpendicular magnetic fields which in turn possibly provide the quasi-perpendicular environment necessary for efficient CR electron acceleration. I find that the overall magnetic field is tightly constrained by the combination of the multi-frequency spectrum and observed morphology in different wave bands. I have shown that the Bell amplified magnetic fields are an important ingredient but that the morphology can only be explained by volume-filling amplified fields potentially driven by a turbulent dynamo.

## 6.2 Outlook

The current implementation of `CREST` treats advection with the gas as dominant CR transport process. However, other transport processes such as streaming or spatial diffusion can become important if the advection length within a timescale of interest becomes comparable or smaller than the streaming or diffusion length, respectively. The inclusion of additional transport processes requires an enhanced numerical treatment detached from the tracer particle approach which is possible but beyond the scope of this work. However, advection is the dominating spatial transport in environments of SNRs or fast galactic outflows and thus renders the current implementation sufficient.

A further application of the `CREST` code is the simulation of other SNRs such as RXJ1713.4-3946 or Vela Jr (RXJ0582.0-4622) as they most-likely originate from core collapse SNe. Their different environment with dense molecular clumps also shows strongly amplified magnetic fields which could favor hadronic TeV  $\gamma$ -ray emission. It would be interesting to apply the results of this study on SN 1006 to these environments and test whether similar conclusions can be drawn.

The next level of interesting applications is the study of galactic outflows that are observed in many different wavebands and their understanding is considered to be the holy grail of galaxy formation. A first study could be to test whether the often applied steady state assumption of the CR spectrum in galactic outflows holds and under which conditions a detailed modeling of the spectrum is required. The next step is a self-consistent numerical simulation of the Milky Way with a Galactic outflow in order to shed light on the origin of the Fermi bubbles. Simulating the CR electron spectrum can distinguish between hadronic and leptonic models for the  $\gamma$ -ray emission of the outflowing regions. The driving mechanism of the Fermi bubbles is a crucial point, as models relying on AGN or starburst events imply different outflow velocities. In slow outflows driven by starburst events the CR electron spectrum cools away before it reaches the top of the bubbles which makes reacceleration by shocks or Fermi-II processes inevitable. All these points can be studied in the framework provided by the `CREST` code.

On even larger scales, galaxy clusters and their radio sources offer another field of interesting applications of the `CREST` code. Radio halos that appear in one third of

X-ray luminous clusters can be explained by a hadronic model or a leptonic model. As CR electrons quickly cool away they require sufficient reacceleration to explain the radio emission. The Fermi-II mechanism via turbulent reacceleration is an essential ingredient for the leptonic model. It is included into `CREST` which allows modeling of radio halos. Radio relics which are often located at the cluster outskirts are characterized by elongated and polarized radio emission. Weak shocks can reaccelerate CR electrons to radio synchrotron emitting momenta which is also modeled by `CREST`. Another application field is offered by active galactic nuclei (AGN) whose jets drive outflows and inflate bubbles which are filled by radio synchrotron emitting CR electrons.

The plethora of astrophysical systems which are characterized by non-thermal radio, X-ray, and  $\gamma$ -ray emission of CR electrons provides a great amount of research applications. The `CREST` code together with MHD simulations makes the self-consistent modeling of these systems possible and links them to observations.



# First Author Publications of G. Winner

Georg Winner, Christoph Pfrommer, Philipp Girichidis, and Rüdiger Pakmor. Evolution of cosmic ray electron spectra in magnetohydrodynamical simulations. *MNRAS*, 488 (2):2235–2252, Sep 2019. doi: 10.1093/mnras/stz1792.

Georg Winner, Christoph Pfrommer, Philipp Girichidis, Maria Werhahn, and Matteo Pais. Evolution and observational signatures of the cosmic ray electron spectrum in SN 1006. *arXiv e-prints*, 2006:arXiv:2006.06683, June 2020. URL <http://adsabs.harvard.edu/abs/2020arXiv200606683W>.



# Bibliography

- A. A. Abdo et al. Fermi large area telescope first source catalog. *ApJS*, 188(2):405–436, June 2010. doi: 10.1088/0067-0049/188/2/405. URL <https://ui.adsabs.harvard.edu/abs/2010ApJS...188..405A>.
- F. Acero, J. Ballet, and A. Decourchelle. The gas density around sn 1006. *A&A*, 475(3):883–890, December 2007. doi: 10.1051/0004-6361/20077742. URL <https://ui.adsabs.harvard.edu/abs/2007A&A...475..883A>.
- F. Acero et al. First detection of vhe  $\gamma$ -rays from sn 1006 by hess. *A&A*, 516:A62, June 2010. doi: 10.1051/0004-6361/200913916. URL <https://ui.adsabs.harvard.edu/abs/2010A%26A...516A..62A>.
- F. Acero et al. Study of tev shell supernova remnants at gamma-ray energies. *A&A*, 580:A74, August 2015. doi: 10.1051/0004-6361/201525932. URL <https://ui.adsabs.harvard.edu/abs/2015A%26A...580A..74A>.
- F. A. Aharonian, S. R. Kelner, and A. Y. Prosekin. Angular, spectral, and time distributions of highest energy protons and associated secondary gamma rays and neutrinos propagating through extragalactic magnetic and radiation fields. *Phys. Rev. D*, 82(4):043002, August 2010. doi: 10.1103/PhysRevD.82.043002. URL <http://adsabs.harvard.edu/abs/2010PhRvD...82d3002A>.
- A. W. Alsabti and P. Murdin. *Supernovae and Supernova Remnants: The Big Picture in Low Resolution*, page 3. Springer International Publishing, 2017. doi: 10.1007/978-3-319-21846-5\_1.
- E. Amato and P. Blasi. A general solution to non-linear particle acceleration at non-relativistic shock waves. *MNRAS*, 364(1):L76–L80, Nov 2005. doi: 10.1111/j.1745-3933.2005.00110.x.
- M. Araya and F. Frutos. On the nature of the TeV emission from the supernova remnant SN 1006. *Monthly Notices of the Royal Astronomical Society*, 425:2810–2816, October 2012. ISSN 0035-8711. doi: 10.1111/j.1365-2966.2012.21580.x. URL <http://adsabs.harvard.edu/abs/2012MNRAS.425.2810A>.
- W. I. Axford, E. Leer, and G. Skadron. The Acceleration of Cosmic Rays by Shock Waves. In *International Cosmic Ray Conference*, volume 11 of *International Cosmic Ray Conference*, page 132, January 1977.

- A. Bamba et al. Suzaku wide-band observations of sn1006. *PASJ*, 60:S153–S162, January 2008. doi: 10.1093/pasj/60.sp1.S153. URL <https://ui.adsabs.harvard.edu/abs/2008PASJ...60S.153B>.
- A. Bamba, R. Yamazaki, M. Ueno, and K. Koyama. Small-Scale Structure of the SN 1006 Shock with Chandra Observations. *ApJ*, 589(2):827–837, June 2003. doi: 10.1086/374687.
- A. Bamba, R. Yamazaki, and J. S. Hiraga. Chandra observations of galactic supernova remnant vela jr.: A new sample of thin filaments emitting synchrotron x-rays. *ApJ*, 632(1):294–301, October 2005. doi: 10.1086/432711. URL <https://ui.adsabs.harvard.edu/abs/2005ApJ...632..294B>.
- N. Battaglia, C. Pfrommer, J. L. Sievers, J. R. Bond, and T. A. Enßlin. Exploring the magnetized cosmic web through low-frequency radio emission. *MNRAS*, 393:1073–1089, March 2009. doi: 10.1111/j.1365-2966.2008.14136.x. URL <http://adsabs.harvard.edu/abs/2009MNRAS.393.1073B>.
- R. Beck and R. Wiełebinski. Magnetic Fields in Galaxies. *Planets, Stars and Stellar Systems. Volume 5: Galactic Structure and Stellar Populations*, page 641, 2013. doi: 10.1007/978-94-007-5612-0\_13. URL <http://adsabs.harvard.edu/abs/2013pss5.book..641B>.
- A. R. Bell. The acceleration of cosmic rays in shock fronts. i. *MNRAS*, 182:147–156, January 1978a. doi: 10.1093/mnras/182.2.147. URL <http://adsabs.harvard.edu/abs/1978MNRAS.182..147B>.
- A. R. Bell. The acceleration of cosmic rays in shock fronts. ii. *MNRAS*, 182:443–455, February 1978b. doi: 10.1093/mnras/182.3.443. URL <http://adsabs.harvard.edu/abs/1978MNRAS.182..443B>.
- A. R. Bell. The non-linear self-regulation of cosmic ray acceleration at shocks. *MNRAS*, 225:615–626, April 1987. doi: 10.1093/mnras/225.3.615.
- A. R. Bell. Turbulent amplification of magnetic field and diffusive shock acceleration of cosmic rays. *MNRAS*, 353:550–558, September 2004. doi: 10.1111/j.1365-2966.2004.08097.x. URL <https://ui.adsabs.harvard.edu/abs/2004MNRAS.353..550B>.
- A. R. Bell, K. M. Schure, and B. Reville. Cosmic ray acceleration at oblique shocks. *MNRAS*, 418(2):1208–1216, December 2011. doi: 10.1111/j.1365-2966.2011.19571.x.
- A. R. Bell, J. H. Matthews, and K. M. Blundell. Cosmic ray acceleration by shocks: spectral steepening due to turbulent magnetic field amplification. *MNRAS*, 488(2): 2466–2472, September 2019. doi: 10.1093/mnras/stz1805.

- 
- P. Benaglia, G. E. Romero, J. Martí, C. S. Peri, and A. T. Araudo. Detection of nonthermal emission from the bow shock of a massive runaway star. *A&A*, 517:L10, July 2010. doi: 10.1051/0004-6361/201015232.
- E. G. Berezhko, G. Pühlhofer, and H. J. Völk. Theory of cosmic ray and  $\gamma$ -ray production in the supernova remnant RX J0852.0-4622. *Astronomy and Astrophysics*, 505:641–654, October 2009. ISSN 0004-6361. doi: 10.1051/0004-6361/200809473. URL <http://adsabs.harvard.edu/abs/2009A%26A...505..641B>.
- E. G. Berezhko, L. T. Ksenofontov, and H. J. Völk. Nonthermal Emission of Supernova Remnant SN 1006 Revisited: Theoretical Model and the H.E.S.S. Results. *The Astrophysical Journal*, 759:12, November 2012. ISSN 0004-637X. doi: 10.1088/0004-637X/759/1/12. URL <http://adsabs.harvard.edu/abs/2012ApJ...759...12B>.
- R. D. Blandford and J. P. Ostriker. Particle acceleration by astrophysical shocks. *ApJ*, 221:L29–L32, 1978. ISSN 0004-637X. doi: 10.1086/182658. URL <http://adsabs.harvard.edu/abs/1978ApJ...221L..29B>.
- R. Blandford and D. Eichler. Particle acceleration at astrophysical shocks: A theory of cosmic ray origin. *Phys. Rep.*, 154:1–75, 1987. ISSN 0370-1573. doi: 10.1016/0370-1573(87)90134-7. URL <http://adsabs.harvard.edu/abs/1987PhR...154.....1B>.
- P. Blasi. The origin of galactic cosmic rays. *A&A Rev.*, 21:70, November 2013. doi: 10.1007/s00159-013-0070-7. URL <http://adsabs.harvard.edu/abs/2013A%26ARv...21...70B>.
- J. M. Blondin, E. B. Wright, K. J. Borkowski, and S. P. Reynolds. Transition to the Radiative Phase in Supernova Remnants. *The Astrophysical Journal*, 500:342–354, June 1998. ISSN 0004-637X. doi: 10.1086/305708. URL <http://adsabs.harvard.edu/abs/1998ApJ...500..342B>.
- G. R. Blumenthal and R. J. Gould. Bremsstrahlung, synchrotron radiation, and compton scattering of high-energy electrons traversing dilute gases. *Reviews of Modern Physics*, 42:237–271, 1970. ISSN 0034-6861. doi: 10.1103/RevModPhys.42.237. URL <http://adsabs.harvard.edu/abs/1970RvMP...42..237B>.
- F. Bocchino, S. Orlando, M. Miceli, and O. Petruk. Constraints on the local interstellar magnetic field from non-thermal emission of sn1006. *A&A*, 531:A129, July 2011. doi: 10.1051/0004-6361/201016341. URL <https://ui.adsabs.harvard.edu/abs/2011A%26A...531A.129B>.
- A. Bohdan, J. Niemiec, O. Kobzar, and M. Pohl. Electron pre-acceleration at nonrelativistic high-mach-number perpendicular shocks. *ApJ*, 847(1):71, September 2017. doi: 10.

## Bibliography

---

- 3847/1538-4357/aa872a. URL <https://ui.adsabs.harvard.edu/abs/2017ApJ...847...71B>.
- C. M. Booth, O. Agertz, A. V. Kravtsov, and N. Y. Gnedin. Simulations of disk galaxies with cosmic ray driven galactic winds. *ApJ*, 777:L16, November 2013. doi: 10.1088/2041-8205/777/1/L16. URL <http://adsabs.harvard.edu/abs/2013ApJ...777L...16B>.
- A. Boulares and D. P. Cox. Galactic hydrostatic equilibrium with magnetic tension and cosmic-ray diffusion. *ApJ*, 365:544–558, December 1990. doi: 10.1086/169509. URL <http://adsabs.harvard.edu/abs/1990ApJ...365..544B>.
- D. Breitschwerdt, J. F. McKenzie, and H. J. Voelk. Galactic winds. i - cosmic ray and wave-driven winds from the galaxy. *A&A*, 245:79–98, May 1991. URL <http://adsabs.harvard.edu/abs/1991A%26A...245...79B>.
- C. Brezinski. Extrapolation algorithms and pade&acute; approximations: A historical survey. *Appl. Numer. Math.*, 20(3):299–318, March 1996. ISSN 0168-9274. doi: 10.1016/0168-9274(95)00110-7. URL [http://dx.doi.org/10.1016/0168-9274\(95\)00110-7](http://dx.doi.org/10.1016/0168-9274(95)00110-7).
- G. Brunetti and A. Lazarian. Compressible turbulence in galaxy clusters: physics and stochastic particle re-acceleration. *MNRAS*, 378:245–275, 2007. ISSN 0035-8711. doi: 10.1111/j.1365-2966.2007.11771.x. URL <http://adsabs.harvard.edu/abs/2007MNRAS.378..245B>.
- G. Brunetti and A. Lazarian. Particle reacceleration by compressible turbulence in galaxy clusters: effects of a reduced mean free path. *MNRAS*, 412:817–824, 2011. ISSN 0035-8711. doi: 10.1111/j.1365-2966.2010.17937.x. URL <http://adsabs.harvard.edu/abs/2011MNRAS.412..817B>.
- A. M. Bykov, D. C. Ellison, A. Marcowith, and S. M. Osipov. Cosmic ray production in supernovae. *Space Science Reviews*, 214(1):41, Jan 2018. ISSN 1572-9672. doi: 10.1007/s11214-018-0479-4. URL <https://doi.org/10.1007/s11214-018-0479-4>.
- A. M. Bykov, F. Vazza, J. A. Kropotina, K. P. Levenfish, and F. B. S. Paerels. Shocks and Non-thermal Particles in Clusters of Galaxies. *Space Sci. Rev.*, 215:14, February 2019. doi: 10.1007/s11214-019-0585-y.
- D. Caprioli. Cosmic-ray acceleration and propagation. In A. S. Borisov et al., editors, *34th International Cosmic Ray Conference (ICRC2015)*, volume 34 of *International Cosmic Ray Conference*, page 8, July 2015.
- D. Caprioli and A. Spitkovsky. Simulations of ion acceleration at non-relativistic shocks. i. acceleration efficiency. *ApJ*, 783:91, March 2014a. doi: 10.1088/0004-637X/783/2/91.

- 
- D. Caprioli and A. Spitkovsky. Simulations of ion acceleration at non-relativistic shocks. ii. magnetic field amplification. *ApJ*, 794:46, October 2014b. doi: 10.1088/0004-637X/794/1/46.
- D. Caprioli and A. Spitkovsky. Simulations of ion acceleration at non-relativistic shocks. iii. particle diffusion. *ApJ*, 794:47, October 2014c. doi: 10.1088/0004-637X/794/1/47.
- D. Caprioli, A.-R. Pop, and A. Spitkovsky. Simulations and theory of ion injection at non-relativistic collisionless shocks. *ApJ*, 798:L28, 2015. ISSN 0004-637X. doi: 10.1088/2041-8205/798/2/L28. URL <http://adsabs.harvard.edu/abs/2015ApJ...798L..28C>.
- E. Carretti et al. Giant magnetized outflows from the centre of the Milky Way. *Nature*, 493:66–69, January 2013. doi: 10.1038/nature11734.
- G. Cassam-Chenaï, J. P. Hughes, E. M. Reynoso, C. Badenes, and D. Moffett. Morphological evidence for azimuthal variations of the cosmic-ray ion acceleration at the blast wave of sn 1006. *ApJ*, 680:1180–1197, June 2008. doi: 10.1086/588015. URL <https://ui.adsabs.harvard.edu/abs/2008ApJ...680.1180C>.
- S. Celli, G. Morlino, S. Gabici, and F. A. Aharonian. Supernova remnants in clumpy media: particle propagation and gamma-ray emission. *MNRAS*, 487:3199–3213, August 2019. doi: 10.1093/mnras/stz1425. URL <https://ui.adsabs.harvard.edu/abs/2019MNRAS.487.3199C>.
- P. Chang, A. Spitkovsky, and J. Arons. Long-Term Evolution of Magnetic Turbulence in Relativistic Collisionless Shocks: Electron-Positron Plasmas. *The Astrophysical Journal*, 674:378–387, February 2008. ISSN 0004-637X. doi: 10.1086/524764. URL <http://adsabs.harvard.edu/abs/2008ApJ...674..378C>.
- A. L. Charles K. Birdsall. *Plasma physics via computer simulation*. McGraw-Hill, 1985. ISBN 0070053715,9780070053717.
- R. A. Chevalier. Self-similar solutions for the interaction of stellar ejecta with an external medium. *ApJ*, 258:790–797, July 1982. doi: 10.1086/160126.
- J. Cho, E. T. Vishniac, A. Beresnyak, A. Lazarian, and D. Ryu. Growth of Magnetic Fields Induced by Turbulent Motions. *ApJ*, 693(2):1449–1461, March 2009. doi: 10.1088/0004-637X/693/2/1449.
- B. Condon, M. Lemoine-Goumard, F. Acero, and H. Katagiri. Detection of Two TeV Shell-type Remnants at GeV Energies with FERMI LAT: HESS J1731-347 and SN 1006. *ApJ*, 851(2):100, December 2017. doi: 10.3847/1538-4357/aa9be8.

- J. Crank and P. Nicolson. A practical method for numerical evaluation of solutions of partial differential equations of the heat-conduction type. *Mathematical Proceedings of the Cambridge Philosophical Society*, 43(1):50–67, 1947. doi: 10.1017/S0305004100023197.
- L. Crocco. Eine neue Stromfunktion für die Erforschung der Bewegung der Gase mit Rotation. *Zeitschrift Angewandte Mathematik und Mechanik*, 17(1):1–7, Jan 1937. doi: 10.1002/zamm.19370170103.
- C. D. Dermer. Binary collision rates of relativistic thermal plasmas. II - spectra. *ApJ*, 307:47–59, 1986. ISSN 0004-637X. doi: 10.1086/164391. URL <http://adsabs.harvard.edu/abs/1986ApJ...307...47D>.
- G. Dobler, D. P. Finkbeiner, I. Cholis, T. Slatyer, and N. Weiner. The Fermi Haze: A Gamma-ray Counterpart to the Microwave Haze. *ApJ*, 717:825–842, July 2010. doi: 10.1088/0004-637X/717/2/825.
- J. Donnert and G. Brunetti. An efficient fokker-planck solver and its application to stochastic particle acceleration in galaxy clusters. *MNRAS*, 443:3564–3577, October 2014. doi: 10.1093/mnras/stu1417. URL <http://adsabs.harvard.edu/abs/2014MNRAS.443.3564D>.
- J. Donnert, K. Dolag, G. Brunetti, and R. Cassano. Rise and fall of radio haloes in simulated merging galaxy clusters. *MNRAS*, 429:3564–3569, March 2013. doi: 10.1093/mnras/sts628.
- L. O. Drury. An introduction to the theory of diffusive shock acceleration of energetic particles in tenuous plasmas. *Reports on Progress in Physics*, 46:973–1027, 1983. ISSN 0034-4885. doi: 10.1088/0034-4885/46/8/002. URL <http://adsabs.harvard.edu/abs/1983RPPh...46..973D>.
- Y. Dubois and B. Commerçon. An implicit scheme for solving the anisotropic diffusion of heat and cosmic rays in the ramses code. *A&A*, 585:A138, January 2016. doi: 10.1051/0004-6361/201527126. URL <http://adsabs.harvard.edu/abs/2016A%26A...585A.138D>.
- P. Duffy, J. G. Kirk, Y. A. Gallant, and R. O. Dendy. Anomalous transport and particle acceleration at shocks. *A&A*, 302:L21, October 1995.
- K. K. Dyer, T. J. Cornwell, and R. J. Maddalena. 1.4 ghz high-resolution flux-accurate images of sn 1006. *AJ*, 137:2956–2967, February 2009. doi: 10.1088/0004-6256/137/2/2956. URL <https://ui.adsabs.harvard.edu/abs/2009AJ...137.2956D>.
- K. Ehlert, R. Weinberger, C. Pfrommer, R. Pakmor, and V. Springel. Simulations of the dynamics of magnetized jets and cosmic rays in galaxy clusters. *MNRAS*, 481:

- 2878–2900, December 2018. doi: 10.1093/mnras/sty2397. URL <http://adsabs.harvard.edu/abs/2018MNRAS.481.2878E>.
- D. Eichler. Particle acceleration in collisionless shocks - Regulated injection and high efficiency. *The Astrophysical Journal*, 229:419–423, April 1979. ISSN 0004-637X. doi: 10.1086/156969. URL <http://adsabs.harvard.edu/abs/1979ApJ...229.419E>.
- D. C. Ellison, P. Slane, D. J. Patnaude, and A. M. Bykov. Core-collapse Model of Broadband Emission from SNR RX J1713.7-3946 with Thermal X-Rays and Gamma Rays from Escaping Cosmic Rays. *ApJ*, 744:39, January 2012. doi: 10.1088/0004-637X/744/1/39.
- T. Enßlin, C. Pfrommer, F. Miniati, and K. Subramanian. Cosmic ray transport in galaxy clusters: implications for radio halos, gamma-ray signatures, and cool core heating. *A&A*, 527:A99, March 2011. doi: 10.1051/0004-6361/201015652.
- T. A. Enßlin, P. L. Biermann, U. Klein, and S. Kohle. Cluster radio relics as a tracer of shock waves of the large-scale structure formation. *A&A*, 332:395–409, April 1998.
- T. A. Enßlin, C. Pfrommer, V. Springel, and M. Jubelgas. Cosmic ray physics in calculations of cosmological structure formation. *A&A*, 473:41–57, October 2007. doi: 10.1051/0004-6361:20065294.
- J. E. Everett et al. The milky way’s kiloparsec-scale wind: A hybrid cosmic-ray and thermally driven outflow. *ApJ*, 674:258–270, February 2008. doi: 10.1086/524766. URL <http://adsabs.harvard.edu/abs/2008ApJ...674..258E>.
- C. Federrath. Magnetic field amplification in turbulent astrophysical plasmas. *Journal of Plasma Physics*, 82(6):535820601, December 2016. doi: 10.1017/S0022377816001069.
- E. Fermi. On the Origin of the Cosmic Radiation. *Physical Review*, 75:1169–1174, April 1949. doi: 10.1103/PhysRev.75.1169.
- Y. Fujita and Y. Ohira. Non-thermal emissions from cool cores heated by cosmic rays in galaxy clusters. *ApJ*, 746:53, February 2012. doi: 10.1088/0004-637X/746/1/53. URL <http://adsabs.harvard.edu/abs/2012ApJ...746...53F>.
- M. S. Fulbright and S. P. Reynolds. Bipolar supernova remnants and the obliquity dependence of shock acceleration. *ApJ*, 357:591, July 1990. doi: 10.1086/168947. URL <https://ui.adsabs.harvard.edu/abs/1990ApJ...357..591F>.
- T. K. Gaisser, R. Engel, and E. Resconi. *Cosmic rays and particle physics*. Cambridge University Press, Cambridge, second edition edition, 2016. ISBN 978-0-521-01646-9 and 0-521-01646-0. Includes bibliographical references and index.

## Bibliography

---

- F. F. Gardner and D. K. Milne. The supernova of A.D. 1006. *AJ*, 70:754, November 1965. doi: 10.1086/109813.
- S. Genel et al. Following the flow: tracer particles in astrophysical fluid simulations. *MNRAS*, 435:1426–1442, October 2013. doi: 10.1093/mnras/stt1383.
- J. Giacalone and J. R. Jokipii. Magnetic Field Amplification by Shocks in Turbulent Fluids. *ApJ*, 663(1):L41–L44, Jul 2007. doi: 10.1086/519994.
- P. Girichidis et al. Launching cosmic-ray-driven outflows from the magnetized interstellar medium. *ApJ*, 816:L19, January 2016. doi: 10.3847/2041-8205/816/2/L19. URL <http://adsabs.harvard.edu/abs/2016ApJ...816L..19G>.
- P. Girichidis, T. Naab, M. Hanasz, and S. Walch. Cooler and smoother - the impact of cosmic rays on the phase structure of galactic outflows. *MNRAS*, 479:3042–3067, September 2018. doi: 10.1093/mnras/sty1653. URL <http://adsabs.harvard.edu/abs/2018MNRAS.479.3042G>.
- P. Girichidis, C. Pfrommer, M. Hanasz, and T. Naab. Spectrally resolved cosmic ray hydrodynamics - I. Spectral scheme. *Monthly Notices of the Royal Astronomical Society*, 491:993–1007, January 2020. ISSN 0035-8711. doi: 10.1093/mnras/stz2961. URL <http://adsabs.harvard.edu/abs/2020MNRAS.491..993G>.
- R. J. Gould. Energy loss of fast electrons and positrons in a plasma. *Physica*, 60:145–154, July 1972a. doi: 10.1016/0031-8914(72)90227-3.
- R. J. Gould. Energy loss of a relativistic ion in a plasma. *Physica*, 58(3):379–383, April 1972b. doi: 10.1016/0031-8914(72)90159-0.
- R. J. Gould. Energy loss of relativistic electrons and positrons traversing cosmic matter. *ApJ*, 196:689–694, March 1975. doi: 10.1086/153457.
- F. Guo and S. P. Oh. Feedback heating by cosmic rays in clusters of galaxies. *MNRAS*, 384:251–266, February 2008. doi: 10.1111/j.1365-2966.2007.12692.x. URL <http://adsabs.harvard.edu/abs/2008MNRAS.384..251G>.
- X. Guo, L. Sironi, and R. Narayan. Non-thermal electron acceleration in low mach number collisionless shocks. i. particle energy spectra and acceleration mechanism. *ApJ*, 794:153, 2014a. ISSN 0004-637X. doi: 10.1088/0004-637X/794/2/153. URL <http://adsabs.harvard.edu/abs/2014ApJ...794..153G>.
- X. Guo, L. Sironi, and R. Narayan. Non-thermal electron acceleration in low mach number collisionless shocks. II. firehose-mediated fermi acceleration and its dependence on pre-shock conditions. *ApJ*, 797:47, 2014b. ISSN 0004-637X. doi: 10.1088/0004-637X/797/1/47. URL <http://adsabs.harvard.edu/abs/2014ApJ...797...47G>.

- M. Hanasz and H. Lesch. Incorporation of cosmic ray transport into the zeus mhd code. application for studies of parker instability in the ism. *A&A*, 412:331–339, December 2003. doi: 10.1051/0004-6361:20031433. URL <http://adsabs.harvard.edu/abs/2003A%26A...412...331H>.
- M. Hanasz, K. Kowalik, D. Wóltański, and R. Pawłaszek. The piernik mhd code - a multi-fluid, non-ideal extension of the relaxing-tvd scheme (i). In K. Goździewski, A. Niedzielski, and J. Schneider, editors, *EAS Publications Series*, volume 42 of *EAS Publications Series*, pages 275–280, April 2010. doi: 10.1051/eas/1042029. URL <http://adsabs.harvard.edu/abs/2010EAS...42...275H>.
- M. Hanasz et al. Cosmic Rays Can Drive Strong Outflows from Gas-rich High-redshift Disk Galaxies. *The Astrophysical Journal Letters*, 777:L38, November 2013. ISSN 0004-637X. doi: 10.1088/2041-8205/777/2/L38. URL <http://adsabs.harvard.edu/abs/2013ApJ...777L..38H>.
- A. Hanusch, T. V. Liseykina, M. Malkov, and F. Aharonian. Steepening of Cosmic-Ray Spectra in Shocks with Varying Magnetic Field Direction. *ApJ*, 885(1):11, November 2019. doi: 10.3847/1538-4357/ab426d.
- V. Heesen, R.-J. Dettmar, M. Krause, R. Beck, and Y. Stein. Advective and diffusive cosmic ray transport in galactic haloes. *MNRAS*, 458:332–353, 2016. ISSN 0035-8711. doi: 10.1093/mnras/stw360. URL <http://adsabs.harvard.edu/abs/2016MNRAS.458..332H>.
- E. A. Helder et al. Observational Signatures of Particle Acceleration in Supernova Remnants. *Space Sci. Rev.*, 173:369–431, November 2012. doi: 10.1007/s11214-012-9919-8.
- V. F. Hess. Über Beobachtungen der durchdringenden Strahlung bei sieben Freiballonfahrten. *Phys.Z.*, 13:1084–1091, 1912. URL <https://inspirehep.net/literature/1623161>.
- A. M. Hillas. The origin of ultra-high-energy cosmic rays. *Annual Review of Astronomy and Astrophysics*, 22:425–444, January 1984. doi: 10.1146/annurev.aa.22.090184.002233. URL <https://ui.adsabs.harvard.edu/abs/1984ARA&A...22...425H>.
- K. Hirata et al. Observation of a neutrino burst from the supernova sn1987a. *Phys. Rev. Lett.*, 58:1490–1493, Apr 1987. doi: 10.1103/PhysRevLett.58.1490. URL <https://link.aps.org/doi/10.1103/PhysRevLett.58.1490>.
- I. Iben, Jr. and A. V. Tutukov. Supernovae of type I as end products of the evolution of binaries with components of moderate initial mass (M not greater than about 9 solar masses). *The Astrophysical Journal Supplement Series*, 54:335–372, February 1984.

- ISSN 0067-0049. doi: 10.1086/190932. URL <http://adsabs.harvard.edu/abs/1984ApJS...54..335I>.
- S. Jacob and C. Pfrommer. Cosmic ray heating in cool core clusters - i. diversity of steady state solutions. *MNRAS*, 467:1449–1477, May 2017a. doi: 10.1093/mnras/stx131. URL <http://adsabs.harvard.edu/abs/2017MNRAS.467.1449J>.
- S. Jacob and C. Pfrommer. Cosmic ray heating in cool core clusters - ii. self-regulation cycle and non-thermal emission. *MNRAS*, 467:1478–1495, May 2017b. doi: 10.1093/mnras/stx132. URL <http://adsabs.harvard.edu/abs/2017MNRAS.467.1478J>.
- S. Jacob, R. Pakmor, C. M. Simpson, V. Springel, and C. Pfrommer. The dependence of cosmic ray-driven galactic winds on halo mass. *MNRAS*, 475:570–584, March 2018. doi: 10.1093/mnras/stx3221. URL <http://adsabs.harvard.edu/abs/2018MNRAS.475..570J>.
- W. J. Jaffe. Origin and transport of electrons in the halo radio source in the coma cluster. *ApJ*, 212:1–7, February 1977. doi: 10.1086/155011. URL <http://adsabs.harvard.edu/abs/1977ApJ...212....1J>.
- S. Ji, S. P. Oh, M. Ruszkowski, and M. Markevitch. The efficiency of magnetic field amplification at shocks by turbulence. *MNRAS*, 463(4):3989–4003, Dec 2016. doi: 10.1093/mnras/stw2320.
- M. Jubelgas, V. Springel, T. Enßlin, and C. Pfrommer. Cosmic ray feedback in hydrodynamical simulations of galaxy formation. *A&A*, 481:33–63, April 2008. doi: 10.1051/0004-6361:20065295. URL <http://adsabs.harvard.edu/abs/2008A%26A...481...33J>.
- B.-I. Jun and T. W. Jones. Radio Emission from a Young Supernova Remnant Interacting with an Interstellar Cloud: Magnetohydrodynamic Simulation with Relativistic Electrons. *The Astrophysical Journal*, 511:774–791, February 1999. ISSN 0004-637X. doi: 10.1086/306694. URL <http://adsabs.harvard.edu/abs/1999ApJ...511..774J>.
- E. Kafexhiu, F. Aharonian, A. M. Taylor, and G. S. Vila. Parametrization of gamma-ray production cross sections for p p interactions in a broad proton energy range from the kinematic threshold to PeV energies. *Phys. Rev. D*, 90(12):123014, December 2014. doi: 10.1103/PhysRevD.90.123014.
- H. Kang, D. Ryu, and J.-H. Ha. Electron preacceleration in weak quasi-perpendicular shocks in high-beta intracluster medium. *arXiv e-prints*, January 2019. URL <http://adsabs.harvard.edu/abs/2019arXiv190104173K>.

- H. Kang and D. Ryu. Re-acceleration of non-thermal particles at weak cosmological shock waves. *The Astrophysical Journal*, 734:18, 2011. ISSN 0004-637X. doi: 10.1088/0004-637X/734/1/18. URL <http://adsabs.harvard.edu/abs/2011ApJ...734...18K>.
- T. N. Kato. Particle Acceleration and Wave Excitation in Quasi-parallel High-Mach-number Collisionless Shocks: Particle-in-cell Simulation. *The Astrophysical Journal*, 802:115, April 2015. ISSN 0004-637X. doi: 10.1088/0004-637X/802/2/115. URL <http://adsabs.harvard.edu/abs/2015ApJ...802..115K>.
- S. Katsuda. Supernova of 1006 (g327.6+14.6). In A. W. Alsabti and P. Murdin, editors, *Handbook of Supernovae*, pages 63–81. Springer International Publishing, Cham, 2017. doi: 10.1007/978-3-319-21846-5\_45.
- S. Katsuda et al. Steady X-ray Synchrotron Emission in the Northeastern Limb of SN 1006. *The Astrophysical Journal*, 723:383–392, November 2010. ISSN 0004-637X. doi: 10.1088/0004-637X/723/1/383. URL <http://adsabs.harvard.edu/abs/2010ApJ...723..383K>.
- U. Keshet, B. Katz, A. Spitkovsky, and E. Waxman. Magnetic Field Evolution in Relativistic Unmagnetized Collisionless Shocks. *The Astrophysical Journal Letters*, 693:L127–L130, March 2009. ISSN 0004-637X. doi: 10.1088/0004-637X/693/2/L127. URL <http://adsabs.harvard.edu/abs/2009ApJ...693L.127K>.
- C.-G. Kim and E. C. Ostriker. Vertical Equilibrium, Energetics, and Star Formation Rates in Magnetized Galactic Disks Regulated by Momentum Feedback from Supernovae. *ApJ*, 815(1):67, December 2015. doi: 10.1088/0004-637X/815/1/67.
- J. G. Kirk, R. Schlickeiser, and P. Schneider. Cosmic-ray transport in accelerating flows. *ApJ*, 328:269–274, May 1988. doi: 10.1086/166290. URL <http://adsabs.harvard.edu/abs/1988ApJ...328..269K>.
- J. G. Kirk, P. Duffy, and Y. A. Gallant. Stochastic particle acceleration at shocks in the presence of braided magnetic fields. *A&A*, 314:1010–1016, October 1996.
- H. W. Koch and J. W. Motz. Bremsstrahlung cross-section formulas and related data. *Reviews of Modern Physics*, 31:920–955, 1959. ISSN 0034-6861. doi: 10.1103/RevModPhys.31.920. URL <http://adsabs.harvard.edu/abs/1959RvMP...31..920K>.
- K. Koyama et al. Evidence for shock acceleration of high-energy electrons in the supernova remnant SN1006. *Nature*, 378:255–258, November 1995. ISSN 0028-0836. doi: 10.1038/378255a0. URL <http://adsabs.harvard.edu/abs/1995Natur.378..255K>.

## Bibliography

---

- G. F. Krymskii. A regular mechanism for the acceleration of charged particles on the front of a shock wave. *Soviet Physics Doklady*, 22:327, June 1977.
- R. Kulsrud and W. P. Pearce. The effect of wave-particle interactions on the propagation of cosmic rays. *ApJ*, 156:445, May 1969. doi: 10.1086/149981. URL <http://adsabs.harvard.edu/abs/1969ApJ...156..445K>.
- P. Lax and B. Wendroff. Systems of conservation laws. *Communications on Pure and Applied Mathematics*, 13(2):217–237, 1960. doi: 10.1002/cpa.3160130205. URL <https://onlinelibrary.wiley.com/doi/abs/10.1002/cpa.3160130205>.
- A. Lazarian and H. Yan. Superdiffusion of Cosmic Rays: Implications for Cosmic Ray Acceleration. *ApJ*, 784(1):38, March 2014. doi: 10.1088/0004-637X/784/1/38.
- R. J. LeVeque, D. Mihalas, E. Dorfi, and E. Müller. Computational methods for astrophysical fluid flow. In O. Steiner and A. Gautschi, editors, *Computational methods for astrophysical fluid flow*, Lecture notes / Swiss Society for Astrophysics and Astronomy. Saas Fee Advanced Course <27, 1997, Les Diablerets> and Schweizerische Gesellschaft für Astrophysik und Astronomie, Springer-Verlag Berlin Heidelberg, 1998. ISBN 978-3-540-64448-4. doi: 10.1007/3-540-31632-9.
- J.-T. Li et al. Spatially Resolved Broadband Synchrotron Emission from the Nonthermal Limbs of SN1006. *ApJ*, 864(1):85, September 2018. doi: 10.3847/1538-4357/aad598.
- A. S. Lipatov. *The hybrid multiscale simulation technology: an introduction with application to astrophysical and laboratory plasmas*. Springer-Verlag Berlin Heidelberg, 2002.
- S. Lloyd. Least squares quantization in pcm. *IEEE Transactions on Information Theory*, 28(2):129–137, 1982.
- M. Loewenstein, E. G. Zweibel, and M. C. Begelman. Cosmic-ray heating of cooling flows - a critical analysis. *ApJ*, 377:392–402, August 1991. doi: 10.1086/170369. URL <http://adsabs.harvard.edu/abs/1991ApJ...377..392L>.
- M. Longair. *High energy astrophysics*. Cambridge Univ. Press, Cambridge [u.a.], 3. ed. edition, 2012. ISBN 978-0-521-75618-1.
- K. Maguire. *Type Ia Supernovae*, page 293. Springer International Publishing, 2017. doi: 10.1007/978-3-319-21846-5\_36.
- M. Malkov and F. Aharonian. Cosmic ray spectra in supernova remnants - i. loss-free self-similar solution. *arXiv e-prints*, January 2019. URL <https://ui.adsabs.harvard.edu/abs/2019arXiv190101284M>.

- K. Mannheim and R. Schlickeiser. Interactions of cosmic ray nuclei. *A&A*, 286:983–996, 1994. ISSN 0004-6361. URL <http://adsabs.harvard.edu/abs/1994A%26A...286..983M>.
- B. R. McNamara and P. E. J. Nulsen. Heating hot atmospheres with active galactic nuclei. *ARA&A*, 45:117–175, September 2007. doi: 10.1146/annurev.astro.45.051806.110625. URL <http://adsabs.harvard.edu/abs/2007ARA%26A...45..117M>.
- P. Mertsch and V. Petrosian. Fermi bubbles from stochastic acceleration of electrons in a galactic outflow. *A&A*, 622:A203, February 2019. doi: 10.1051/0004-6361/201833999. URL <https://ui.adsabs.harvard.edu/abs/2019A%26A...622A.203M>.
- M. Miceli et al. Xmm-newton evidence of shocked ism in sn 1006: indications of hadronic acceleration. *A&A*, 546:A66, October 2012. doi: 10.1051/0004-6361/201219766. URL <https://ui.adsabs.harvard.edu/abs/2012A&A...546A..66M>.
- M. Miceli et al. Shock-Cloud Interaction and Particle Acceleration in the Southwestern Limb of SN 1006. *The Astrophysical Journal Letters*, 782:L33, February 2014. ISSN 0004-637X. doi: 10.1088/2041-8205/782/2/L33. URL <http://adsabs.harvard.edu/abs/2014ApJ...782L..33M>.
- M. Miceli et al. Modeling the shock-cloud interaction in SN 1006: Unveiling the origin of nonthermal X-ray and  $\gamma$ -ray emission. *A&A*, 593:A26, August 2016. doi: 10.1051/0004-6361/201628725.
- A. Mignone, G. Bodo, B. Vaidya, and G. Mattia. A particle module for the pluto code. i. an implementation of the mhd-pic equations. *ApJ*, 859:13, May 2018. doi: 10.3847/1538-4357/aabccd. URL <http://adsabs.harvard.edu/abs/2018ApJ...859...13M>.
- F. Miniati. Cosmocr: A numerical code for cosmic ray studies in computational cosmology. *Computer Physics Communications*, 141:17–38, November 2001. doi: 10.1016/S0010-4655(01)00293-4.
- F. Miniati. Numerical modelling of gamma radiation from galaxy clusters. *MNRAS*, 342:1009–1020, July 2003. doi: 10.1046/j.1365-8711.2003.06647.x. URL <http://adsabs.harvard.edu/abs/2003MNRAS.342.1009M>.
- F. Miniati, T. W. Jones, H. Kang, and D. Ryu. Cosmic-ray electrons in groups and clusters of galaxies: Primary and secondary populations from a numerical cosmological simulation. *ApJ*, 562:233–253, November 2001. doi: 10.1086/323434. URL <http://adsabs.harvard.edu/abs/2001ApJ...562..233M>.
- G. Morlino, E. Amato, P. Blasi, and D. Caprioli. Spatial structure of X-ray filaments in SN 1006. *MNRAS*, 405(1):L21–L25, Jun 2010. doi: 10.1111/j.1745-3933.2010.00851.x.

- T. Naab and J. P. Ostriker. Theoretical Challenges in Galaxy Formation. *ARA&A*, 55(1): 59–109, August 2017. doi: 10.1146/annurev-astro-081913-040019.
- K. Nomoto. Accreting white dwarf models for type I supernovae. I - Presupernova evolution and triggering mechanisms. *The Astrophysical Journal*, 253:798–810, February 1982. ISSN 0004-637X. doi: 10.1086/159682. URL <http://adsabs.harvard.edu/abs/1982ApJ...253..798N>.
- S. M. Osipov, A. M. Bykov, and D. C. Ellison. Monte Carlo modelling of particle acceleration in collisionless shocks with effective mean electric field. In *Journal of Physics Conference Series*, volume 1400 of *Journal of Physics Conference Series*, page 022004, November 2019. doi: 10.1088/1742-6596/1400/2/022004.
- M. Pais, C. Pfrommer, K. Ehlert, and R. Pakmor. The effect of cosmic ray acceleration on supernova blast wave dynamics. *MNRAS*, 478:5278–5295, August 2018a. doi: 10.1093/mnras/sty1410. URL <http://adsabs.harvard.edu/abs/2018MNRAS.478.5278P>.
- M. Pais, C. Pfrommer, K. Ehlert, and M. Werhahn. Constraining the coherence scale of the interstellar magnetic field using tev gamma-ray observations of supernova remnants. *arXiv e-prints*, May 2018b. URL <https://ui.adsabs.harvard.edu/abs/2018arXiv180503216P>.
- R. Pakmor and V. Springel. Simulations of magnetic fields in isolated disc galaxies. *MNRAS*, 432:176–193, June 2013. doi: 10.1093/mnras/stt428. URL <http://adsabs.harvard.edu/abs/2013MNRAS.432..176P>.
- R. Pakmor, C. Pfrommer, C. M. Simpson, R. Kannan, and V. Springel. Semi-implicit anisotropic cosmic ray transport on an unstructured moving mesh. *MNRAS*, 462:2603–2616, November 2016a. doi: 10.1093/mnras/stw1761.
- R. Pakmor, C. Pfrommer, C. M. Simpson, and V. Springel. Galactic winds driven by isotropic and anisotropic cosmic-ray diffusion in disk galaxies. *ApJ*, 824:L30, June 2016b. doi: 10.3847/2041-8205/824/2/L30.
- R. Pakmor et al. Improving the convergence properties of the moving-mesh code arepo. *MNRAS*, 455:1134–1143, January 2016c. doi: 10.1093/mnras/stv2380. URL <http://adsabs.harvard.edu/abs/2016MNRAS.455.1134P>.
- R. Pakmor et al. Sub-luminous type Ia supernovae from the mergers of equal-mass white dwarfs with mass  $\sim 0.9M_{\text{solar}}$ . *Nature*, 463(7277):61–64, January 2010. doi: 10.1038/nature08642.
- J. Park, D. Caprioli, and A. Spitkovsky. Simultaneous acceleration of protons and electrons at nonrelativistic quasiparallel collisionless shocks. *Physical Review Letters*, 114:085003, 2015. ISSN 0031-9007. doi: 10.1103/PhysRevLett.114.085003. URL <http://adsabs.harvard.edu/abs/2015PhRvL.114h5003P>.

- V. Petrosian. On the nonthermal emission and acceleration of electrons in coma and other clusters of galaxies. *ApJ*, 557:560–572, August 2001. doi: 10.1086/321557.
- V. Petrosian. Stochastic Acceleration by Turbulence. *Space Sci. Rev.*, 173:535–556, November 2012. doi: 10.1007/s11214-012-9900-6.
- O. Petruk et al. Aspect angle for interstellar magnetic field in sn 1006. *MNRAS*, 393(3):1034–1040, March 2009. doi: 10.1111/j.1365-2966.2008.14251.x. URL <https://ui.adsabs.harvard.edu/abs/2009MNRAS.393.1034P>.
- O. Petruk, V. Beshley, F. Bocchino, M. Miceli, and S. Orlando. Observational constraints on the modelling of SN 1006. *Monthly Notices of the Royal Astronomical Society*, 413:1643–1656, May 2011. ISSN 0035-8711. doi: 10.1111/j.1365-2966.2011.18237.x. URL <http://adsabs.harvard.edu/abs/2011MNRAS.413.1643P>.
- C. Pfrommer. Toward a comprehensive model for feedback by active galactic nuclei: New insights from m87 observations by lofar, fermi, and h.e.s.s. *ApJ*, 779:10, December 2013. doi: 10.1088/0004-637X/779/1/10. URL <http://adsabs.harvard.edu/abs/2013ApJ...779...10P>.
- C. Pfrommer, V. Springel, T. A. Enßlin, and M. Jubelgas. Detecting shock waves in cosmological smoothed particle hydrodynamics simulations. *MNRAS*, 367:113–131, March 2006. doi: 10.1111/j.1365-2966.2005.09953.x. URL <http://adsabs.harvard.edu/abs/2006MNRAS.367..113P>.
- C. Pfrommer, T. A. Enßlin, and V. Springel. Simulating cosmic rays in clusters of galaxies - II. A unified scheme for radio haloes and relics with predictions of the  $\gamma$ -ray emission. *MNRAS*, 385:1211–1241, April 2008. doi: 10.1111/j.1365-2966.2008.12956.x.
- C. Pfrommer, R. Pakmor, K. Schaal, C. M. Simpson, and V. Springel. Simulating cosmic ray physics on a moving mesh. *MNRAS*, 465:4500–4529, March 2017a. doi: 10.1093/mnras/stw2941.
- C. Pfrommer, R. Pakmor, C. M. Simpson, and V. Springel. Simulating gamma-ray emission in star-forming galaxies. *ApJ*, 847:L13, October 2017b. doi: 10.3847/2041-8213/aa8bb1. URL <http://adsabs.harvard.edu/abs/2017ApJ...847L..13P>.
- C. Pfrommer. *On the role of cosmic rays in clusters of galaxies*. PhD thesis, Fakultät für Physik der Ludwig-Maximilians-Universität München, 2005. URL <http://nbn-resolving.de/urn:nbn:de:bvb:19-46051>.
- A. Pinzke and C. Pfrommer. Simulating the gamma-ray emission from galaxy clusters: a universal cosmic ray spectrum and spatial distribution. *Mon. Not. Roy. Astron. Soc.*, 409:449, 2010. doi: 10.1111/j.1365-2966.2010.17328.x.

## Bibliography

---

- A. Pinzke, S. P. Oh, and C. Pfrommer. Giant radio relics in galaxy clusters: reacceleration of fossil relativistic electrons? *Mon. Not. Roy. Astron. Soc.*, 435:1061, 2013. doi: 10.1093/mnras/stt1308.
- A. Pinzke, S. P. Oh, and C. Pfrommer. Turbulence and particle acceleration in giant radio haloes: the origin of seed electrons. *MNRAS*, 465:4800–4816, 2017. ISSN 0035-8711. doi: 10.1093/mnras/stw3024. URL <http://adsabs.harvard.edu/abs/2017MNRAS.465.4800P>.
- M. Pohl, H. Yan, and A. Lazarian. Magnetically Limited X-Ray Filaments in Young Supernova Remnants. *The Astrophysical Journal Letters*, 626:L101–L104, June 2005. ISSN 0004-637X. doi: 10.1086/431902. URL <http://adsabs.harvard.edu/abs/2005ApJ...626L.101P>.
- T. A. Porter and A. W. Strong. A new estimate of the galactic interstellar radiation field between 0.1 $\mu$ m and 1000 $\mu$ m. *International Cosmic Ray Conference*, 4:77, 2005. URL <http://adsabs.harvard.edu/abs/2005ICRC....4...77P>.
- T. A. Porter, I. V. Moskalenko, A. W. Strong, E. Orlando, and L. Bouchet. Inverse compton origin of the hard x-ray and soft gamma-ray emission from the galactic ridge. *ApJ*, 682:400–407, July 2008. doi: 10.1086/589615. URL <http://adsabs.harvard.edu/abs/2008ApJ...682..400P>.
- W. H. Press, S. A. Teukolsky, W. T. Vetterling, and B. P. Flannery, editors. *Numerical recipes*. Cambridge Univ. Press, Cambridge [u.a.], 3. ed. edition, 2007. ISBN 978-0-521-88407-5 and 978-0-521-70685-8. Includes bibliographical references and index. - This printing is corrected to software version 3.0.
- J. E. Pringle, A. R. King, and J. E. Pringle. *Astrophysical flows*. Cambridge University Press, Cambridge [u.a.], 2007. ISBN 0-521-86936-6 and 978-0-521-86936-2.
- V. S. Ptuskin. Cosmic-ray acceleration by long-wave turbulence. *Soviet Astronomy Letters*, 14:255, March 1988. URL <http://adsabs.harvard.edu/abs/1988SvAL...14..255P>.
- V. S. Ptuskin, H. J. Voelk, V. N. Zirakashvili, and D. Breitschwerdt. Transport of relativistic nucleons in a galactic wind driven by cosmic rays. *A&A*, 321:434–443, May 1997. URL <http://adsabs.harvard.edu/abs/1997A%26A...321..434P>.
- O. Regev, O. M. Umurhan, and P. A. Yecko. *Modern Fluid Dynamics for Physics and Astrophysics*. Graduate Texts in Physics. Springer, New York, NY, 1st ed. 2016 edition, 2016. ISBN 978-1-4939-3164-4. doi: 10.1007/978-1-4939-3164-4. URL <http://dx.doi.org/10.1007/978-1-4939-3164-4>.

- S. M. Ressler et al. Magnetic Field Amplification in the Thin X-Ray Rims of SN 1006. *The Astrophysical Journal*, 790:85, August 2014. ISSN 0004-637X. doi: 10.1088/0004-637X/790/2/85. URL <http://adsabs.harvard.edu/abs/2014ApJ...790...85R>.
- B. Reville and A. R. Bell. Universal behaviour of shock precursors in the presence of efficient cosmic ray acceleration. *MNRAS*, 430(4):2873–2884, April 2013. doi: 10.1093/mnras/stt100.
- S. P. Reynolds. Supernova remnants at high energy. *ARA&A*, 46:89–126, September 2008. doi: 10.1146/annurev.astro.46.060407.145237.
- S. P. Reynolds. Synchrotron models for x-rays from the supernova remnant sn 1006. *ApJ*, 459:L13, March 1996. doi: 10.1086/309936. URL <https://ui.adsabs.harvard.edu/abs/1996ApJ...459L..13R>.
- S. P. Reynolds. *Dynamical Evolution and Radiative Processes of Supernova Remnants*, page 1981. Springer International Publishing, 2017. doi: 10.1007/978-3-319-21846-5\_89.
- E. M. Reynoso, J. P. Hughes, and D. A. Moffett. On the Radio Polarization Signature of Efficient and Inefficient Particle Acceleration in Supernova Remnant SN 1006. *AJ*, 145(4):104, Apr 2013. doi: 10.1088/0004-6256/145/4/104.
- M. A. Riquelme and A. Spitkovsky. Electron injection by whistler waves in non-relativistic shocks. *ApJ*, 733:63, May 2011. doi: 10.1088/0004-637X/733/1/63. URL <http://adsabs.harvard.edu/abs/2011ApJ...733...63R>.
- R. Rothenflug et al. Geometry of the non-thermal emission in sn 1006. azimuthal variations of cosmic-ray acceleration. *A&A*, 425:121–131, October 2004. doi: 10.1051/0004-6361:20047104. URL <https://ui.adsabs.harvard.edu/abs/2004A&A...425..121R>.
- M. Ruszkowski, H.-Y. K. Yang, and C. S. Reynolds. Cosmic-ray feedback heating of the intracluster medium. *ApJ*, 844:13, July 2017a. doi: 10.3847/1538-4357/aa79f8. URL <http://adsabs.harvard.edu/abs/2017ApJ...844...13R>.
- M. Ruszkowski, H.-Y. K. Yang, and E. Zweibel. Global simulations of galactic winds including cosmic-ray streaming. *ApJ*, 834:208, January 2017b. doi: 10.3847/1538-4357/834/2/208. URL <http://adsabs.harvard.edu/abs/2017ApJ...834..208R>.
- G. B. Rybicki and A. P. Lightman. *Radiative Processes in Astrophysics*. Wiley-VCH, June 1986. ISBN 0-471-82759-2.

- D. Ryu, H. Kang, E. Hallman, and T. W. Jones. Cosmological shock waves and their role in the large-scale structure of the universe. *ApJ*, 593:599–610, August 2003. doi: 10.1086/376723. URL <http://adsabs.harvard.edu/abs/2003ApJ...593..599R>.
- M. Salem and G. L. Bryan. Cosmic ray driven outflows in global galaxy disc models. *MNRAS*, 437:3312–3330, February 2014. doi: 10.1093/mnras/stt2121.
- S. Samui, K. Subramanian, and R. Srianand. Efficient cold outflows driven by cosmic rays in high-redshift galaxies and their global effects on the igm. *MNRAS*, 476:1680–1695, May 2018. doi: 10.1093/mnras/sty287. URL <http://adsabs.harvard.edu/abs/2018MNRAS.476.1680S>.
- C. L. Sarazin. The Energy Spectrum of Primary Cosmic-Ray Electrons in Clusters of Galaxies and Inverse Compton Emission. *ApJ*, 520:529–547, August 1999. doi: 10.1086/307501.
- K. Schaal and V. Springel. Shock finding on a moving mesh - i. shock statistics in non-radiative cosmological simulations. *MNRAS*, 446:3992–4007, February 2015. doi: 10.1093/mnras/stu2386.
- A. A. Schekochihin, S. C. Cowley, S. F. Taylor, J. L. Maron, and J. C. McWilliams. Simulations of the Small-Scale Turbulent Dynamo. *ApJ*, 612(1):276–307, September 2004. doi: 10.1086/422547.
- R. Schlickeiser. Cosmic-ray transport and acceleration. i - derivation of the kinetic equation and application to cosmic rays in static cold media. *ApJ*, 336:243–293, January 1989a. doi: 10.1086/167009. URL <http://adsabs.harvard.edu/abs/1989ApJ...336..243S>.
- R. Schlickeiser. Cosmic-ray transport and acceleration. ii. cosmic rays in moving cold media with application to diffusive shock wave acceleration. *ApJ*, 336:264, January 1989b. doi: 10.1086/167010. URL <http://adsabs.harvard.edu/abs/1989ApJ...336..264S>.
- R. Schlickeiser, A. Sievers, and H. Thiemann. The diffuse radio emission from the coma cluster. *A&A*, 182:21–35, August 1987. URL <http://adsabs.harvard.edu/abs/1987A%26A...182...21S>.
- R. Schlickeiser. *Cosmic Ray Astrophysics*. Astronomy and astrophysics library. Springer, Berlin ; Heidelberg [u.a.], 2002. ISBN 3-540-66465-3 and 978-3-540-66465-9.
- E. M. Schneiter, P. F. Velázquez, E. M. Reynoso, A. Esquivel, and F. De Colle. 3d mhd simulation of polarized emission in sn 1006. *MNRAS*, 449(1):88–93, May 2015. doi: 10.1093/mnras/stv279. URL <https://ui.adsabs.harvard.edu/abs/2015MNRAS.449...88S>.

- E. M. Schneiter, P. F. Velázquez, E. M. Reynoso, and F. de Colle. An mhd study of sn 1006 and determination of the ambient magnetic field direction. *MNRAS*, 408 (1):430–435, October 2010. doi: 10.1111/j.1365-2966.2010.17125.x. URL <https://ui.adsabs.harvard.edu/abs/2010MNRAS.408..430S>.
- L. I. Sedov. *Similarity and Dimensional Methods in Mechanics*. Academic Press, 1959. ISBN 978-1-4832-0088-0. URL <http://adsabs.harvard.edu/abs/1959sdmm.book.....S>.
- M. Selig, V. Vacca, N. Oppermann, and T. A. Enßlin. The denoised, deconvolved, and decomposed fermi  $\gamma$ -ray sky. an application of the d<sup>3</sup>po algorithm. *A&A*, 581:A126, September 2015. doi: 10.1051/0004-6361/201425172.
- F. H. Shu. *The physics of astrophysics. Volume II: Gas dynamics*. Univ. Science Books, Mill Valley, Calif., 1992. ISBN 0-935702-65-2 and 978-0-935702-65-1.
- C. M. Simpson et al. The role of cosmic-ray pressure in accelerating galactic outflows. *ApJ*, 827:L29, August 2016. doi: 10.3847/2041-8205/827/2/L29. URL <http://adsabs.harvard.edu/abs/2016ApJ...827L..29S>.
- J. Skilling. Cosmic ray streaming. i - effect of alfvén waves on particles. *MNRAS*, 172:557–566, 1975. ISSN 0035-8711. doi: 10.1093/mnras/172.3.557. URL <http://adsabs.harvard.edu/abs/1975MNRAS.172..557S>.
- G. A. Sod. A survey of several finite difference methods for systems of nonlinear hyperbolic conservation laws. *Journal of Computational Physics*, 27:1–31, April 1978. doi: 10.1016/0021-9991(78)90023-2. URL <http://adsabs.harvard.edu/abs/1978JCoPh..27....1S>.
- V. Springel. E pur si muove: Galilean-invariant cosmological hydrodynamical simulations on a moving mesh. *Mon. Not. Roy. Astron. Soc.*, 401:791, 2010. doi: 10.1111/j.1365-2966.2009.15715.x.
- M. Steffen. A simple method for monotonic interpolation in one dimension. *A&A*, 239:443, November 1990. URL <http://adsabs.harvard.edu/abs/1990A%26A..239..443S>.
- K. Stycz. *VHE Gamma-ray sources at the resolution limit of H.E.S.S.* PhD thesis, Humboldt-Universität zu Berlin, Mathematisch-Naturwissenschaftliche Fakultät, 2016.
- M. Su, T. R. Slatyer, and D. P. Finkbeiner. Giant gamma-ray bubbles from fermi-lat: Active galactic nucleus activity or bipolar galactic wind? *ApJ*, 724:1044–1082, December 2010. doi: 10.1088/0004-637X/724/2/1044.

- I. Sushch, R. Brose, and M. Pohl. Modeling of the spatially resolved nonthermal emission from the Vela Jr. supernova remnant. *Astronomy and Astrophysics*, 618:A155, October 2018. ISSN 0004-6361. doi: 10.1051/0004-6361/201832879. URL <http://adsabs.harvard.edu/abs/2018A%26A...618A..155S>.
- M. Takamoto and J. G. Kirk. Rapid Cosmic-ray Acceleration at Perpendicular Shocks in Supernova Remnants. *ApJ*, 809(1):29, August 2015. doi: 10.1088/0004-637X/809/1/29.
- T. Tanaka et al. Gamma-Ray Observations of the Supernova Remnant RX J0852.0-4622 with the Fermi Large Area Telescope. *The Astrophysical Journal Letters*, 740:L51, October 2011. ISSN 0004-637X. doi: 10.1088/2041-8205/740/2/L51. URL <http://adsabs.harvard.edu/abs/2011ApJ...740L..51T>.
- G. Taylor. The formation of a blast wave by a very intense explosion. i. theoretical discussion. *Proceedings of the Royal Society of London Series A*, 201:159–174, March 1950. doi: 10.1098/rspa.1950.0049. URL <http://adsabs.harvard.edu/abs/1950RSPSA.201..159T>.
- T. Thomas and C. Pfrommer. Cosmic-ray hydrodynamics: Alfvén-wave regulated transport of cosmic rays. *MNRAS*, 485(3):2977–3008, May 2019. doi: 10.1093/mnras/stz263.
- Y. Uchiyama, F. A. Aharonian, T. Tanaka, T. Takahashi, and Y. Maeda. Extremely fast acceleration of cosmic rays in a supernova remnant. *Nature*, 449:576–578, October 2007. doi: 10.1038/nature06210. URL <https://ui.adsabs.harvard.edu/abs/2007Natur.449..576U>.
- M. Uhlig et al. Galactic winds driven by cosmic ray streaming. *MNRAS*, 423:2374–2396, July 2012. doi: 10.1111/j.1365-2966.2012.21045.x.
- B. Vaidya, A. Mignone, G. Bodo, P. Rossi, and S. Massaglia. A particle module for the pluto code. ii. hybrid framework for modeling nonthermal emission from relativistic magnetized flows. *ApJ*, 865:144, October 2018. doi: 10.3847/1538-4357/aadd17. URL <http://adsabs.harvard.edu/abs/2018ApJ...865..144V>.
- B. van Leer. Towards the ultimate conservative difference scheme. iv. a new approach to numerical convection. *Journal of Computational Physics*, 23:276, March 1977. doi: 10.1016/0021-9991(77)90095-X. URL <http://adsabs.harvard.edu/abs/1977JCoPh..23..276V>.
- B. van Leer. Towards the Ultimate Conservative Difference Scheme. V. A Second-Order Sequel to Godunov’s Method. *Journal of Computational Physics*, 32(1):101–136, July 1979. doi: 10.1016/0021-9991(79)90145-1.

- 
- F. Vazza et al. Why are central radio relics so rare? *MNRAS*, 421:1868–1873, April 2012. doi: 10.1111/j.1365-2966.2011.20160.x. URL <http://adsabs.harvard.edu/abs/2012MNRAS.421.1868V>.
- H. J. Völk, E. G. Berezhko, and L. T. Ksenofontov. Variation of cosmic ray injection across supernova shocks. *A&A*, 409:563–571, October 2003. doi: 10.1051/0004-6361:20031082. URL <https://ui.adsabs.harvard.edu/abs/2003A&A...409..563V>.
- J. Wiener, S. P. Oh, and F. Guo. Cosmic ray streaming in clusters of galaxies. *MNRAS*, 434:2209–2228, September 2013. doi: 10.1093/mnras/stt1163.
- R. Willingale, R. G. West, J. P. Pye, and G. C. Stewart. ROSAT PSPC observations of the remnant of SN 1006. *Monthly Notices of the Royal Astronomical Society*, 278: 749–762, February 1996. ISSN 0035-8711. doi: 10.1093/mnras/278.3.749. URL <http://adsabs.harvard.edu/abs/1996MNRAS.278..749W>.
- P. F. Winkler and K. S. Long. X-Ray and Optical Imagery of the SN 1006 Supernova Remnant. *ApJ*, 491(2):829–838, Dec 1997. doi: 10.1086/304969.
- P. F. Winkler, G. Gupta, and K. S. Long. The SN 1006 Remnant: Optical Proper Motions, Deep Imaging, Distance, and Brightness at Maximum. *ApJ*, 585(1):324–335, March 2003. doi: 10.1086/345985.
- P. F. Winkler et al. The First Reported Infrared Emission from the SN 1006 Remnant. *ApJ*, 764(2):156, February 2013. doi: 10.1088/0004-637X/764/2/156.
- P. F. Winkler et al. A High-resolution X-Ray and Optical Study of SN 1006: Asymmetric Expansion and Small-scale Structure in a Type Ia Supernova Remnant. *ApJ*, 781(2):65, February 2014. doi: 10.1088/0004-637X/781/2/65.
- G. Winner, C. Pfrommer, P. Girichidis, and R. Pakmor. Evolution of cosmic ray electron spectra in magnetohydrodynamical simulations. *MNRAS*, 488(2):2235–2252, Sep 2019. doi: 10.1093/mnras/stz1792.
- G. Winner, C. Pfrommer, P. Girichidis, M. Werhahn, and M. Pais. Evolution and observational signatures of the cosmic ray electron spectrum in SN 1006. *arXiv e-prints*, 2006:arXiv:2006.06683, June 2020. URL <http://adsabs.harvard.edu/abs/2020arXiv200606683W>.
- Y. Xing, Z. Wang, X. Zhang, and Y. Chen. Fermi LAT detection of the supernova remnant SN 1006 revisited: The southwest limb. *PASJ*, 71(4):77, August 2019. doi: 10.1093/pasj/psz056.

- R. Xu, A. Spitkovsky, and D. Caprioli. Electron acceleration in non-relativistic quasi-perpendicular collisionless shocks. *arXiv e-prints*, art. arXiv:1908.07890, August 2019. URL <https://ui.adsabs.harvard.edu/abs/2019arXiv190807890X>.
- H.-Y. K. Yang and M. Ruszkowski. The Spatially Uniform Spectrum of the Fermi Bubbles: The Leptonic Active Galactic Nucleus Jet Scenario. *ApJ*, 850:2, November 2017. doi: 10.3847/1538-4357/aa9434.
- R.-z. Yang, E. Kafexhiu, and F. Aharonian. Exploring the shape of the  $\gamma$ -ray spectrum around the “ $\pi^0$ -bump”. *A&A*, 615:A108, Jul 2018. doi: 10.1051/0004-6361/201730908.
- G. P. Zank. *Transport Processes in Space Physics and Astrophysics*. Lecture Notes in Physics ; 877. Springer, New York, NY, 2014. ISBN 978-146-148-480-6.
- V. N. Zirakashvili and F. Aharonian. Analytical solutions for energy spectra of electrons accelerated by nonrelativistic shock-waves in shell type supernova remnants. *A&A*, 465: 695–702, April 2007. doi: 10.1051/0004-6361:20066494.
- V. N. Zirakashvili and V. S. Ptuskin. Role of the mean electric field in diffusive shock acceleration. *Bulletin of the Russian Academy of Sciences, Physics*, 79(3):316–318, March 2015. doi: 10.3103/S1062873815030466.
- V. N. Zirakashvili, D. Breitschwerdt, V. S. Ptuskin, and H. J. Voelk. Magnetohydrodynamic wind driven by cosmic rays in a rotating galaxy. *A&A*, 311:113–126, July 1996. URL <http://adsabs.harvard.edu/abs/1996A%26A...311..113Z>.
- E. G. Zweibel. The microphysics and macrophysics of cosmic rays. *Physics of Plasmas*, 20(5):055501, 2013. doi: <http://dx.doi.org/10.1063/1.4807033>. URL <http://scitation.aip.org/content/aip/journal/pop/20/5/10.1063/1.4807033>.
- E. G. Zweibel. The basis for cosmic ray feedback: Written on the wind. *Physics of Plasmas*, 24(5):055402, 2017. doi: 10.1063/1.4984017. URL <http://dx.doi.org/10.1063/1.4984017>.

# A Appendix

## Convergence study

We briefly discuss the numerical convergence of our simulations. As described in section 5.2.3, we use two setups, that only differ in their number of resolution elements (cells and tracer particles). Figure A.1 shows the multi-frequency spectrum (top panel) that is calculated for the low resolution of  $1 \times 10^6$  cells (blue lines) and the high resolution of  $5 \times 10^6$  cells (orange lines). Both spectra are calculated with our best-fit parameters which are spectral indices  $\alpha_e = 2.1$  for electrons and  $\alpha_p = 1.9$  for protons, gas density of  $n = 0.12 \text{ cm}^{-3}$ , distance of  $D = 1660 \text{ pc}$ , equivalent magnetic field of  $B = 35 \text{ } \mu\text{G}$  (as a result of a turbulent dynamo), and Bell amplification by a factor of 20. The bottom panel of Figure A.1 shows the relative error

$$\delta = \left| 1 - \frac{d\Phi_{\text{low}}/dE}{d\Phi_{\text{high}}/dE} \right| \quad (\text{A.1})$$

of the low to high resolution simulation spectrum. The relative error becomes largest in the cutoff regions of the synchrotron and IC spectra. However, the relative error is below 15 per cent at the X-ray and  $\gamma$ -ray data points. This is accurate enough to enable our parameter space study presented in Section 5.6 at a feasible computational costs.

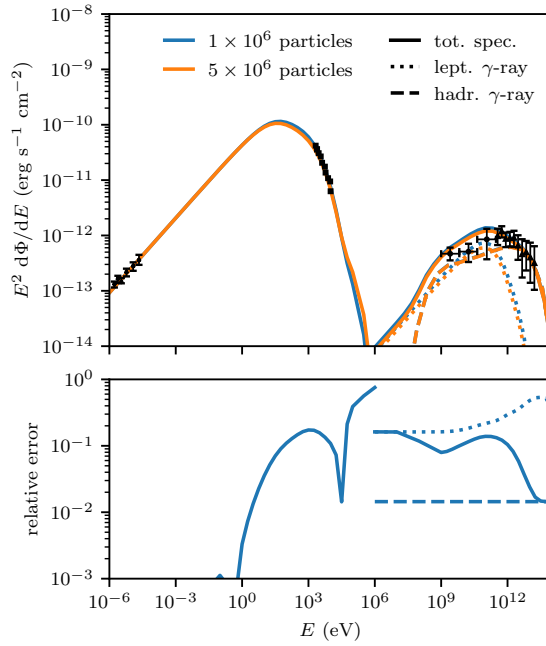


Figure A.1: Multi frequency spectra (top) and relative error (bottom) for a simulation at low resolution with  $1 \times 10^6$  cells (blue) and at high resolution with  $5 \times 10^6$  cells (orange). The spectrum is calculated with our best-fit parameters: spectral indices  $\alpha_e = 2.1$  for electrons and  $\alpha_p = 1.9$  for protons, gas density of  $n = 0.12 \text{ cm}^{-3}$ , distance of  $D = 1660 \text{ pc}$ , equivalent magnetic field of  $B = 35 \mu\text{G}$  (as a result of a turbulent dynamo), and Bell amplification by a factor of 20.

# Danksagung

Diese Arbeit beruht auf vier Jahren Forschung am Heidelberger Institut für theoretische Studien (HITS) und am Leibniz-Institut für Astrophysik Potsdam (AIP), die ohne die Unterstützung zahlreicher Personen in dieser Form nicht möglich gewesen wäre.

Mein besonderer Dank gilt zunächst an Prof. Dr. Christoph Pfrommer, der mir die Möglichkeit gegeben hat, mit ihm an diesem Promotionsthema zu arbeiten, und der meine Arbeit mit großer Begeisterung betreut hat. Ferner danke ich Prof. Dr. Ralf Klessen, der meine Arbeit als Zweitgutachter und im Thesiskomitee betreut hat. Für konstruktive Anregungen im Thesiskomitee sowie für den Zugang zum AREPO Simulationscode bedanke ich mich bei Prof. Dr. Volker Springel.

Der regelmäßige Austausch in der Gruppe zu allen Themen der Astrophysik, der Computersimulationen und weit darüber hinaus haben mich bereichert und bei dieser Arbeit unterstützt. Insbesondere der Austausch mit Christoph Pfrommer und Philipp Girichidis sowie mit Rüdiger Pakmor vom Max-Planck-Institut für Astrophysik München haben zum Erfolg dieser Arbeit beigetragen. Herzlicher Dank geht auch an Matteo Pais, Maria Werhahn, Martin Sparre, Thomas Berlok, Alexander Scherrmann, Mohamad Shalaby, Kristian Ehlert sowie an alle anderen Gruppenmitglieder.

Ich bedanke mich für die finanzielle Unterstützung von der Heidelberg Graduate School for Physics (HGSFP). Für dieses Projekt wurden Fördermittel des Europäischen Forschungsrats (ERC) im Rahmen des Programms der Europäischen Union für Forschung und Innovation „Horizont 2020“ bereitgestellt (CRAGSMAN, Finanzhilfvereinbarung Nr. 646955).

Abschließend möchte ich mich von ganzem Herzen bei meiner Freundin Valérie, meiner Familie und meinen Freunden bedanken, die mir emotionalen Rückhalt gegeben haben und mich mit großem Engagement unterstützt haben.